Oxygen-related Point Defects in Silicon and Germanium

Submited by José Pedro Abreu Coutinho to the University
of Exeter as a thesis for the degree of Doctor of Philisophy
in Physics.

December, 2001

Abstract

A modelling study of several oxygen related defects in silicon and germanium crystals is reported. These include radiation and thermally activated defects. The problem of thermal donor formation is revised in detail. Here we report the properties of the simple interstitial oxygen complexes, their diffusivity and clustering properties, culminating with a novel model for the thermal double donor defects (TDD). The model is also extended to the hydrogen-related shallow thermal donor family, STD(H). According to the model, electrons from over-coordinated oxygen atoms with a donor level lying above that of a stress-induced state, are transfered to the later. This picture is analogous to that of an externally doped quantum-dot.

To my parents,

Adélio and Maria Isabel.

Aknowledgements

Contents

List of Tables

12

List of Figures

List of Publications

1. J. Coutinho, R. Jones, P. R. Briddon, S. Öberg, L. I. Murin, V. P. Markevich, J. L. Lindström, *Thermal Double Donors as Quantum Dots*, to appear in Phys. Rev. Lett.

2. J. Coutinho, R. Jones, P. R. Briddon, S. Öberg, L. I. Murin, V. P. Markevich, J. L. Lindström, *The interstitial carbon-oxygen center and the hydrogen related shallow thermal donors in Si*, to appear in Phys. Rev. B.

3. R. Jones, J. Coutinho, S. Öberg, P. R. Briddon, *Thermal Double Donors and Quantum Dots*, to appear in Physica B.

4. J. Coutinho, R. Jones, P. R. Briddon, S. Öberg, L. I. Murin, V. P. Markevich, J. L. Lindström, *Interaction between hydrogen and the interstitial carbon-oxygen center in Si*, to appear in Physica B.

5. L. I. Murin, V. P. Markevich, J. L. Lindström, V. V. Litvinov, J. Coutinho, R. Jones, P. R. Briddon, S. Öberg, *Isotopic effects on local vibrational modes of thermal double donors in Si and Ge*, to appear in Physica B.

6. J. Coutinho, R. Jones, P. R. Briddon, S. Öberg, *Oxygen and dioxygen centers in Si and Ge: Density-functional calculations*, Phys. Rev. B **62**, 10824 (2000).

7. V. P. Markevich, L. I. Murin, M. Suezawa, J. L. Lindström, J. Coutinho, R. Jones, P. R. Briddon, S. Öberg, *Observation and theory of the VOH_2 complex in silicon*, Phys. Rev. B **61**, 12964 (2000).

8. J. Coutinho, R. Jones, P. R. Briddon, S. Öberg, *Formation and diffusivity of small oxygen aggregates in Si and Ge*, Proceedings of the Second ENDEASD Workshop, (Stockholm, 2000).

9. V. P. Markevich, L. I. Murin, M. Suezawa, J. L. Lindström, J. Coutinho, R. Jones, P. R. Briddon, S. Öberg, *Local vibrational mode bands of VOH complexes in silicon*, Physica B **273-274**, 300 (1999).

Introduction

Almost all silicon wafers used for micro-electronic circuits are prepared by the Czochralski technique (Abe, 1985). Here, polysilicon nuggets and doping elements are melted in a silica crucible. A crystal seed dipped into the melt is pulled and rotated, such that dislocation-free $\sim$200 mm diameter ingots are obtained. Because of the high oxygen solubility ($\sim10^{18}$ cm^{-3}) in the melt (Hrostowski and Kaiser, 1959), interstitial oxygen defects (O_i) are normally present in Cz-Si wafers as a super-saturated solution. Despite these concentrations, interstitial oxygen was known to be electrically harmless and located at a bond-centre site (Kaiser *et al.*, 1956). The main reason why oxygen is a beneficial impurity in Si, stems from two main reasons. (i) oxygen greatly enhances mechanical resistivity of Si crystals, and (ii) in the form of SiO_2 precipitates, it is used as a getterer for highly undesirable transition metals (*intrinsic gettering*) (Shimura, 1994).

In the mid 1950's, when semiconductor silicon (Si) was still in its early stages of development for electronic applications, it was found that the conductivity of Si samples grown by the Czochralski (Cz) method could be dramatically enhanced after heat treatments around 450°C (Fuller *et al.*, 1954). Soon after, it was realised that oxygen-related donor defects were at the origin of this enhancement. The thermal activation of these defects lead to their labelling as *thermal donors* (TD) (Fuller and Logan, 1957; Kaiser *et al.*, 1958). Concentrations of TD defects could in fact reach orders of magnitude higher than that of the dopant — presenting a serious threat to device performance after heat-treatment fabrication processes.

When Fuller *et al.* (1954) discovered the conductivity enhancement, they also noticed a recovery of the initial resistivity following heat treatments above 600°C. This is basically what we call a *donor-killing* process, employed to break the TD defects.

Today we know about the existence of several thermally activated oxygen-related donor families. In general they are referred to as thermal donors (TD), comprising thermal double donors (TDD), shallow thermal donors (STD), new donors (ND), and other less studied classes like the ultra-shallow thermal donors (USTD) (Jones, 1996). Here we are

particularly interested in the first two families. In the last 30 years, more than any other problem on defects in semiconductor, the most varied and sophisticated experiments were applied to study thermal donors. Unfortunately, the technique that could unravel the most structural and chemical information — magnetic resonance — resulted in structureless or extremely weak signals. However, in the recent years, considerable progress has been made with infra-red absorption spectroscopy. The revelation of local vibrational modes associated with oxygen aggregates (Lindström and Hallberg, 1996; Öberg *et al.*, 1998) (including the O-dimer and early TDD members), gives us an unprecedented opportunity to review the problem theoretically.

The most important features of TDD's established so far include (Jones, 1996):

- Up to 17 TDD(N) members were identified, with $0 \leq N \leq 16$;

- The donor states are those of an effective-mass theory double donor, with first and second ionisation levels at $\sim$70 and $\sim$150 meV, monotonically decreasing with N;

- The generation kinetics and the maximum concentration of donors depend on the oxygen content;

- Initial TDD growth is mediated by a 1.7 eV activation barrier, which decreases to 1.1 eV for the later species;

- The overall donor symmetry is C_{2v}, although small deviations were reported after high-field resonance experiments;

- Short heat treatments above 600°C destroys the electrical activity of TDD's, which is accompanied by an increase of O_i content;

- Impurities like carbon, nitrogen, hydrogen and aluminium are known to influence the production of the donors.

- Electron irradiation and hydrostatic pressure strongly enhance TDD formation rates

- Each TDD member appears to produce at least three infra-red active local vibrational modes at $\sim$1000, $\sim$720 and $\sim$580 cm^{-1}.

Inspection of the list given above, lead us to conclude that despite a half-century of active debate, the general picture is well understood, but details by which thermal donor defects form, as well their chemical nature and structure remain obscure. Therefore we have a fundamental problem to be solved. Most importantly, (i) following the current steady rate of device miniaturisation, soon the presence of a mere few donors and low dopant uniformity will certainly affect the overall device performance; (ii) formation of oxygen-free (*denuded*) zones demand a detailed knowledge of the early stages of oxygen aggregation. Being aware that oxygen-rich Ge crystals or Ge rich Cz-Si also suffers from the thermal donor problem, it is expected that SiGe technology, a promising material to operate in the microwave region, will inherit the knowledge from its group-IV constituents. These are some convincing facts driving the semiconductor community to study the problem.

This thesis is divided into six chapters, starting with a description of the method, culminating with models for TDD and STD defects. Chapter 2 presents a review of the relevant experimental details involved in the TDD problem. These include electron paramagnetic resonance (EPR) and electron-nuclear double resonance (ENDOR), photoluminescence (PL), deep-level transient spectroscopy (DLTS) and infra-red (IR) absorption. In Chapter 3 we review previous modelling of vacancy-oxygen defects. This is an issue not only somewhat indirectly related to the TDD problem, but also serving as a *benchmark* test for the method employed here. Chapter 4 discusses the very early oxygen aggregates in Si and Ge, with oxygen diffusivity and self-interstitial ejection as central issues. In the two final chapters, the TDD and STD models are discussed, where calculated observables are directly compared with the experimental observations.

Chapter 1

Theoretical framework

1.1 The many-body problem

In the absence of external fields, the Schrödinger equation for a non-relativistic and stationary problem involving a set of N_{e} electrons and N_{n} atomic nuclei can be written as

$$\widehat{\mathcal{H}}\Psi = E\Psi. \tag{1.1}$$

Here, the Hamiltonian $\widehat{\mathcal{H}}$ contains the usual kinetic and potential terms[1],

$$\begin{aligned}
\widehat{\mathcal{H}} = &-\frac{1}{2}\sum_{i}^{N_{\mathrm{e}}}\nabla_i^2 - \sum_{\alpha}^{N_{\mathrm{n}}}\frac{1}{2M_\alpha}\nabla_\alpha^2 + \\
&+\frac{1}{2}\sum_{\substack{i,j=1 \\ i\neq j}}^{N_{\mathrm{e}}}\frac{1}{|\mathbf{r}_i - \mathbf{r}_j|} - \sum_{i,\alpha=1}^{N_{\mathrm{e}},N_{\mathrm{n}}}\frac{Z_\alpha}{|\mathbf{r}_i - \mathbf{R}_\alpha|} + \frac{1}{2}\sum_{\substack{\alpha,\beta=1 \\ \alpha\neq\beta}}^{N_{\mathrm{n}}}\frac{Z_\alpha Z_\beta}{|\mathbf{R}_\alpha - \mathbf{R}_\beta|},
\end{aligned} \tag{1.2}$$

where M_α, Z_α and $\mathbf{R}_\alpha$ represent the mass, charge and location of the α-th nucleus, and $\mathbf{r}_i$ the i-th electron coordinate. The total wavefunction Ψ from Equation 1.1 is therefore

---

[1] All quantities are expressed in atomic units (unless otherwise specified). In this system of units, $\hbar$, e, m and $4\pi\epsilon_0$ are taken to be unity, where e, m and ϵ_0 are the electron charge, electron mass, and the permitivity of vacuum respectively. The unit of length is 0.529 Å, and the unit of energy is 27.211 eV.

a function of N_n nuclei coordinates, plus N_e electron spatial and spin coordinates, $\mathbf{r}_i$ and s_i respectively,

$$\Psi \equiv \Psi(\mathbf{r}_1, s_1, \ldots, \mathbf{r}_{N_e}, s_{N_e}; \mathbf{R}_1, \ldots, \mathbf{R}_{N_n}). \qquad (1.3)$$

Disregarding any analytical solution for 1.1 (only known for problems such as the hydrogen and He$^+$ atoms (Schiff, 1955)), one can appreciate the fact that Ψ depends on $3N_n + 4\sum_\alpha Z_\alpha$ scalar variables, and even the simplest problem with potential technological applications is simply intractable even when using the fastest computers available. This is the stage where one is forced to develop a theoretical framework by trading approximations for an useful output, keeping the standards of accuracy as high as possible.

1.2 Born-Oppenheimer approximation

By noting that the electron mass is $\sim$2000 times lighter than that of a neutron or proton, we expect electrons to respond *instantaneously* to atomic motion. In other words, the shape of an electron-only wavefunction will adapt adiabatically to nuclear motion. The idea proposed by Born and Oppenheimer (1925), was that a first order ansatz

$$\Psi(\mathbf{r}; \mathbf{R}) = \psi_{\mathbf{R}}(\mathbf{r})\, \phi(\mathbf{R}) \qquad (1.4)$$

for the total wavefunction Ψ, where ψ and ϕ are separate electronic and nuclear wavefunctions, is a good solution for the ground state of the Hamiltonian in 1.2. The variables $\mathbf{r}$ and $\mathbf{R}$ represent now all electronic and nuclear degrees of freedom. As no magnetic fields are considered, we drop the spin indexes for the moment. The subscript on ψ stresses the fact that the electronic wavefunction depends on $\mathbf{R}$ in a parametric way.

Substituting 1.4 in 1.2, one obtains

$$\widehat{\mathcal{H}}\psi_{\mathbf{R}}(\mathbf{r})\phi(\mathbf{R}) = (E_{\mathrm{n}} + E_{\mathrm{e}})\,\psi_{\mathbf{R}}(\mathbf{r})\phi(\mathbf{R})-$$

$$-\sum_{\alpha}^{N_{\mathrm{n}}}\frac{1}{2M_{\alpha}}\left[\phi(\mathbf{R})\nabla_{\alpha}^2\psi_{\mathbf{R}}(\mathbf{r}) + 2\boldsymbol{\nabla}_{\alpha}\psi_{\mathbf{R}}(\mathbf{r})\cdot\boldsymbol{\nabla}_{\alpha}\phi(\mathbf{R})\right]. \qquad (1.5)$$

with E_{n} and E_{e} as eigenvalues from the separate nuclear and electronic problems respectively,

$$\left(\widehat{\mathcal{T}}_{\mathrm{n}} + \widehat{\mathcal{V}}_{\mathrm{nn}}\right)\phi \;\;=\;\; E_{\mathrm{n}}\phi \qquad (1.6)$$

$$\left(\widehat{\mathcal{T}}_{\mathrm{e}} + \widehat{\mathcal{V}}_{\mathrm{ee}} + \widehat{\mathcal{V}}_{\mathrm{en}}\right)\psi \;\;=\;\; E_{\mathrm{e}}\psi. \qquad (1.7)$$

Equations 1.6 and 1.7 include all kinetic $(\widehat{\mathcal{T}})$ and potential $(\widehat{\mathcal{V}})$ terms in the many-body Hamiltonian in 1.2. Subscripts n and e label the nuclear and electronic terms respectively. Now making use of the hypothesis — for $M_{\alpha} \gg 1$, the total energy E is given by the independent electronic and nuclear eigenvalues E_{e} and E_{n}, with the ansatz in 1.4 as eigenstate. Hence, a stationary state of a many-body system is normally defined after finding ψ for a set of fixed atomic positions (see Section 1.3).

From now on, we will then focus on the electronic problem and its Hamiltonian,

$$\widehat{\mathcal{H}} = \widehat{\mathcal{T}}_{\mathrm{e}} + \widehat{\mathcal{V}}_{\mathrm{ee}} + \widehat{\mathcal{V}}_{\mathrm{en}} = \qquad (1.8)$$

$$= -\frac{1}{2}\sum_{i}^{N_{\mathrm{e}}}\nabla_i^2 + \frac{1}{2}\sum_{\substack{i,j=1\\i\neq j}}^{N_{\mathrm{e}}}\frac{1}{|\mathbf{r}_i - \mathbf{r}_j|} - \sum_{i,\alpha=1}^{N_{\mathrm{e}},N_{\mathrm{n}}}\frac{Z_{\alpha}}{|\mathbf{r}_i - \mathbf{R}_{\alpha}|}. \qquad (1.9)$$

It is worth noting that when electron-nuclear coupling is strong, the Born-Oppenheimer breaks down. This is also the case for Jahn-Teller systems, where $\boldsymbol{\nabla}_{\alpha}\psi$ is large enough as to impose a nuclear distortion due mixing of the nuclear and electronic wavefunctions.

1.3 Variational principle

There are two main methods used to attain stationary solutions for the Hamiltonian in 1.8 — grid and variational methods. The first integrates the Schrödinger equation using discretisation methods, and the second uses a variational principle. In this method, a carefully chosen subspace $\{\phi_1, \ldots, \phi_M\}$ of Hilbert space is used to span an approximation Ψ_{app} of the ground-state wavefunction Ψ_0 as

$$\Psi_0 \approx \Psi_{\text{app}} = \sum_i^M c_i \phi_i. \tag{1.10}$$

Now using the expectation value for the total energy E written as a functional of the wavefunction Ψ,

$$E\left[\Psi\right] = \frac{\langle \Psi | \widehat{\mathcal{H}} | \Psi \rangle}{\langle \Psi \mid \Psi \rangle}, \tag{1.11}$$

gives the approximate total energy

$$E_{\text{app}} = E\left[\Psi_{\text{app}}\right] = \frac{\sum_{i,j=1}^{M} c_i^* c_j H_{ij}}{\sum_{i,j=1}^{M} c_i^* c_j S_{ij}}, \tag{1.12}$$

with $H_{ij} = \langle \phi_i | \widehat{\mathcal{H}} | \phi_j \rangle$ and $S_{ij} = \langle \phi_i \mid \phi_j \rangle$. These are referred as the Hamiltonian and overlap matrix elements. Stationary states then follow from the condition that the derivative of E_{app} with respect to c_i vanishes, leading to

$$\sum_{j=1}^{M} \left(H_{ij} - E_{\text{app}} S_{ij}\right) c_j = 0, \ \text{ for } \ i = 1, \ldots, M, \tag{1.13}$$

or in a more compact form, to the following generalised eigenvalue equation:

$$\mathsf{H} \cdot \mathbf{c} = E_{\text{app}} \, \mathsf{S} \cdot \mathbf{c}. \tag{1.14}$$

The lowest eigenvalue from the above secular equation is higher than (or equal to) the true ground state energy E_0. Including more basis functions into our set, the subspace becomes larger, and consequently E_{app} will decrease or become constant. This is known as the Rayleigh-Ritz variational principle (Kemble, 1932; MacDonald, 1933).

Theorem 1 (Variational principle) *The energy E_{app} computed from an approximate Ψ_{app} wavefunction is an upper bound to the true ground-state energy E_0. Full minimisation of the functional $E[\Psi]$ with respect to the all allowed basis functions will give the true ground state Ψ_0 and energy $E_0 = E[\Psi_0]$; that is,*

$$E_0 = \min_{\Psi} E[\Psi]. \qquad (1.15)$$

The variational principle is used in almost all electronic structure calculations where the ground state Ψ_0 is the goal. This is also the case for density-functional methods.

1.4 Hartree-Fock method

The Hartree-Fock (HF) method (Fock, 1930; Roothaan, 1951; Slater, 1965; Stoneham, 1975) uses a variational approach in which the wave function of the many-electron system has the form of an anti-symmetrised product of one-electron wavefunctions (therefore taking into account the Pauli exclusion principle). These are elegantly written in the form of Slater determinants (Slater, 1929),

$$\Psi_{\text{SD}}(\mathbf{x}_1, \ldots, \mathbf{x}_N) = \frac{1}{\sqrt{N!}} \det \begin{bmatrix} \psi_1(\mathbf{x}_1) & \cdots & \psi_N(\mathbf{x}_1) \\ \vdots & \ddots & \vdots \\ \psi_1(\mathbf{x}_N) & \cdots & \psi_N(\mathbf{x}_N) \end{bmatrix}, \qquad (1.16)$$

where $\mathbf{x}_i$ includes spatial and spin coordinates of the i-th electron, and ψ_i are one-electron *spin-orbitals*, which we assume to be orthogonal. The wavefunctions Ψ_{SD} carries the exchange properties of a many-body wavefunction. The determinantal form ensures its

anti-symmetry as exchanging two electron coordinates affects Ψ_{SD} by a factor of -1, and $\Psi_{\mathrm{SD}} = 0$ if two electrons with the same coordinates are present.

Considering Ψ_{SD} as a solution of the Hamiltonian in 1.8, one arrives at an expectation value for the total energy,

$$E = \sum_i^N H_i + \frac{1}{2} \sum_{i,j=1}^N \left(J_{ij} - K_{ij} \right), \tag{1.17}$$

where H_i is the one-electron integral

$$H_i = \int \psi_i^*(\mathbf{x}) \left[-\frac{1}{2}\nabla_i^2 - \sum_{\alpha=1}^{N_\mathrm{n}} \frac{Z_\alpha}{|\mathbf{r}_i - \mathbf{R}_\alpha|} \right] \psi_i(\mathbf{x}) \, d\mathbf{x}, \tag{1.18}$$

and J_{ij} and K_{ij} are called *Hartree* and *exchange integrals*. These are given by the following two-electron terms,

$$J_{ij} = \iint \psi_i(\mathbf{x})\psi_i^*(\mathbf{x}) \frac{1}{|\mathbf{r} - \mathbf{r'}|} \psi_j(\mathbf{x'})\psi_j^*(\mathbf{x'}) \, d\mathbf{x} \, d\mathbf{x'} \tag{1.19}$$

$$K_{ij} = \iint \psi_i(\mathbf{x})\psi_j^*(\mathbf{x}) \frac{1}{|\mathbf{r} - \mathbf{r'}|} \psi_i(\mathbf{x'})\psi_j^*(\mathbf{x'}) \, d\mathbf{x} \, d\mathbf{x'}, \tag{1.20}$$

where integration in $\mathbf{x}$ represent spatial integration and spin summation, i.e., $\mathbf{x} = (\mathbf{r}, s)$. The reason why the two-electron summation in 1.17 include the $i = j$ term is because $J_{ii} = K_{ii}$. Hence, this summation is composed of an electron-electron repulsion term, plus an exchange component representing spin-correlation effects.

Minimisation of 1.17 subject to the orthogonality condition $\langle \psi_i \mid \psi_j \rangle = \delta_{ij}$, gives the Hartree-Fock equations (McWeeny, 1989; Thijssen, 1999),

$$\widehat{\mathcal{F}} \, \psi_i(\mathbf{x}) = \sum_{j=1}^N \epsilon_{ij} \, \psi_j(\mathbf{x}), \tag{1.21}$$

with $\widehat{\mathcal{F}}$ known as Fock operator, and defined as

$$\widehat{\mathcal{F}} = \widehat{h} + \widehat{j} - \widehat{k} \tag{1.22}$$

with $\langle\psi_i|\widehat{h}|\psi_i\rangle = H_i$ (see Equation 1.18), and

$$\widehat{j}(\mathbf{x})f(\mathbf{x}) = \sum_{k=1}^{N} \int \psi_k^*(\mathbf{x}')\psi_k(\mathbf{x}')\frac{1}{|\mathbf{r}-\mathbf{r}'|}f(\mathbf{x})\,d\mathbf{x}' \tag{1.23}$$

$$\widehat{k}(\mathbf{x})f(\mathbf{x}) = \sum_{k=1}^{N} \int \psi_k^*(\mathbf{x}')f(\mathbf{x}')\frac{1}{|\mathbf{r}-\mathbf{r}'|}\psi_k(\mathbf{x})\,d\mathbf{x}' \tag{1.24}$$

for $f(\mathbf{x})$ an arbitrary function. The matrix $\boldsymbol{\epsilon}$ consists of Lagrange multipliers from the minimisation procedure. Its diagonal elements are obtained after integrating the Fock operator, i.e.,

$$\epsilon_i \equiv \epsilon_{ii} = \langle\psi_i|\widehat{\mathcal{F}}|\psi_i\rangle = H_i + \sum_{j=1}^{N}\left(J_{ij} - K_{ij}\right), \tag{1.25}$$

which after summation and compared with Equation 1.17, gives the total energy as

$$E = \sum_{i=1}^{N}\epsilon_i - \frac{1}{2}\sum_{i,j=1}^{N}\left(J_{ij} - K_{ij}\right). \tag{1.26}$$

Usually, in a computer implementation of the HF method, the spin-orbitals ψ_i are expanded as a linear combination of atomic orbitals. Hence, as in Section 1.3, after carefully choosing a set of M functions $\phi_i(\mathbf{x})$, we define

$$\psi_j(\mathbf{x}) = \sum_{i}^{M} c_{ij}\phi_i(\mathbf{x}) \tag{1.27}$$

The Fock equation then takes a matrix form, and therefore we end with a generalised eigenvalue problem similar to that of Section 1.3, called *Roothaan equation* (Roothaan, 1951),

$$F \cdot \mathbf{c}_j = \epsilon_j S \cdot \mathbf{c}_j, \qquad (1.28)$$

where S is again the $M \times M$ overlap matrix $S_{ij} = \langle \phi_i \,|\, \phi_j \rangle$. The above equation is solved in a self-consistent way, until the wavefunction convergence is attained along with the total energy.

The physical meaning of the eigenvalues from the Roothaan equation was developed by Koopmans (1934).

Theorem 2 (Koopmans' theorem) *Assuming that the eigenstates $\mathbf{c}_j$ do not vary after removal of one electron from the system, the ionisation energy I_m of the m-th electron is given by $I_m = -\epsilon_m$.*

An important consequence of the Koopmans theorem is the ability to calculate excited states within the HF method.

In this section, we did not include the spin in the formulation. This leads to *open-shell* or *unrestricted systems*, as opposed to the spin-averaged *closed-shell systems*. In the open-shell formalism, the non-local matrix elements J_{ij} and K_{ij} must couple both spins by explicitly summing over this degrees of freedom. For a review on this issue, see Slater (1965); Schaefer (1977); Lawley (1987).

The Hartree-Fock theory has one major short-coming — the wavefunction does not incorporate electron-correlation, i.e., the spin-orbitals do not have a functional dependence on $\mathbf{r}_i - \mathbf{r}_j$. This problem can be solved by expressing Ψ as a linear combination of Slater determinants, known as Configuration Interaction (CI) method. Unfortunately, this carries a serious computational cost as the number of determinants grows rapidly with the size of the system. Also the evaluation of the J_{ij} and K_{ij} matrix elements is a demanding computational task — its CPU-time scales with the fourth power of basis size. In fact, even with help of modern supercomputers, only systems with a few tens of atoms can be studied (see for example Pisany *et al.* (1988); Kantorovich *et al.* (2000)).

1.5   Density-Functional Theory

As we saw in Section 1.4, application of the all-electron HF method is prohibitive in extended systems. The non-local character of both the $\widehat{j}$ and $\widehat{k}$ operators (their values at $\mathbf{r}$ depend on another coordinate $\mathbf{r}'$), complicates the evaluation of the J_{ij} and K_{ij} matrix elements. Most of today's state-of-the-art electronic structure calculations in solids use Density-Functional Theory (DFT) (Hohenberg and Kohn, 1964; Kohn and Sham, 1965). This theory has been extensively reviewed over the last two decades (Lundqvist, 1983; Parr and Yang, 1989; Jones and Gunnarsson, 1989). Here the total energy $E \equiv E[n]$ is a functional of the electronic charge density $n(\mathbf{r})$, as opposed to the wavefunction in HF. It is then proposed,

$$E[n] = F[n] + \int v_{\text{ext}}(\mathbf{r})n(\mathbf{r})\,d\mathbf{r}, \tag{1.29}$$

with v_{ext} representing an external potential to which the electrons are subject. This includes the ion-electron interaction and other fields. The functional F is universal (system-independent), and accounts for electronic kinetic energy, electron-correlation and exchange-correlation.

Theorem 3 (First Hohenberg-Kohn theorem) *The external potential is determined, within a trivial additive constant, by the electron density $n(\mathbf{r})$ (Hohenberg and Kohn, 1964).*

In DFT, the number of electrons, the external potential, and therefore the ground-state wavefunction along with all its properties are uniquely defined by the charge density.

Theorem 4 (Second Hohenberg-Kohn theorem) *For a trial density $\tilde{n}(\mathbf{r})$, such that $\tilde{n}(\mathbf{r}) \geq 0$ and $\int \tilde{n}(\mathbf{r})\,d\mathbf{r} = N$ (Hohenberg and Kohn, 1964),*

$$E_0 \leq E[\tilde{n}]. \tag{1.30}$$

This expression is analogous to Equation 1.15, and is the basis of a variational principle. Hence in this case

$$E_0 = \min_{\tilde{n}} E\left[\tilde{n}\right]. \tag{1.31}$$

The striking feature of this method, is that despite the huge simplification of adopting the charge density as the variational variable, no approximations are made. Still as in HF, the exchange-correlation contribution to the functional F is a non-local quantity.

1.5.1 Kohn-Sham equations

In DFT, an effective independent particle Hamiltonian is arrived at, leading to the following Schrödinger set of one-electron equations (Kohn and Sham, 1965):

$$\left[-\frac{1}{2}\nabla^2 - \sum_{\alpha} \frac{Z_\alpha}{|\mathbf{r} - \mathbf{R}_\alpha|} + \int \frac{n(\mathbf{r}')}{|\mathbf{r} - \mathbf{r}'|} d^3\mathbf{r}' + \frac{\delta E_{\mathrm{xc}}\left[n\right]}{\delta n(\mathbf{r})} \right] \psi_\lambda(\mathbf{r}) = \epsilon_\lambda \psi_\lambda(\mathbf{r}). \tag{1.32}$$

with the density n obtained by summing up all N occupied spin-orbital states,

$$n(\mathbf{r}) = \sum_{\lambda=1}^{N} |\psi_\lambda(\mathbf{r})|^2. \tag{1.33}$$

The first three terms of Equation 1.32 are the kinetic energy, the external potential imposed by the ions, and the Hartree energy respectively. The fourth term lumps together all remaining many-body effects in the form of an exchange-correlation functional. One main pillar of DFT is the existence of an universal E_{xc} density functional (depending only on the electron density n), leading to the knowledge of the *exact* ground-state total energy and density.

The total energy functional for the many-electron system is given by (Parr and Yang, 1989)

$$E[n] = \sum_{\lambda=1}^{N} \epsilon_\lambda - J[n] + E_{\mathrm{xc}}[n] - \int V_{\mathrm{xc}}[n]\, n(\mathbf{r})\, d\mathbf{r}. \tag{1.34}$$

In Equation 1.34, the Hartree energy and the exchange-correlation potential (J and V_{xc} respectively) are written as

$$J[n] = \frac{1}{2} \int \frac{n(\mathbf{r})n(\mathbf{r'})}{|\mathbf{r} - \mathbf{r'}|}\, d\mathbf{r}\, d\mathbf{r'} \tag{1.35}$$

$$V_{\mathrm{xc}}[n] = \frac{\delta E_{\mathrm{xc}}[n]}{\delta n(\mathbf{r})}. \tag{1.36}$$

The exact form of E_{xc} is however unknown, but some standard approximations are currently used. In fact, improvements to this functional is still one of today's active research areas (Doren *et al.*, 2001; M. A. L. Marques, 2001).

Equations 1.32 and 1.33 – known as *Kohn-Sham equations* (Kohn and Sham, 1965), are solved in a self-consistent loop. We first choose a trial charge density and solve Equation 1.32. The resulting eigenvectors are fed into 1.33 to build a new charge-density, which is the input to Equation 1.32. This process (*self-consistency cycle*) keeps going until the charge-density does not appreciably change.

The above formalism neglects any spin-dependence. Apart from the E_{xc} correlation functional, all terms are linear with respect to the charge density. The extension of the Kohn-Sham scheme to spin-polarised systems was given by von Barth and Hedin (1972); Rajagopal and Callaway (1973). Here we define the charge density as being made up of spin-up and spin-down densities, $n(\mathbf{r}) = n_\uparrow(\mathbf{r}) + n_\downarrow(\mathbf{r})$, but we still have a non-local $E_{\mathrm{xc}}[n_\uparrow(\mathbf{r}), n_\downarrow(\mathbf{r})]$. This will be discussed later. Note that we have now one-electron spin-orbitals, and therefore the total charge density is

$$n(\mathbf{r}) = \sum_{\lambda=1}^{N/2} \sum_{s} |\psi_\lambda(\mathbf{r}, s)|^2. \tag{1.37}$$

1.5.2 The exchange-correlation functional

In DFT, the exchange-correlation energy is accounted by the $E_{\rm xc}[n]$ non-local density functional. This functional is however unknown. Several approaches have been taken to overcome this problem. The most common is to assume a local density approximation (LDA), or local spin-density approximation (LSDA) for non-zero spin systems (Kohn and Sham, 1965; von Barth and Hedin, 1972; Perdew and Zunger, 1981). Here, it is assumed that the exchange-correlation energy is local. Normally this energy is separated into exchange and correlation parts, where in LSDA notation,

$$E_{\rm xc}[n_\uparrow, n_\downarrow] = E_{\rm x}[n_\uparrow, n_\downarrow] + E_{\rm c}[n_\uparrow, n_\downarrow]. \qquad (1.38)$$

The exchange functional is linear with respect to n, and its analytic form is given by (von Barth and Hedin, 1972),

$$E_{\rm x}[n_\uparrow, n_\downarrow] = -\frac{3}{2}\left(\frac{3}{4\pi}\right)^{1/3}\left(n_\uparrow^{4/3} + n_\downarrow^{4/3}\right). \qquad (1.39)$$

The correlation part is however more complicated. In the high-density regime, perturbation theory yields one expression (Perdew and Zunger, 1981), while in the low-density regime, a Green function quantum Monte Carlo method yields another (Ceperley, 1978; Ceperley and Alder, 1980). A simple parameterised functional form is then fitted to the numerical results. Several parameterisations are available, namely those from Perdew and Zunger (1981) (PZ), Vosko *et al.* (1980) (VWN) and Perdew and Wang (1992) (PW). First-order expansions of $E_{\rm xc}$ in the density were also developed. This is the generalised gradient approximation (GGA), and includes terms depending on $\boldsymbol{\nabla}n$ (Perdew, 1991; Perdew *et al.*, 1996*a*,*b*).

1.6 Pseudopotentials

It is well known that the standard properties of molecules or solids are governed by valence electrons. Electrons in core-states behave much like those in isolated atoms, creating a

screening effective potential — a *pseudopotential*, seen by the valence electrons. The idea behind the pseudopotential method is to split the all-electron Coulomb operator into two separate parts, i.e., one that takes care of the inner core-states, and the other dealing with valence states. This allows us to drop matrix elements regarding the core-electrons, and focus only on few remaining ones. Detailed information on the pseudopotential method has been extensively reported (Harrison, 1966; Brust, 1968; Stoneham, 1975; Heine, 1970; Pickett, 1989).

Two main reasons justify this approach, i) a full electron potential implies large total energies, therefore leading to large errors when comparing similar systems, ii) the number of basis functions required to fit all states (especially those at the core) would become prohibitively large, and affordable expansions would carry catastrophic consequences to accuracy of the total energy.

Obviously the utilisation of pseudopotentials has implications. Some assumptions (or approximations) are made, namely i) the *frozen core approximation* which assumes the core states to be unperturbed when the atom is transfered to a specific environment, and ii) the *small core approximation* where one assumes negligible overlap between core and valence states.

1.6.1   Basic formulation

Transferability *measures* the quality of a pseudopotential. That is, a pseudopotential will be transferable if it can reproduce the properties of the valence electrons, in a wide rage of different problems. To accomplish this, the pseudopotential must be constructed by stripping off valence electrons from the atom, leaving behind an *ionic-pseudopotential* (Heine, 1970). Within the density-functional framework,

$$\widehat{\mathcal{V}}_{\text{ion}}^{\text{ps}}(\mathbf{r}) = \widehat{\mathcal{V}}^{\text{ps}}(\mathbf{r}) - \int \frac{n^{\text{ps}}(\mathbf{r})}{|\mathbf{r} - \mathbf{r}'|} \, d\mathbf{r}' - \widehat{\mathcal{V}}_{\text{xc}}[n(\mathbf{r})], \tag{1.40}$$

with

$$n^{\mathrm{ps}}(\mathbf{r}) = \sum_{\lambda} \left| \psi_{\lambda}^{\mathrm{ps}}(\mathbf{r}) \right|^2. \tag{1.41}$$

In equations 1.40 and 1.41, $\widehat{\mathcal{V}}^{\mathrm{ps}}$ is the pseudopotential of the neutral atom and n^{ps} the charge-density from the valence states. Note that in 1.40 we not only subtract a classic Coulombic term, but also all exchange-correlation interactions $\widehat{\mathcal{V}}_{\mathrm{xc}}$ between the valence electrons (Pickett, 1989). In this thesis, the pseudopotentials of Bachelet, Hamann and Schlüter are used (Hamann *et al.*, 1982). These were tabulated by Bachelet *et al.* (1982) for elements between H and Pu.

1.7 Boundary-conditions and basis functions

The DFT code implementation used in this work has important features which need to be described. Among these is the use of a real-space Gaussian type basis set (Jones and Briddon, 1999). The choice of the boundary conditions has also important consequences. Here we treat the problem using supercells, involving Brillouin-zone (BZ) integration and reciprocal-space expansions using a Fourier-transformation (Briddon, 1999; Coutinho *et al.*, 2000*b*). We start by defining a supercell.

1.7.1 The supercell

Let us assume a crystallographic material with a unit cell defined by its unit vectors $\mathbf{a}_i$, with $i = 1, 2$ and 3, volume v_0, and containing a set of n_a atoms located at $\mathbf{r}_j$ ($j = 1, \ldots, n_a$) from the origin of the unit cell. The Bravais lattice points are then given by $\mathbf{l_n} = \sum_i n_i \mathbf{a}_i$. Reciprocal-space unit vectors $\mathbf{G}_i$ are then automatically defined as

$$\mathbf{G}_i = 2\pi \frac{\mathbf{a}_j \times \mathbf{a}_k}{\mathbf{a}_i \cdot (\mathbf{a}_j \times \mathbf{a}_k)} \tag{1.42}$$

with i, j, $k = 1, 2, 3$.

A supercell is defined by the linear transformation W with integer elements W_{ij}, operating on $\mathbf{a}_i$,

$$\mathbf{A}_j = \sum_{i=1}^{3} W_{ij}\mathbf{a}_i, \text{ and } W = \det(\mathsf{W}).\tag{1.43}$$

The larger cell with unit vectors $\mathbf{A}_j$ is a *supercell* with volume $\Omega = v_0 W$, and define a lattice of points $\mathbf{L_n} = \sum_i n_i \mathbf{A}_i$ for all integers n_i. Its reciprocal space unit-vectors $\mathbf{g}_j$ define a unit cell W times smaller than that of the $\mathbf{G}_j$ vectors, i.e.,

$$\mathbf{g}_j = \sum_{i=1}^{3} L_{ij}^{-1}\mathbf{G}_i \tag{1.44}$$

with L_{ij}^{-1} representing the elements of L^{-1}. The supercell contain $N_a = n_a W$ atoms, and their location $\mathbf{R}_i$ ($i = 1,\ldots,N_a$) can be defined by any set of N_a independent atomic positions $\mathbf{R}_i$,

$$\mathbf{R}_i = \mathbf{l_n} + \mathbf{r}_k, \text{ for all } \mathbf{R}_i - \mathbf{R}_j \neq \mathbf{L_m}.\tag{1.45}$$

In the expression above, k can take any value between $1 \leq k \leq n_a$, and the index $\mathbf{n}$ can be any integer vector. The important point is that no two atomic positions (say $\mathbf{R}_i$ and $\mathbf{R}_j$), may differ by a lattice vector $\mathbf{L_m}$.

Inserting a defect in the supercell has important consequences. The basis vectors $\mathbf{A}_i$ now form a conventional crystal with a smallest possible unit cell with volume Ω, filled with atoms located at $\mathbf{R}_i$. The goal is to model defects in a crystalline environment. However, as a consequence of periodicity, a defect image will be located in each cell. Note that it does not matter where we place the defect — for example, displacing a substitutional impurity by $\delta\mathbf{r}$ implies that all images will be displaced by the same vector. However, if the supercell is not adequate in terms of size and shape, spurious effects can take place in the form of defect-image coupling through elastic, Coulombic, dipolar and quadrupolar interactions.

One of the implications of using an LDA exchange-correlation functional is the underestimation (by ∼50%) of the band-gap in semiconductors. If the unit cell is not large enough, mixing between defect-related gap states with the band extrema may be considerable. Hence, special attention must be paid to band-bending effects in gap states, especially for the shallow ones.

In the cluster approach, we do not have defect-image interaction, but different problems occur. The most important is defect-surface interaction. Unlike the supercell method, the total electric dipole may depend on the location of the defect (Jones and Briddon, 1999).

1.7.2 Basis functions

We define a set of Bloch basis functions $B_{\mathbf{k}i}(\mathbf{r})$ that are built from a set of Cartesian-Gaussian functions ϕ_i centred at $\mathbf{R}_i$, over N_L the lattice vectors $\mathbf{L_n}$,

$$B_{\mathbf{k}i}(r) = \frac{1}{\sqrt{N_L}} \sum_{\mathbf{L_n}} \phi_i(\mathbf{r} - \mathbf{R}_i - \mathbf{L_n}) \, e^{i\mathbf{k}\cdot\mathbf{L_n}}. \qquad (1.46)$$

with $\mathbf{k}$ as a reciprocal-space vector. The localised orbitals are given by

$$\phi_i(\mathbf{r}) = (x - R_{ix})^{l_1}(y - R_{iy})^{l_2}(z - R_{iz})^{l_3}e^{-a_i(\mathbf{r}-\mathbf{R}_i)^2}, \qquad (1.47)$$

with s-, p- or d-like orbitals corresponding to $\sum_i l_i = 0$, 1 or 2, and with $l_i \geq 0$. The Kohn-Sham orbitals $\psi_{\mathbf{k}\lambda}$ are then expanded over all $B_{\mathbf{k}i}$ basis functions,

$$\psi_{\mathbf{k}\lambda}(\mathbf{r}) = \sum_i c_{\mathbf{k}\lambda,i} B_{\mathbf{k}i}(\mathbf{r}) \qquad (1.48)$$

with the $\mathbf{k}\lambda$ pair labelling the state. The charge-density is readily obtained as

$$n(\mathbf{r}) = \sum_{i,j,\mathbf{k}} b_{ij}(\mathbf{k}) B_{\mathbf{k}i}^*(\mathbf{r}) B_{\mathbf{k}j}(\mathbf{r}), \qquad (1.49)$$

$$b_{ij}(\mathbf{k}) = \sum_{\lambda} f_{\mathbf{k}\lambda} c_{\mathbf{k}\lambda,i}^* c_{\mathbf{k}\lambda,j}, \qquad (1.50)$$

where $f_{\mathbf{k}\lambda}$ is the occupancy of the $\mathbf{k}\lambda$ state. This should be 2 for a filled level and 0 for an empty one.

The advantage of using Gaussian-like functions is that their related integrals can be analytically found, and in contrast with oscillating basis functions, they can be made as to quickly vanish away from $\mathbf{R}_i$ (Jones and Briddon, 1999). However, they are not orthogonal, and over-completeness can induce numerical instabilities.

1.7.3   Brillouin-zone sampling

In the supercell method, the calculation of physical quantities (as for example the total energy, charge density, density of states, etc), require integrations over the Brillouin-zone (BZ). The integrand function $f(\mathbf{k})$ is periodic in reciprocal space, and has no simple analytic form. To avoid numerical integration over a dense mesh, several schemes were developed. As proposed by Baldereschi (1973) and Chadi and Cohen (1973), one or a set of N *special* $\mathbf{k}_i$-points can be used to obtain the average $\bar{f}$ over the BZ, where

$$\bar{f} = \frac{\Omega}{(2\pi)^3} \int f(\mathbf{k}) \, d\mathbf{k} \approx \frac{1}{N} \sum_i^N f(\mathbf{k}_i). \tag{1.51}$$

Despite the obvious advantages of this method over a full integration, it provided no obvious way of checking the convergence of the calculations. A clearer scheme was proposed by Monkhorst and Pack (1976); Pack and Monkhorst (1977) (MP). The main advantages of their method are its simplicity, and convergence is verifiable. Here we define the following sequence of variables[2],

$$u_i = (2i - I - 1)/2I, \qquad\qquad (i = 1, \dots I) \tag{1.52}$$

$$u_j = (2j - J - 1)/2J, \qquad\qquad (i = 1, \dots J) \tag{1.53}$$

$$u_k = (2k - K - 1)/2K, \qquad\qquad (i = 1, \dots K), \tag{1.54}$$

---

[2]In the original paper, $I = J = K$ is imposed, and for a particular I the scheme is normally referred as MP-I^3. However, here we extend the method such it is best suitable for non-cubic BZ cells

with the integers I, J and $K \geq 1$ defining a grid of $I \times J \times K$ points in the reciprocal space given by

$$\mathbf{k}(i, j, k) = u_i\mathbf{g_1} + u_j\mathbf{g_2} + u_k\mathbf{g_3}. \tag{1.55}$$

Now let us assume F, G and H to be point-groups for the Wigner-Seitz cell, Brillouin-zone and crystal respectively, with respective order g_F, g_G and g_H. Consequently, $H \subseteq G \subseteq F$. Note that as G must have time-reversal symmetry, $G = H \times \mathsf{i}$ where i is the inversion operation.

The MP scheme, uses the following recipe:

1. Define the initial grid $\mathbf{k}(i, j, k)$ for a given set of I, J and K integers;

2. Generate a star from each $\mathbf{k}(i, j, k)$ vector using symmetry operations from the lattice point group F;

3. Eliminate all redundant $\mathbf{k}$ vectors, by leaving only one irreducible representative — the *special* $\mathbf{k}$-*point*. This is done by folding each star within the BZ point-group G, and ensuring that it does not lie outside the BZ;

4. Each special $\mathbf{k}_n$-point is associated with a weighting factor w_n. These w_n's are directly related to the representativity of $\mathbf{k}_n$ in the BZ,i.e., with the order g_n of its site symmetry in within the BZ;

$$w_n = g_G/g_n \tag{1.56}$$

For example, in a crystal with C_{2v} point-group and cubic lattice, the BZ has D_{2d} symmetry. If the principal axis is along the z-axis, the $\mathbf{k}$ vector $(0, 0, 1/4)$ (with C_{2v} site symmetry) has a weighting factor $w = 8/4 = 2$, corresponding to the equivalent $(0, 0, 1/4)$ and $(0, 0, -1/4)$ vectors.

Finally, the as in 1.51, the average $\bar{f}$, or the integral of f over the BZ with volume $(2\pi)^3/\Omega$, is simply given by

$$\bar{f} = \frac{\Omega}{(2\pi)^3} \int f(\mathbf{r}) \, d\mathbf{r} \approx \frac{\sum_n w_n f(\mathbf{k}_n)}{\sum_n w_n}. \tag{1.57}$$

1.7.4 Reciprocal-space basis

Although a real-space basis set is used to expand the Kohn-Sham orbitals, the periodic boundary conditions provide the opportunity to work on reciprocal-space as well. Several quantities are more efficiently evaluated in $\mathbf{k}$-space. This is the case of the Hartree (including the local pseudopotential), and exchange-correlation energies. As functionals of the charge density, they are periodic on the BZ. Their Fourier transformation is then a series over reciprocal lattice vectors. Obviously, the quality of the transformation is strictly dependent on the grid of $\mathbf{g}$-vectors. In practice a uniform grid of vectors inside a sphere of radius g_{cut} that defines a *cut-off energy* is used,

$$E_{\mathrm{cut}} = \frac{1}{2} g_{\mathrm{cut}}^2. \tag{1.58}$$

Normally, this energy is increased until the total energy has attained a converged value. We will return to this issue in Section 1.9.

1.7.5 Ewald summations

Evaluation of the Coulombic and dipolar interactions in crystals (including the Madelung energy), involves calculating conditionally converging sums, i.e., its final value depends on the order in which the terms are summed. The problem lies in the fact that a series like $1/r^p$ over r (with $p \le 2$), converge very slowly as r goes to infinity. To solve this problem, Ewald (1921) proposed a method in which the series is split into a fast-converging and slowly-converging parts,

$$\sum_L \frac{1}{r_L^p} = \sum_L \frac{\mathrm{erfc}(\alpha r_L)}{r_L^p} + \sum_L \frac{\mathrm{erf}(\alpha r_L)}{r_L^p}. \tag{1.59}$$

Evaluation of the first term is straightforward as $\text{erfc}(x)$ converges to zero when $x \to \infty$. The last term, slowly converging in real-space, is Fourier transformed, and as a consequence its terms are now *sort-ranged* in reciprocal space. The parameter α controls the transition between the real-space and reciprocal-space summations. Although the analytical result does not depend on the choice of α, in practice this is not true as a consequence of the summations being taken over a finite set of lattice vectors. An extensive treatment of this method was given by Leeuw *et al.* (1980).

1.8   Calculation of observables

The density functional theory method is a ground-state theory. By definition, excited states are not accessible as the Kohn-Sham eigenstates are not electronic wavefunctions. They are a set of basis functions from which the electron density n is expanded. This is the price that it must be paid when writing the Hamiltonian as a functional of n. Nevertheless, many observables can be calculated. These include ground-state structures, electron density, solubilities, electrical levels, vibrational modes, elastic properties, migration barriers, etc.

In this section we discuss how these are obtained, and the experiments (later described in Chapter 2), they are to be compared.

1.8.1   Local structure - forces

As we saw in Subsection 1.5.1, the Kohn-Sham equations must be solved self-consistently. The self-consistent charge-density n is obtained when its Kohn-Sham orbitals give rise to the same potential used to obtain n. We then say that *self-consistency* has been reached. Once n is known, the force $\mathbf{F}_\alpha$ acting on atom α can be obtained as $-\boldsymbol{\nabla}_\alpha E$, where E is the total energy. This can be understood as a consequence of the following theorem (Epstein *et al.*, 1967):

Theorem 5 (Hellmann-Feynman theorem) *Let ζ be a parameter in the Hamiltonian and Ψ_ζ an eigenstate of $\widehat{\mathcal{H}}$. Then*

$$\frac{\partial E}{\partial \zeta} = \left\langle \Psi \left| \frac{\partial \widehat{\mathcal{H}}}{\partial \zeta} \right| \Psi \right\rangle. \tag{1.60}$$

We can now apply this theorem to evaluate the forces acting in every atom. These are extremely important in finding the ground state structure of a set of atoms. They provide the necessary input for the algorithm that optimises the structure (called *relaxation*), with respect to the total energy. Here all atoms are moved along the direction of the force that it is acting on it, until all of them are smaller than a specified value.

The atomic structure is commonly measurable with diffracted X-rays or electrons (see for example Kisielowski (2001)). Experimental support for a particular structure may however lie in spectroscopic data which is directly related to the local atomic arrangement. These include hyperfine interactions, vibrational frequencies, gap-states, piezospectroscopic-tensors, etc.

1.8.2 Formation energies and occupancy levels

The chemical potential μ_X is defined to be the derivative of the Gibbs free energy $G = E + PV - TS$ for a given phase with respect to the number of particles of type X: $\mu_X = \partial G / \partial n_X$ (Reif, 1965; Flynn, 1972). Here, X might represent an atomic species, or electrons. In thermodynamic equilibrium μ_X must be the same in all phases in contact, so it can be considered as the free energy per particle. The PV term can be neglected for pressures involved in solid-state reactions, and hence the formation energy E_f of a crystal with a neutral defect can be expressed as

$$E_f = E_D - \sum_X n_X \mu_X - TS \tag{1.61}$$

where E_D is the total energy of the crystal with the defect, formed by bringing together

n_X particles of species X. Chemical potentials can be considered as the energy X in a standard thermodynamic state.

Now if the defect possesses gap states, it can assume different charge states. Therefore, the formation energy of a charged defect must include a term with the electron chemical potential μ_e. As we are dealing with solids, a natural choice is to lock μ_e to the Fermi level E_{F}. Therefore it is convenient to define $\mu_e = E_{\mathrm{v}} + E_{\mathrm{F}}$, where E_{v} is the top of the valence band. The formation energy $E_f(q)$ of the crystal with the defect in the charge state q is therefore

$$E_f(q) = E_D(q) - \sum_X n_X \mu_X + q(E_{\mathrm{v}} + E_{\mathrm{F}}) \tag{1.62}$$

where the entropy term from 1.61 is neglected. This is not always the best approximation especially at high temperatures. Equation 1.62 allows us to estimate several thermodynamic properties. These include solubilities, defect concentrations subject to the charge neutrality condition, occupancy levels, etc (Baraff and Schlüter, 1985; Qian and Martin, 1988; Northrup, 1989).

For example, the location of a $(q/q + 1)$ level is given by the position of the Fermi-level for which the neutral and charged defects have the same formation energy. This is simply done by extracting E_{F} from the equation $E_f(q) = E_f(q + 1)$.

According to Equation 1.62 the formation energy of a defect at a non-neutral charge state q depends on the position of the valence-band top E_{v}. In a supercell calculation, due to finite size effects, the position of E_{v} differs in the defective supercell from its position in the perfect crystal. Therefore it is necessary to estimate the lineup of the energy levels. As proposed by de Walle and Martin (1987), this offset is the difference in the average potentials taken over a Bulk $\bar{V}_{\mathrm{B}}$ and defective supercells $\bar{V}_{\mathrm{D}}$ respectively. Assuming the valence-band top (from bulk) to coincide with the highest occupied state at $\mathbf{k} = \Gamma$, i.e., $\epsilon_{\lambda\Gamma}$, then

$$E_{\mathrm{v}} = \epsilon_{\lambda\Gamma} + \bar{V}_{\mathrm{D}} - \bar{V}_{\mathrm{B}}. \tag{1.63}$$

This is an *ab-initio* method, in the sense that it is a parameter-free approach. As for the band-gap height, LDA calculations should underestimate the occupancy levels position from the valence band. There are mainly two ways as to overcome this problem, (i) keeping it *ab-initio* but improving the exchange-correlation functional, or (ii) adopting parameter-dependent methods. This is the case of a semi-empirical scheme proposed by Resende *et al.* (1999). The donor or acceptor levels of a defect $E(q/q+1)$ are calculated from the difference in total energies of charged and neutral defects, $\Delta E_D(q/q+1) = E_D(q) - E_D(q+1)$, and comparing the analogous quantity found for a *standard* defect (with well known donor or acceptor levels), that is,

$$E(q/q+1) - E_v = \Delta E_D(q/q+1) - \Delta E_S(q/q+1). \tag{1.64}$$

This method assumes that the defect and standard should have similar levels and treated in the same sized cell and basis (Resende *et al.*, 1999). It has proved very useful in anticipating the single and second acceptor levels of Sn-V defects in Si (Larsen *et al.*, 2000), and is affected by an error of ~ 0.2 eV.

It should be emphasised that these are thermodynamic levels, i.e., they are differences between the ground states of a defect in two charge states. They influence the position of the Fermi-level through a charge balance equation or neutrality condition. These levels are commonly measured by capacitance methods, in particular by deep-level transient spectroscopy (DLTS). In principle, they can also be compared with optical absorption measurements. However, we must bear in mind that no atomic relaxation occurs during photo-ionisation. This should be less problematic for shallow defects, if the extent of the donor or acceptor wavefunction is such that the relaxation energy is negligible when compared with the band-gap.

1.8.3 Mulliken bond population

It is important to understand the properties of gap-states. For example, the carbon interstitial defect in Si has a donor state localised on a *p*-orbital centred on the carbon

atom. This was clearly demonstrated on resonance experiments (Trombetta and Watkins, 1987). One way to determine the contribution from a basis function ϕ_i to a gap state λ is by calculating the Mulliken bond population $p_\lambda(i)$ (Pople and Beverage, 1970), defined as

$$p_\lambda(i) = \frac{1}{N_L} \sum_{j,\mathbf{k}} c_{\mathbf{k}\lambda,i} \, S_{ij}^{\mathbf{k}} \, c_{\mathbf{k}\lambda,j}^*, \tag{1.65}$$

where $S_{ij}^{\mathbf{k}}$ are the overlap matrix elements,

$$S_{ij}^{\mathbf{k}} = \int B_{\mathbf{k}i}^* \, e^{-i\mathbf{k}\cdot\mathbf{r}} B_{\mathbf{k}j} \, d\mathbf{r}. \tag{1.66}$$

Here the sum runs over the special $\mathbf{k}$-points, and $\sum_i p_\lambda(i) = 1$. If a state λ has a strong contribution from the orbital ϕ_i centred on a particular atom, the coefficients $c_{\mathbf{k}\lambda,i}$, and therefore $p_\lambda(i)$ will be large. We can then estimate the hybridisation of the state by comparing all $p_\lambda(i)$ values for s, p and d-type orbitals.

As we shall see in Chapter 2, magnetic resonance experiments can be interpreted as a linear combination of atomic orbitals. This allows paramagnetic wavefunctions to be characterised in terms of amplitude and angular momentum. The Mulliken bond population is therefore very useful when confronted with these measurements.

1.8.4 Localised vibrational modes

Localised vibrational modes and their frequencies are quantities which can be accurately predicted by *ab-initio* methods. These can be directly compared with infra-red absorption or photoluminescence data. Here we use the adiabatic (or Born-Oppenheimer) approximation, in the sense that the nuclei are regarded as point-like masses surrounded by electrons that adiabatically follow their vibrational movement. We also assume the harmonic approximation, according to which, the total energy E of a system composed of N atoms is expanded to second order atomic displacements Born and Huang (1954); Maradudin *et al.* (1963); Stoneham (1975); Srivastava (1990),

$$E = E_0 + \frac{1}{2} \sum_{i,j}^{N} \mathbf{u}_i \cdot \mathsf{K}(i,j) \cdot \mathbf{u}_j, \tag{1.67}$$

where E_0 is the static total energy, $\mathbf{u}_i$ is the displacement of atom i, and $\mathsf{K}(i,j)$ is a second-rank tensor whose elements $K_{ab}(i,j)$ are normally referred as force-constants, given by the second derivatives of the total energy with respect to atomic motion at the equilibrium,

$$K_{ab}(i,j) = \frac{\partial^2 E}{\partial u_{ia} \partial u_{jb}}, \tag{1.68}$$

with a and b representing any of the three Cartesian coordinates.

The equation of motion of an atom i is given by

$$M_i \frac{\partial^2 \mathbf{u}_i}{\partial t^2} = -\boldsymbol{\nabla}_i E = -\sum_j^{N} \mathsf{K}(i,j) \cdot \mathbf{u}_j. \tag{1.69}$$

Assuming a oscillatory solution $\mathbf{u}_i(t)$, one arrives to an eigenvalue problem,

$$\mathsf{D} \cdot \mathbf{U} = \omega^2 \mathbf{U}, \tag{1.70}$$

with the $3N \times 3N$ matrix called *dynamical matrix* (Born and Huang, 1954),

$$\mathsf{D}_{ab}(i,j) = \frac{1}{\sqrt{M_i M_j}} \mathsf{K}_{ab}(i,j). \tag{1.71}$$

Its $3N$ eigenvalues ω^2 are the square frequencies associated with $3N$ normal modes $\mathbf{U}$. Note that each normal mode is a $3N$ dimensional vector representing the motion of all N atoms.

For periodic systems, one need to include a lattice labelling index l. Hence the i-th atom in the l-th unit cell has a displacement represented by $\mathbf{u}_{li}$, and a force constant is now represented by $\mathsf{K}(il, jl')$. A solution to Equation 1.69 assumes now a wave-like form, and the dynamical matrix elements for a unit cell are then given by,

$$D_{ab}^{\mathbf{k}}(i,j) = \frac{1}{\sqrt{M_i M_j}} \sum_l K_{ab}(i0, jl) e^{i\mathbf{k} \cdot (\mathbf{r}_{jl} - \mathbf{r}_{i0})}, \tag{1.72}$$

where a phase factor depending on the equilibrium positions of atoms $\mathbf{r}_{il}$ is introduced. Eigenvectors from $D_{ab}^{\mathbf{k}}(i,j)$ are now complex and have the $\mathbf{k}$-vector as an additional *quantum number* for a complete labelling.

In practice, to calculate local vibrational modes, equation 1.71 is used, with the second derivatives $K_{ab}(i,j)$ obtained from the *ab-initio* code. This involves moving all atom-pairs along Cartesian directions, and calculating the variation of the total energy.

For localised modes, only a few atoms are necessary to include in D: specifically the defect atoms and their neighbours. This is because in these modes only the nearest atoms have considerable amplitude on $\mathbf{U}$. However, modes which lie close to the crystal vibrational band edges are better described if additional neighbours are included. This is easily accomplished if the force constants are derived from an empirical potential such as the one proposed by Musgrave and Pople (1962). Here the potential for atom i is

$$V_i = \frac{1}{4} \sum_j k_r^{(i)} (\Delta r_{ij})^2 + \frac{r_0^2}{2} \sum_{i>k} k_\theta^{(i)} (\Delta \theta_{jik})^2 + r_0 \sum_{k>j} k_{r\theta}^{(i)} (\Delta r_{ij} + \Delta r_{ik}) \Delta \theta_{jik} +$$
$$+ \sum_{k>j} k_{rr}^{(i)} \Delta r_{ij} \Delta r_{ik} + r_0^2 \sum_{l>k>j} k_{\theta\theta}^{(i)} \Delta \theta_{jik} \Delta \theta_{kil}. \tag{1.73}$$

where Δr_{ij} and $\Delta \theta_{jik}$ are the changes in the $i - j$ bond length and the angle between $i - j$ and $i - k$ bonds. The sums run over the nearest neighbours of atom i, and the coefficients $k^{(i)}$ are fitted in order to reproduce well known experimental quantities, like elastic constants, Raman frequency, etc.

1.8.5 Stress-energy tensor

An important characteristic of a defect with lower symmetry than the host crystal, is the stress-energy tensor or piezospectroscopic tensor B (Watkins, 1996). In the absence of

any imposed stress, isolated defects are equally distributed over all equivalent orientations related by the symmetry of the crystal. However, applying a compressive stress across a particular direction results in an increase in energy of those defects exerting a compressive stress along this direction, and a decrease in energy of those which impose a tensile stress.

Let us suppose that we have a volume V_0 of cubic crystal under strain, containing N defects, N_i of which are oriented along direction i. In the elastic regime, the total energy is

$$E = E_0 + NE_f + \frac{V_0}{2} \boldsymbol{\epsilon} \cdot \mathsf{C} \cdot \boldsymbol{\epsilon} + \sum_i N_i \, \mathsf{B}^{(i)} \cdot \boldsymbol{\epsilon}, \tag{1.74}$$

subject to the condition $N = \sum_i N_i$. The first term is the total energy of the perfect crystal in the absence of external strain $\boldsymbol{\epsilon}$. The second term is the formation energy of all defects. The third term is the strain energy stored in the crystal with elastic coefficients C_{klmn}, and finally, the elements of the traceless second rank tensor $\mathsf{B}^{(i)}$ are given by

$$B_{lm}^{(i)} = \frac{\partial E_f^{(i)}}{\partial \epsilon_{lm}}, \tag{1.75}$$

represent the variation of the formation energy $E_f^{(i)}$ of a defect oriented along i, with respect to strain. Provided that $\sum_i \mathsf{B}^{(i)}$ is diagonal, if all equivalent orientations are equally distributed ($N_i = N_j$ for all i and j), and

$$\sum_i N_i \, \mathsf{B}^{(i)} \cdot \boldsymbol{\epsilon} = \frac{N}{3} \operatorname{Tr} \mathsf{B} \left(\epsilon_{11} + \epsilon_{22} + \epsilon_{33} \right). \tag{1.76}$$

At the equilibrium, $\partial E / \partial \epsilon_{ij} = 0$, leading us to a traceless tensor B.

Assuming no interaction between defects, each one has its own partition function. Given r possible orientations, the probability p_i of finding a defect aligned along i is

$$p_i = e^{-\beta \, \mathsf{B}^{(i)} \cdot \boldsymbol{\epsilon}} / \sum_j^r e^{-\beta \, \mathsf{B}^{(j)} \cdot \boldsymbol{\epsilon}}, \tag{1.77}$$

with $\beta = 1/k_{\mathrm{B}}T$, and hence for two different alignments we have,

$$\frac{p_i}{p_j} = e^{-\beta\left(\mathsf{B}^{(i)} - \mathsf{B}^{(j)}\right)\cdot\epsilon} \quad \text{subject to} \quad \sum_i^r p_i = 1. \tag{1.78}$$

Both expressions in 1.77 and 1.78 are used in experiments to obtain the B_{lm} components. Uniaxial stress at a predefined temperature T is applied to the sample, where after waiting long enough, defects will reach an equilibrium alignment distribution given in Equation 1.77. The probability values p_i, are then measured, as they are proportional to the intensity of some spectroscopic signal. Note that not all B_{lm} components are independent. The stress-tensor is:

1. Traceless, i.e., $B_{11} + B_{22} + B_{33} = 0$. This condition follow from the fact that in the absence of stress, all defects are randomly aligned, and the volume derivative of the energy must vanish at the equilibrium;

2. Symmetric ($B_{lm} = B_{ml}$);

3. Symmetric with respect to any symmetry operation R of the point-group of the defect, $\mathsf{R}^{-1} \cdot \mathsf{B} \cdot \mathsf{R} = \mathsf{B}$.

To calculate the stress-tensor for a defect, we deform the defective supercell with a set of strain tensors compatible with the symmetry of the defect, and solve Equation 1.75. This procedure can be preceded by a volume relaxation of the supercell, imposing the traceless condition. If the volume is not relaxed, an extra volumetric component is included in a non-traceless stress-energy tensor B'. Using Equations 1.76 and 1.74, and assuming only volumetric distortions in a cubic material ($\epsilon_{ii} = \epsilon$ and $B = (C_{1111} + 2\,C_{1122})/3$), we now have

$$E = E_0 + N E_f + \frac{9}{2} V_0\, B\, \epsilon^2 + N \operatorname{Tr} \mathsf{B}'\, \epsilon, \tag{1.79}$$

where B is the crystal bulk modulus. To find the volume change per defect $\Delta V/N = (V - V_0)/N$ we simply solve $\partial E/\partial \epsilon = 0$, to find that

$$\frac{\Delta V}{N} = -\frac{1}{3B} \operatorname{Tr} \mathsf{B}'. \tag{1.80}$$

Comparing Equations 1.74 and 1.79, we conclude that

$$\mathsf{B} = \mathsf{B}' - \frac{1}{3} \operatorname{Tr} \mathsf{B}'. \tag{1.81}$$

Using equations 1.80 and 1.81, we can calculate the anisotropic stress-energy tensor elements B_{lm}, as well as predict the volume relaxation of the crystal for a specific defect density.

1.8.6 Migration and reorientation barriers

To calculate the activation energy for the diffusion (or reorientation) of a defect, the saddle point lying in the pathway between translationally equivalent (or symmetrically equivalent) sites must be found (Flynn, 1972). This can be achieved by relaxing the cell subject to some constraint preventing the defect from returning to its equilibrium site. In some cases this can be done by constraining the symmetry of the defect and in others by imposing algebraic constraints on bond lengths in a way described previously (Jones *et al.*, 1991). These type of constraints are ideal for situations where in the saddle-point some bond between atoms i and j is about to be broken, and the $i - k$ bond is about to be created. Appropriate constraints are then:

$$c = |\mathbf{R}_i - \mathbf{R}_j|^2 - |\mathbf{R}_i - \mathbf{R}_k|^2, \tag{1.82}$$

with $c = 0$ when the $i - j$ and $i - k$ distances are equal. All the atoms in the cell are relaxed subject to c taking specific values. Using this procedure, the configuration energy surface can be found as a function of c and the barrier estimated by interpolation (Jones *et al.*, 1991). Previously this method was used to find the saddle-point configuration of interstitial oxygen in Si (Newman and Jones, 1994).

1.9   Convergence criteria

There are several convergence criteria that must be addressed: the cut-off in the Fourier expansion of the charge density, the number of shells of vectors $\mathbf{L_n}$ required to evaluate the Madelung energy (see Ewald method in Subsection 1.7.5), the mesh of special $\mathbf{k}$-points used to sample the band structure energy, the exponents used in the Gaussian basis functions and the size of the supercell. These criteria are not independent of each other and several iterations are needed to generate satisfactory values. Having selected a basis and supercell, the first three are easily dealt with: The number of shells of lattice vectors, the terms in the Fourier expansion and the number of $\mathbf{k}$-points generated by a MP-scheme are increased until the energy changes by less than 0.001 a.u. per atom.

The Fourier transform of the charge density includes reciprocal lattice vectors $\mathbf{g}$ corresponding to kinetic energies up to 80 a.u. for Si and Ge, and 300 a.u. when oxygen is included in the cell. The large cut-offs arise from the use of the BHS pseudopotentials and the lack of an occupied core p-orbital for oxygen.

The convergence criteria involving the number of Gaussian exponents and the size of the supercell are more problematic. The wavefunction basis consists of N Gaussian s- and p-orbitals, each specified by an exponent and located at the nuclei, and M similar orbitals located at each bond centre to simulate the effect of higher order angular momentum functions like d-orbitals. The Gaussian exponents for Si, O and Ge were found by minimising the energy of a cell containing bulk material or a disiloxane molecule $O-(Si-H_3)_2$. The exponents were selected in the range between 0.1 and 3.6 a.u. by using a Metropolis-like algorithm. All the exponents used are given in Table 1.1.

The table also shows that the calculated lattice parameters and bulk moduli for Si and Ge lie within 1% of the experimental values and that these structural parameters have converged for the smallest (4, 1) basis set. As a test, the structure of α-quartz was also evaluated and the lattice parameters found to be within 0.6% of the observed values with the (4, 1) Si and (6, 1) O basis.

The energy, however, is much more sensitive to the basis and Table 1.2 shows its variation

Table 1.1: Basis exponents (a.u.) for $s-$ and p-Gaussian orbitals for Si, Ge and O. AC refers to orbitals sited at atoms while BC refers to those sited at bond centres. (N, M) refer to numbers of orbitals placed at nuclei and at bond centres respectively. Lattice parameters a_0 (Å), the bulk moduli B (GPa), found from the basis sets are also given. Experimental values for a_0 and B from James and Lord (1992) and Singh (1993) respectively.

Species	Silicon		Germanium		Oxygen	
(N, M)	$(4, 1)$	$(4, 2)$	$(4, 1)$	$(4, 2)$	$(6, 1)$	$(6, 2)$
	0.1454	0.1272	0.1499	0.1509	0.2043	0.2815
	0.5002	0.3938	0.3747	0.4008	0.4339	0.5470
AC	1.2102	1.1592	0.9369	0.9018	0.9409	1.1665
	3.5712	3.1164	2.3422	2.4433	2.2011	2.5534
					4.7881	5.3166
					10.3587	11.4959
	0.1946	0.1474	0.1632	0.1435	0.4624	0.2081
BC		0.3838		0.3824		0.4238
a_0 (calc.)	5.390	5.394	5.579	5.568		
B (calc.)	99.5	94.3	76.3	74.2		
a_0 (obs.)	5.431		5.658			
B (obs.)	97.9		77.2			

Table 1.2: Total energies (a.u.) for bulk Si and α-quartz. The formation energy (eV), for an interstitial oxygen centre was evaluated using equation 1.62, and is given in the right hand column.

Basis				
Si	O	$E_{2\mathrm{Si}}$	$E_{3\mathrm{SiO}_2}$	$E_f(\mathrm{O}_i)$
$(3,0)$	$(6,0)$	-7.8623	-108.1744	1.989
$(3,1)$	$(6,1)$	-7.9187	-108.4906	1.973
$(4,1)$	$(6,1)$	-7.9271	-108.5423	1.809
$(4,2)$	$(6,2)$	-7.9309	-108.5485	1.817
$(4,3)$	$(6,3)$	-7.9317	-108.5502	1.820

with different (N, M) values. Here the energies for primitive cells of Si and α-quartz were evaluated using a MP-8^3 sampling mesh and fixed cell parameters equal to the converged values. It is clear that for the (4, 1) Si basis, the absolute energy per atom of bulk Si is in error by as much as 0.05 eV. Similarly, the Si (4, 1) and O (6, 1) basis produces an error in the total energy of a unit cell of quartz of 0.008 a.u. or 0.2 eV.

The absolute energy is, however, not of major concern. Of greater interest are the formation energies of defects and their relative energies (Subsection 1.8.2). The chemical potentials for Si and Ge are simply the energies per atom in the bulk phase. When dealing with oxygen defects in Si, we take μ_{O} to be given by the energy of an oxygen atom in α-quartz, namely $\mu_{\mathrm{O}} = (E_{3\mathrm{SiO}_2} - 3\mu_{\mathrm{Si}})/6$. A similar equation involving GeO_2 gives the chemical potential for oxygen in Ge. The formation energy then gives the equilibrium density of oxygen atoms in Si (Ge) when in equilibrium with SiO_2 (GeO_2).

The chemical potentials vary substantially with the basis as discussed above but the formation energies E_f of defects calculated using a consistent basis are much less sensitive. This is illustrated in Table 1.2 which shows that E_f for interstitial oxygen in Si has converged to within 10 meV, for the (4, 1) Si and (6, 1) O basis. These calculations used 64 Si cells and MP-2^3 sampling.

Table 1.3: Energy per silicon atom and formation energy of O_i in Si, eV, evaluated in several supercells and sets of special **k**-points. *scN*, *fccN*, and *bccN* refers to simple cubic, faced centred cubic, and body centred cubic lattices containing N Si atoms; n denotes the MP-n^3 sampling grid used.

Supercell	n	E_{Si}	$E_f(O_i)$	
			Calc.[a]	Calc.[b]
*sc*64	1	-107.7433	1.06	
*fcc*128	1	-107.7577	1.38	1.1
*sc*216	1	-107.8393	1.66	
*bcc*32	2	-107.8452	1.83	1.8
*sc*64	2	-107.8534	1.81	
*sc*8	20	-107.8549		

[a]This work.

[b]From Pesola *et al.* (1999*a*)

We now discuss the effect of different sized supercells and sampling schemes. For this the basis was fixed to be Si (4, 1) and O (6,1) and the unit cells volume was relaxed. Table 1.3 shows that using a single **k**-point at Γ in a 64 Si atom cell gives an error in the energy per atom of about 0.1 eV but this deceases to about 0.0015 eV for an MP-2^3 scheme Monkhorst and Pack (1976). Thus in 64 atom cells, we invariably used this scheme. The MP-1^3 sampling scheme was only used in 216 atom cells. Also shown, is the formation energy of O_i. Here it is clear that the use of MP-1^3 sampling gives poor energies except in the largest 216 atom cells.

To check the effect of the size of the supercell on the defect, the volume of the cell ought to be relaxed. Defects can exert strong compressive or tensile stresses, and the total energy per cell is reduced by expanding or contracting the lattice.Whereas each defect gives a finite volume change – irrespective of the volume of the supercell – the fractional volume change should vanish in the limit of large cells. The magnitude of this change is then a

measure of the sensitivity to cell size.

1.10   Summary

The DFT formalism has been presented as an accurate method for solving the ground state of a many-electron problem. In its formalism, the charge density is used as a variational variable, without introduction of approximations. Unfortunately, an exact exchange-correlation functional is still unknown. The LDA form of this functional was used throughout this thesis. In this sense, DFT might be seen as a pragmatic approach, allowing us to explore larger problems than those solvable with the all-electron Schrödinger equation.

The pseudopotential method, also plays a key role. Without them, the problem of a simple Ge atom would be as costly as that of a small cluster made of $\sim$10 *pseudo* Ge atoms. This allows us to model defects embedded in supercells with up to $\sim$200 group-IV atoms (plus the defect).

Finally, bearing in mind that we are using a ground-state theory, we must acknowledge the variety of observables that we are allowed to accurately predict. These include optical, mechanical and thermodynamic properties, which combined with the experiments, allows us to grasp many microscopic properties of defects in semiconductors.

Chapter 2

Experimental survey

2.1 Electron Paramagnetic Resonance

From a spectroscopic point of view, electron paramagnetic resonance (EPR) forms the basis for one of the most powerful techniques of defect characterisation. With it, valuable information concerning the microstructure of defects in crystals can be readily obtained. The wavefuction symmetry of a paramagnetic state, the site symmetry and identity of nearby atoms with a finite nuclear magnetic moment, and the angular-momentum character of the resonant electron are examples of properties that can be directly observed (Watkins, 1999; Bourgoin and Lannoo, 1983; Stoneham, 1975). Complementary techniques can be used to extract even more information. Stress alignment and its thermal recovery, has proven to be extremely efficient in providing new insights on defects (Watkins and Corbett, 1961a; Watkins, 1975).

2.1.1 Zeeman splitting

An unpaired electron within a spherically symmetric potential, possesses both orbital and intrinsic angular momenta $\mathbf{L}$ and $\mathbf{S}$ with amplitudes L and S quantised by integers l and s respectively, *i.e.,*

$$L = \sqrt{l(l+1)}\hbar \qquad\qquad l = 0,\, 1,\, \dots \qquad\qquad (2.1)$$

$$S = \sqrt{s(s+1)}\hbar \qquad\qquad s = \frac{1}{2},\, 1,\, \dots \qquad\qquad (2.2)$$

The respective magnetic moments $\boldsymbol{\mu}_L$ and $\boldsymbol{\mu}_S$ contribute to a total magnetic moment $\boldsymbol{\mu}$,

$$\boldsymbol{\mu} = \boldsymbol{\mu}_L + \boldsymbol{\mu}_S = -\mu_B\, g_L\, \mathbf{L} - \mu_B\, g_S\, \mathbf{S}, \qquad\qquad (2.3)$$

where μ_B is a proportionality factor of $e\hbar/2m_e c$, known as the Bohr magneton, $g_L = 1$ and $g_S = 2.0023$ are the so called *g-values* associated with $\mathbf{L}$ and $\mathbf{S}$.

In a solid the unpaired electron also experiences a crystal field composed of valleys and saddles, and as shown by van Vleck (1932), the angular momentum can be quenched. Nevertheless, the unpaired spin distribution induces a small magnetic momentum via spin-orbit coupling. This is taken into account by expressing the total magnetic moment with an effective **g**-tensor instead of the previous *g*-value. Therefore

$$\boldsymbol{\mu} = -\mu_B\, \mathbf{g} \cdot \mathbf{S}, \qquad\qquad (2.4)$$

where **g** is now a second rank tensor that mirrors the anisotropy of the spin density distribution and its orientation relative to some axial system. This new information arises from the induced magnetic dipole on atoms surrounding the unpaired electron. Bearing this in mind, one can divide **g** into an isotropic term equal to $g_e = 2.0023$ (corresponding to the g value of a free electron), and a deviation $\Delta\mathbf{g}$ carrying the signature of the environment,

$$\mathbf{g} = g_e \cdot \mathbf{I} + \Delta\mathbf{g}. \qquad\qquad (2.5)$$

Here $\mathbf{I}$ is the unit matrix. $\Delta\mathbf{g}$ can be evaluated by perturbation theory, where a spin-orbit coupling term $\lambda\,\mathbf{L} \cdot \mathbf{S}$ is expanded to second order. Thus, if $|n\rangle$ and $|0\rangle$ represent excited

and ground states with energies E_n and E_0 respectively, as Bourgoin and Lannoo (1983) shown,

$$\Delta \mathbf{g} = -2\lambda \sum_n \frac{\langle 0 \left| L \right| n \rangle \langle n \left| L \right| 0 \rangle}{E_n - E_0}. \tag{2.6}$$

A steady magnetic field $\mathbf{H}$ along an arbitrary direction couples with $\boldsymbol{\mu}$, resulting in a Hamiltonian $\mathcal{H}_{Ze}$, where

$$\mathcal{H}_{Ze} = \mu_B \, \mathbf{H} \cdot \mathbf{g} \cdot \mathbf{S}. \tag{2.7}$$

The $(2S + 1)$ degenerate electronic states are now split. This phenomenon is called the Zeeman splitting. For a particular direction of the magnetic field given by a unit vector $\mathbf{h}$, the electron spin can be considered as quantised along an effective magnetic field $H \, \mathbf{h} \cdot \mathbf{g} = H \left| \mathbf{h} \cdot \mathbf{g} \right| \mathbf{h}_s$ with direction $\mathbf{h}_s$. This allows us to approximate the energy eigenvalues from the Hamiltonian in 2.7, using the azimuthal spin quantum number m_s as follows,

$$E = \mu_B \, H \, m_s \, \mathbf{h} \cdot \mathbf{g} \cdot \mathbf{h}_s = \mu_B \, H \, m_s \, \frac{(\mathbf{h} \cdot \mathbf{g}) \cdot (\mathbf{g} \cdot \mathbf{h})}{\left| \mathbf{g} \cdot \mathbf{h} \right|}, \tag{2.8}$$

where the allowed transitions, for which $\Delta m_s = \pm 1$, occur between equally spaced levels separated by

$$\Delta E = \mu_B \, H \sqrt{\mathbf{h} \cdot \ \mathbf{g}^2 \cdot \mathbf{h}} = \mu_B \, H \, g. \tag{2.9}$$

Note that here the direction of $\mathbf{H}$ is fixed, and therefore the $\mathbf{g}$-tensor is contracted towards a scalar. The Zeeman splitting between $m_s = \pm 1/2$ states is shown as t_0 in Figure 2.1. For magnetic fields of the order of ~ 1 T, the energy separation $\mu_B \, H \, g$ typically corresponds to photon frequencies of 1 - 30 GHz (microwave region). Monitoring electronic transitions between Zeeman states is the basis of EPR. In practice it is difficult to have a source of microwaves tunable in a wide enough spectral region. Instead, this one is fixed with some frequency ω, and the magnetic field $\mathbf{H}$ is allowed to vary until resonance occurs.
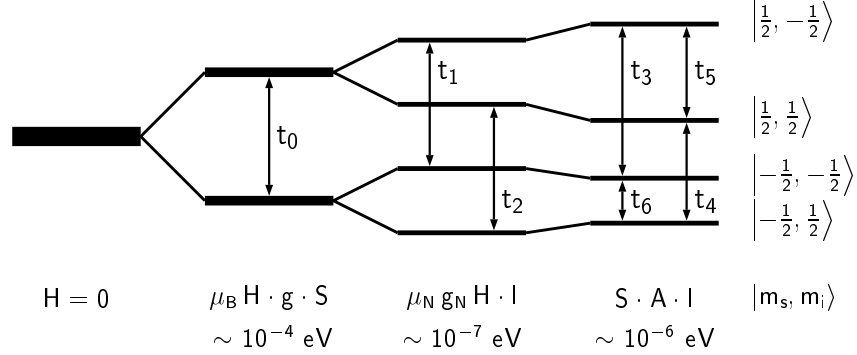
Figure 2.1: Energy levels of a system with $S = 1/2$ and $I = 1/2$ under influence of a magnetic field. EPR transition are allowed when $\Delta m_s = \pm 1$ and $\Delta m_i = 0$, whereas for ENDOR the selection rules are $\Delta m_s = 0$ and $\Delta m_i = \pm 1$.

2.1.2 Angle dependent patterns

As defined in Subsection 2.1.1, the coupling between the unpaired spin associated with a defect state and an external magnetic field is mediated through a tensor $\mathbf{g}$. The Hamiltonian was then found to have solutions which are proportional to $\sqrt{\mathbf{h} \cdot \mathbf{g}^2 \cdot \mathbf{h}}$. Expressing the unit vector $\mathbf{h}$ in terms of the angles θ_i that it makes with the Cartesian axes ($i = 1, 2, 3$), the quantity inside the square root can be expanded to

$$g^2 = \mathbf{h} \cdot \mathbf{g}^2 \cdot \mathbf{h} = \sum_i \left[\mathbf{g}^2\right]_{ii} \cos^2 \theta_i + 2 \sum_k \varepsilon_{ijk} \left[\mathbf{g}^2\right]_{ij} \cos \theta_i \cos \theta_j, \qquad (2.10)$$

where $\left[\mathbf{g}^2\right]_{ij}$ represent the tensorial element indexed by the i, j pair, and $\varepsilon_{ijk} = 1$ if $i \neq j \neq k \neq i$, and zero otherwise. In silicon crystals, a defect transforming within a point group G of order g_G, can take $24/g_G$ different orientations (Kaplianskii, 1964). Hence, each of the $24/g_G$ different $\mathbf{g}$-tensor orientations correspond to a g^2-value in Equation 2.10, and therefore to an individual EPR resonance. However, since in practice the magnetic field is kept in the $(0\bar{1}1)$ plane, one is restricted to 12 orientations (Sieverts, 1978). In this plane $\sin \theta_1 = \sqrt{2} \cos \theta_2 = \sqrt{2} \cos \theta_3$, allowing us to drop the indexes, and rewrite Equation 2.10 for any orientation of $\mathbf{H}$ within the plane,
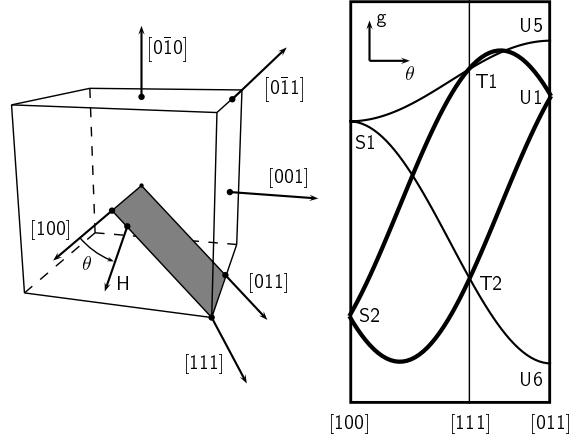
Figure 2.2: Angular variation of the magnetic field **H** relative to the cubic crystallographic axes in an EPR experiment (left). Angular dependence of a spin-half rhombic-I symmetry (C_{2v}) EPR signal (right). Thick and thin lines are doubly and non degenerate defect orientations relative to **H**.

$$g^2 = g_{11}^2 \, \cos^2 \theta + \frac{1}{2} \left(g_{22}^2 + g_{33}^2 \right) \sin^2 \theta + \frac{1}{2} \left(g_{12}^2 + g_{13}^2 \right) \sin \theta \, \cos \theta + g_{23}^2 \, \sin^2 \theta. \qquad (2.11)$$

If the defect possesses any structural symmetry, say that all atomic coordinates can be transformed within the symmetry operator R, then additional constraints will be imposed on the g-tensor, i.e., $R^{-1} \cdot g \cdot R = g$. For example, if a paramagnetic defect possesses C_{2v} symmetry, the number of distinct orientations is reduced to 6, and Equation 2.11 is further simplified to

$$g^2 = g_{11}^2 \, \cos^2 \theta + \left(g_{33}^2 + g_{23}^2 \right) \sin^2 \theta. \qquad (2.12)$$

The g^2 values corresponding to each orientation of the defect, are then monitored by varying the direction of the magnetic field . A typical EPR pattern for a C_{2v} defect is shown in the right-hand side of Figure 2.2,

The g-values for the [100], [111] and [011] high-symmetry directions, are commonly denoted as S-, T-, and U-values respectively. One can readily observe that not all *branches* have the

same thickness. Thicker lines correspond to more intense resonances due to orientational degeneracy (Kaplianskii, 1964). Hence, when **H** is along [100], only two orientations of defects are distinguishable: those with the C_2 axis parallel and perpendicular to **H**. However, there are twice as many defects axially perpendicular to **H** as those which are parallel to it. Therefore, for this particular orientation of **H**, the EPR signal contains two features, namely at S1 and S2, with an intensity ratio of 2:4. Here we preserve the total number of possible orientations $(6 = 4 + 2)$.

We can now appreciate how powerful the measurement of the **g**-tensor associated with a paramagnetic defect can be. It not only provides us with information about the symmetry of the centre, but also gives us the anisotropy character of the unpaired electron. The eigenvalues g_i and eigenvectors $\mathbf{g}_i$ of the **g**-tensor contain useful information. Very similar g_i elements indicate low anisotropy and vice versa. The principal directions inform us about the orientation of the paramagnetic spin density relative to the crystallographic axes. This kind of information is certainly priceless and unattainable by any other spectroscopic technique.

2.1.3 Hyperfine interaction

Until now, we considered the coupling between an external magnetic field and an unpaired spin. However, besides the external field, the electron is affected by other sources of magnetism within solids. In silicon, approximately 4.7% of the atoms belong to the ^{29}Si isotopic species, possessing an intrinsic nuclear spin $I = 1/2$. We can imagine these as magnetic dipoles inducing its own magnetic fields, much like the applied field (being however $\sim$2 orders of magnitude weaker). These give rise to the hyperfine interaction. In this Subsection, a description will be given about how information concerning a particular defect is extracted from these weak interactions.

Consider an isolated atom whose nucleus possesses an intrinsic angular momentum **I** where $I = \sqrt{i(i+1)}\,\hbar$ and $i = 0, \frac{1}{2}, 1, \ldots$. As for the electron, this nucleus has a magnetic moment

$$\mu_I = -g_N \, \mu_N \, \mathbf{I}, \tag{2.13}$$

where g_N is the nuclear g-value (for ^{29}Si, $g_N = 1.1095$), and μ_N the nuclear magneton. Analogously to μ_B, the nuclear magneton is $e\hbar/2Mc$, but M is now the nuclear mass. Atoms with non-zero $\mathbf{I}$ can interact with an unpaired electron, or with an external magnetic field. The last interaction is of Zeeman type, and in analogy with Equation 2.7, one can write a term to be added to the Hamiltonian as

$$\mathcal{H}_{Zi} = \mu_N \, \mathbf{H} \cdot \mathsf{g}_N \cdot \mathbf{I} = \mu_N \, g_N \, \mathbf{H} \cdot \mathbf{I}. \tag{2.14}$$

Note that in this situation we assume an interaction between $\mathbf{H}$ and a point like nuclear dipole moment. Therefore g_N is contracted to a scalar and the coupling is isotropic. A Zeeman-nuclear interaction for a system with $I = 1/2$ is shown in Figure 2.1 involving a second splitting. Two associated EPR transitions are also indicated by t_1 and t_2. These correspond to $\Delta m_s = \pm 1$ and $\Delta m_i = 0$, where m_s and m_i are the azimuthal quantisations of the electronic and nuclear angular momenta.

Now if an atom with non-zero nuclear magnetic moment is in the neighbourhood of a paramagnetic defect, another type of hyperfine interaction can be observed. This can be thought as arising from the interaction between a local magnetic field $\mathbf{H}_{\mathrm{loc}} \propto \mathsf{A} \cdot \mathbf{I}$ induced by a magnetic nucleus, and the electronic spin, i.e.,

$$\mathcal{H}_{SI} = \mathbf{S} \cdot \mathsf{A} \cdot \mathbf{I}, \tag{2.15}$$

where A is referred as hyperfine tensor. On the extreme right of Figure 2.1, the effect of this coupling is shown, and now EPR transitions (labelled as t_3 and t_4) do not possess the same energy. We see that $\Delta E(t_4) \leq \Delta E(t_0) \leq \Delta E(t_3)$, implying that the EPR spectra will be composed of strong absorption lines due to t_0 transitions, plus a certain number of low- and high-energy side bands with intensity depending on the number of equivalent

nuclei giving rise to each particular sideband. We can now write the spin-Hamiltonian normally adopted for paramagnetic defects in semiconductors,

$$\mathcal{H} = \mathcal{H}_{Ze} + \mathcal{H}_{Zi} + \mathcal{H}_{SI} = \mu_B \, \mathbf{H} \cdot \mathsf{g} \cdot \mathbf{S} + \sum_k \left(\mu_N^{(k)} \, g_N^{(k)} \, \mathbf{H} \cdot \mathbf{I}^{(k)} + \mathbf{S} \cdot \mathsf{A}^{(k)} \cdot \mathbf{I}^{(k)} \right), \quad (2.16)$$

where the summation (taken over all atoms for which $I \neq 0$) can eventually be substituted by a term expressing the location and statistical abundance of the corresponding atomic species. The hyperfine tensor $\mathsf{A}^{(k)}$ as we shall see next, contains detailed information concerning the shape of the wavefunction near atom k.

The electron-nuclear hyperfine contribution in 2.16 can be described as dipole-dipole interaction between two magnetic dipole moments separated by a vector $\mathbf{r}$. Assuming only one magnetic nucleus, the operator associated with this observable can be written as

$$\mathcal{H}_{SI} = g \, \mu_B \, g_N \, \mu_N \left[\left(\frac{3 \, (\mathbf{S} \cdot \mathbf{r}) \, (\mathbf{I} \cdot \mathbf{r})}{r^5} - \frac{\mathbf{S} \cdot \mathbf{I}}{r^3} \right) + \frac{8}{3} \pi \, \mathbf{S} \cdot \mathbf{I} \, \delta(r) \right]. \quad (2.17)$$

Here the first term is the classical dipole-dipole interaction, but a second term, called the Fermi contact interaction, must be included. The Fermi contact interaction is non-zero for spin-densities which have an s-like component at the nucleus. We can then separate the hyperfine interaction into isotropic and anisotropic parts, say with corresponding operators $\hat{a}$ and $\hat{b}$,

$$\widehat{a} = \frac{8}{3} \pi \, g \, \mu_B \, g_N \, \mu_N \, \mathbf{S} \cdot \mathbf{I} \, \delta(r) \quad (2.18)$$

$$\widehat{b} = g \, \mu_B \, g_N \, \mu_N \, \left(\frac{3 \, (\mathbf{S} \cdot \mathbf{r}) \, (\mathbf{I} \cdot \mathbf{r})}{r^5} - \frac{\mathbf{S} \cdot \mathbf{I}}{r^3} \right), \quad (2.19)$$

where $\mathcal{H}_{SI} = \widehat{a} + \widehat{b}$. We can now write a spin-Hamiltonian describing the hyperfine effects arising from a particular electronic wavefunction ψ,

$$\mathcal{H}_{SI} = \mathbf{S} \cdot \mathsf{A} \cdot \mathbf{I} = \langle \psi | \widehat{\mathcal{H}}_{SI} | \psi \rangle = \langle \psi \, | \widehat{a} | \, \psi \rangle + \langle \psi | \widehat{b} | \psi \rangle = \mathbf{S} \cdot \mathsf{a} \cdot \mathbf{I} + \mathbf{S} \cdot \mathsf{b} \cdot \mathbf{I}. \quad (2.20)$$

In this way, the hyperfine tensors a and b mirror the local amplitude and angular variation of the unpaired wavefunction around a particular atom. Experimental determination of A follows the same procedure as that for g. Providing that hyperfine peaks can be resolved, the direction of the magnetic field is varied in the $(0\bar{1}1)$ plane, and again, sinusoidal patterns are observed. However, these can be much more complicated that those arising from the electron-Zeeman splitting since several sidebands can appear in a narrow spectral region. These patterns provide us with an immense amount of information, and for practical proposes only some values at S-, T- and U- are necessary to define A (Sieverts, 1978). Another important feature of the hyperfine interaction analysis is the fact that all symmetry equivalent magnetic nuclei will contribute to the same band. Here $\mathsf{A}^{(m)} = \mathsf{R}^{-1} \cdot \mathsf{A}^{(n)} \cdot \mathsf{R}$, where R relates both m and n equivalent atoms, and consequently the EPR signals arising from both nucleus will be superimposed (Kaplianskii, 1964). We then say that each hyperfine band arises from a *shell* of symmetrically equivalent magnetic nuclei.

2.1.4 LCAO analysis of the hyperfine spectra

As we concluded from Equation 2.20, the hyperfine tensor A quantifies the coupling between a nuclear magnetic dipole and the electron spin density. Isotropic and anisotropic tensors a and b were then defined for a general shape of the electronic wavefunction. In practice, wavefunctions associated with gap-states are normally approximated as linear combination of atomic orbitals ϕ_i (LCAO) centred on each atom i near the defect (Slater, 1965, p. 203). Hence,

$$\psi(\mathbf{r}) = \sum_i \eta_i \, \phi_i(\mathbf{r}), \qquad (2.21)$$

where $\sum_i \eta_i^2 = 1$. The atomic orbitals ϕ_i are normally chosen to be composed of hybridised $sp-$ functions $f_{s,i}$ and $f_{p,i}$,

$$\phi_i(\mathbf{r}) = \alpha_i \, f_{s,i}(\mathbf{r}) + \beta_i \, f_{p,i}(\mathbf{r}), \qquad (2.22)$$

with $\alpha_i^2 + \beta_i^2 = 1$. The LCAO interpretation of A was pioneered by Watkins and Corbett (1961a) and shown to be extremely fruitful. From the parity of $f_{s,i}$ and $f_{p,i}$, Equation 2.20 can be written as

$$\left\langle \psi \left| \widehat{a}_{mn}^{(i)} \right| \psi \right\rangle = \delta_{mn} \frac{8\pi}{3} \, g \, \mu_B \, g_N \, \mu_N \, \eta_i^2 \, \alpha_i^2 \, f_{s,i}^2(\mathbf{0}) \tag{2.23}$$

$$\left\langle \psi \left| \widehat{b}_{mn}^{(i)} \right| \psi \right\rangle = g \, \mu_B \, g_N \, \mu_N \, \eta_i^2 \, \beta_i^2 \, \left\langle f_{p,i} \left| \frac{3 r_m r_n}{r^5} - \frac{\delta_{mn}}{r^3} \right| f_{p,i} \right\rangle . \tag{2.24}$$

Accurate self-consistent Hartree-Fock values for $f_{s,i}^2(\mathbf{0})$ and the integral in 2.24 are available in the literature for numerous atomic species. It is now evident from Equations 2.23 and 2.24, that the measurement of the isotropic and traceless tensors $\mathsf{a}^{(i)}$ and $\mathsf{b}^{(i)}$ respectively, lead to the knowledge of the localisation η_i^2 and the $s-$ and $p-$character of the wavefunction on atom i, i.e., α_i^2 and β_i^2 respectively. If the hyperfine tensor does not exhibit axial symmetry, its interpretation is more difficult (Sieverts, 1978). This is the case of shallow impurity states, where hyperfines are predominantly isotropic and LCAO normally breaks down. This kind of states are more accurately studied by means of effective-mass theory (see Section 2.5).

2.1.5 Observation of resonance

In a real experiment, transitions between two paramagnetic states (say t_0 in Figure 2.1), are driven by two mechanisms – radiation and thermal excitations. The former tends to equalise the defect populations n_- and n_+ for which $m_s = -1/2$ and $m_s = +1/2$ respectively. However, the second drives the occupancy of these states according to a Boltzmann law, which takes into account the fact that the defect is embedded in a thermal bath (Bourgoin and Lannoo, 1983). One can readily see that if the thermally activated process is not the fastest mechanism, it will be impossible to restore a steady state differential population $n_- - n_+ \neq 0$, and the transition probability will vanish along with the EPR signal. The rate at which the system relaxes to the thermal equilibrium is limited by the spin-lattice relaxation time, which is an intrinsic property of a particular material. Thus if W is the

$\left|\frac{1}{2}\right\rangle \rightarrow \left|-\frac{1}{2}\right\rangle$ or $\left|-\frac{1}{2}\right\rangle \rightarrow \left|\frac{1}{2}\right\rangle$ transition probability, and τ_{sl} the spin-lattice relaxation time of the material of interest, EPR signals would only be observable only if

$$W \tau_{\mathrm{sl}} \ll 1. \tag{2.25}$$

A semiconductor for which τ_{sl} is too short is germanium. Here the lines are broad and difficult to detect. Moreover, other sorts of difficulties can appear during an EPR experiment. For example, in materials where the most abundant isotopic species of its chemical components have a non-zero nuclear magnetic moment (like gallium arsenide), signals are normally hidden by a strong background of hyperfines. Fortunately this is not the case for silicon, which is the material of main interest in this thesis, where the spin-lattice time is sufficiently short, allowing sharp signals to be detected. Furthermore, the $\sim$4.7% natural magnetic ^{29}Si nuclei enable the observation of important hyperfine interactions.

2.1.6 Example: Si-A centre

The Si-A centre (or VO) is a secondary radiation induced defect, where an oxygen atom inside a vacancy bridges two second neighbouring Si atoms, leaving two unsatisfied Si-dangling bonds which collapse to form a weak Si-Si reconstruction (Watkins and Corbett, 1961a; Corbett et $al.$, 1961). This defect is shown on the left hand side of Figure 2.3. The EPR data concerning this defect can be summarised as follows (Watkins and Corbett, 1961a) — EPR activity arises from the negatively charged defect with an electron trap 0.17 eV below the conduction band. This is shown schematically on the right hand side of the same figure, where an extra electron populates an anti-bonding orbital close to the conduction band bottom. The pattern of the g values can be fitted assuming a C_{2v} symmetry g-tensor with principal values of 2.0093, 2.0025 and 2.0031 for g_1, g_2 and g_3, and principal directions along [110], [1$\bar{1}$0] and [001] respectively. Hyperfine interactions with 4.7% abundant ^{29}Si isotopes (with a nuclear magnetic moment $I = 1/2$), were resolved. These arise from five different shells, and from the relative intensities of the hyperfine signals, it was possible to estimate the number $N^{(i)}$ of equivalent Si atoms belonging to

Table 2.1: LCAO analysis of the Si-A centre from the ^{29}Si hyperfine signals measured by EPR (Watkins and Corbett, 1961a) and ENDOR (van Kemp et $al.$, 1989a). Shell labelling follow the original work. $N^{(i)}$ is the number of Si atoms in each shell, and α_i^2, β_i^2 and η_i^2 are the s and p character and relative localisation of the wavefunction on atoms from shell i respectively.

	Shell	A	B	C	D		E
	$N^{(i)}$	2	2	2	4 - 6		4 - 6
	α_i^2	0.37	0.26	0.25	0.25		$\sim$1
EPR	β_i^2	0.63	0.74	0.75	0.75		$\sim$0
	η_i^2	0.355	0.049	0.034	0.022		0.002
	Shell	$Mad1$	$Mad2$	$Mad3$	$Mad4$	$G1$	$G2$
	$N^{(i)}$	2	2	2	2	4	4
	α_i^2	0.302	0.195	0.188	0.236	0.171	0.203
ENDOR	β_i^2	0.698	0.805	0.812	0.764	0.829	0.797
	η_i^2	0.300	0.044	0.031	0.016	0.021	0.009

shell i. Using an LCAO analysis it was concluded that most part of the spin density is localised around a shell (labelled A) with two Si atoms (see Table 2.1). Shells with 4-6 atoms were also reported. However, we must bear in mind that a C_{2v} symmetry defect only has shells where $N^{(i)}$ is 1, 2 or 4. Unequivocal evidence about $N^{(i)}$ can be obtained if a resolved signal could be monitored with different orientations for **H**, allowing the precise site-symmetry to be found. Experiments with samples containing the magnetic ^{17}O isotope did not reveal any O-related hyperfine.

Although detailed information about the ground state of VO$^{(-)}$ was provided by EPR, an even richer picture has been reported using electron-nuclear double resonance (ENDOR). This technique, much more sensitive than EPR, was pioneered by Feher (1959a). Here a powerful microwave source quenches the EPR signal by equally populating ground and excited states with $\Delta m_i = 0$, giving rise to a differential population of states with $\Delta m_i \neq 0$.
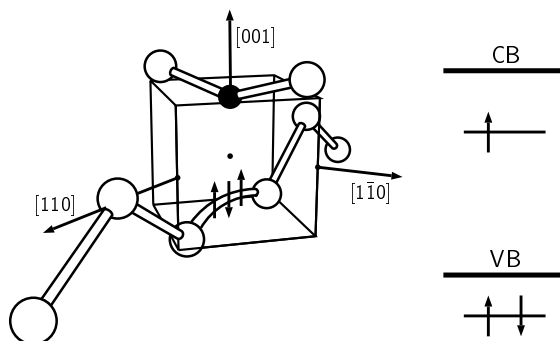
Figure 2.3: (left) Structure of the A-centre defect in Si, and (right) its level scheme in the negative charge state. Two paired electrons occupy a bonding state, and an unpaired electron occupies an anti-bonding level.

These correspond to transitions labelled as t_5 and t_6 in Figure 2.1. Angular patterns similar to those obtained in EPR for the hyperfine A, are then monitored during an ENDOR experiment.

Measurements of ^{29}Si ENDOR reveal a total of 50 distinct shells. The six strongest hyperfines are shown in Table 2.1. Among all, 1, 20, 6 and 23 of them have C_2, C_{1h}, C_{1h} and C_1 site-symmetry, and labelled as of T, Mad, Mbc and G-type respectively. Most of the spin-density was found to be localised on the $\{1\bar{1}0\}$ plane defined by the reconstructed Si-Si unit plus the O-atom (van Kemp *et al.*, 1989*a*). In Table 2.1 we can see a clear agreement between the LCAO analysis from the EPR and ENDOR hyperfines. Hyperfine interactions as far as 12 Å from the defect were resolved, despite the strong localisation of the wavefunction. A plot of η^2 vs shell-distance, shows that the wavefunction has higher amplitude on the Si atoms lying along the two semi-infinite [110]-chains, starting on both weakly bonded Si atoms respectively (see Figure 2.3). These Si-chains account for 81% of localisation.

Measurements of ^{17}O-ENDOR were also reported (van Kemp *et al.*, 1989*b*). Regardless of the fact that the O-atom sits at a nodal plane of the anti-bonding wavefunction, it was possible to detect oxygen-related ENDOR transitions. The isotropic component of the hyperfine interaction is about $a = 3$ MHz, corresponding to $\eta^2 \sim 0.06\%$, justified as arising

from spin-polarisation, or self-interaction effects. The anisotropic part of A correspond to a localisation of $\eta^2 = 1.18\%$ on a p-like orbital along the [110] direction.

2.2 Photoluminescence

Photoluminescence (PL) is an optical method for characterisation of light emitting centres, by means of photonic excitation. Other methods to produce luminescence can also be employed, such as accelerated electrons, electric fields, and heat, for cathode-, electro-, and thermo-luminescence respectively. Luminescence occurs when a system in an excited electronic state relaxes to a lower energy state by a radiative process. For reviews of this technique, see Davies (1981); Lightowlers (1990); Davies (1999), and in particular the detailed report on luminescent centres in silicon by Davies (1989).

2.2.1 Excitations in silicon

It is beyond the scope of this thesis to describe the PL technique in detail, and attention will be focused only on relevant issues to the present work, i.e., a brief description of bound-exciton luminescence in defective silicon crystals. Silicon has a 1.17 eV indirect band-gap (E_g), and in a PL experiment, the excitation source normally injects photons with energy $h\nu > E_g$, such that electron-hole (EH) pairs are created. Thermalisation of these pairs rapidly occurs, as they accumulate at the band edges.

Electrons and holes can relax via several routes, namely by being captured by carrier traps (defects), electron-hole recombination, and free-exciton (FE) formation (Lightowlers, 1990; Dean and Herbert, 1979). In the first process, defects are charged, and eventually discharged such thermodynamic equilibrium is recovered. In the last route, formation of free-excitons can be followed by FE-recombination or impurity trapping. Here we say that a bound-exciton (BE) is formed, which ultimately can decay via BE-recombination. Other processes which are less relevant to this work can also occur. In particular, with intense light sources, bound-multiexciton and electron-hole drops are normally observed

(Lightowlers, 1990). Note that the indirect gap in silicon makes FE annihilation possible only when accompanied by phonon emission, giving rise to long FE life-times of up to 60 μs in very pure crystals (Merle *et al.*, 1978), allowing them to migrate several hundreds of μm.[1] In the presence of defects the FE life-time decreases drastically due to capture and BE formation.

2.2.2 Vibronic coordinate diagram

Electronic transitions associated with defects are in principle accompanied by local bonding changes. We would then expect that the sudden change on the electronic charge density during the transition will also imply a change in the vibrational state. These coupled electronic-vibrational transitions are referred as *vibronic transitions*. In Figure 2.4 the configuration coordinate of a system is shown. Here the total energy of a crystal with some defect is shown as a parabola centred at the equilibrium atomic configurations (Q_g and Q_e for the ground and excited states respectively). This idealised system has one unique normal mode Q for atomic vibration. Assuming that the harmonic term of the inter-atomic potential is the same in both states,

$$E_g(Q) = \frac{1}{2}\mu\,\omega^2(Q - Q_g)^2 \tag{2.26}$$

$$E_e(Q) = h\,\nu_0 + \frac{1}{2}\mu\,\omega^2(Q - Q_e)^2, \tag{2.27}$$

where μ and ω are the reduced mass and frequency of an oscillator with a normal coordinate Q. As shown in Figure 2.4, both electronic states possess their own set of phonon states separated by $\hbar\omega$.

Now let us suppose that we populate the excited state by illuminating the system. For $T = 0$ K, thermalisation rapidly pulls the system towards the zero-phonon state with an energy of $h\,\nu_0 + \hbar\omega/2$. According to the Frank-Condon principle, light emission correspond to the downward bold transition in Figure 2.4, where the electronic state is changed in a much

---

[1] Here the FE diffusivity of 34 cm^{2}s^{-1} at 20 K was used (Cuthbert, 1970).
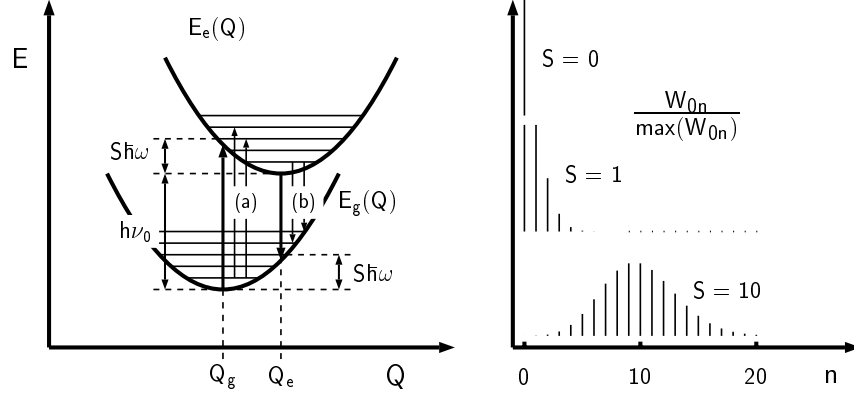
Figure 2.4: Configuration coordinate diagram for the ground and excited states around their equilibrium coordinates Q_g and Q_e respectively (left hand side). Absorption and emission processes are labelled as (a) and (b). Electronic transitions are assumed to be coupled by one unique normal mode Q. On the right side, relative intensities for n-phonon transitions at $T = 0$ K are given for three different degrees of coupling.

smaller time scale than atomic relaxation. However, real emission spectra are normally composed of several peaks, corresponding to the number of phonons created during the process. These are the (b) type vibronic transitions in the same figure, where 3 and 4 phonons are created respectively. At $T = 0$ K the transition probability associated with the creation of n phonons is given by

$$W_{0n} = \frac{S^n}{n!} e^{-S}, \tag{2.28}$$

where S is known as the Huang-Rhys factor. The physical significance of "S" can be understood as follows. If the excited state in (2.27) is expressed in terms of the ground state, we get a linear term in Q coupling the two states, i.e.,

$$E_e(Q) = \frac{1}{2}\mu\,\omega^2(Q - Q_g)^2 - \mu\,\omega^2\Delta Q \cdot Q + \frac{1}{2}\mu\,\omega^2(\Delta Q)^2 + h\nu_0, \tag{2.29}$$

where $\Delta Q = Q_e - Q_g$.

Hence, after a "vertical" excitation, the energy given by

70

$$E_e(Q_g) - E_g(Q_g) = \frac{1}{2}\mu\,\omega(\Delta Q)^2 = S\hbar\omega \tag{2.30}$$

is involved in phonon creation, and a "vertical" relaxation will most probably emit a photon with energy $h\nu_0 - S\hbar\omega$. Therefore S is the most probable number of phonons created (or annihilated) during the luminescence (or absorption) process.

A pure electronic transition (with no phonon creation) will occur with photon emission with an energy of $h\nu_0$. The spectral feature associated to this type of transition is normally referred as zero-phonon line (ZPL). However, if phonons are created, then a low energy side-band will appear below the ZPL. Since at $T = 0K$ the vibronic transition probability between the excited and ground states $|0, e\rangle$ and $|n, g\rangle$ is given by Equation 2.28, the total spectrum will be composed by the ZPL plus a series of equally spaced vibronic side bands. This is illustrated on the right hand side of Figure 2.4, where the probability of a series of vibronic transitions is shown for three different values of S. For $S = 0$ there is no electron-phonon coupling, and all transitions are purely electronic. For small values of S, $\Delta Q \neq 0$, and the n-th side-band will have an intensity proportional to W_{0n}. Finally, for high values of S (strong coupling), all vibronic side-bands are modulated by a curve which is asymptotically Gaussian centred on $h\nu_0 - S\hbar\omega$.

2.2.3 Free-exciton luminescence

Let $E_n(\mathbf{k})$ represent the electronic band structure for silicon. This is illustrated on Figure 2.5(a), where the one-electron Khon-Sham energy states are plotted along the (100), (110) and (111) cubic directions within the Brillouin-Zone (BZ). Here, conduction band minima occur at $\mathbf{k}_i = 0.86\,X$. When free electrons and holes travelling with the same group velocity, i.e., $\nabla_{\mathbf{k}}E_{\mathrm{c}} = \nabla_{\mathbf{k}}E_{\mathrm{v}}$, where subscripts c and b denote conduction and valence band states, they may be driven by their mutual Coulombic attraction and form free-excitons with well defined bound states. A simplistic approach, where the conduction and valence bands are assumed to be spherical in $\mathbf{k}$-space and non-degenerate, allows us to identify the electron-hole pair with an hydrogenic problem. Hence, for an electron orbiting
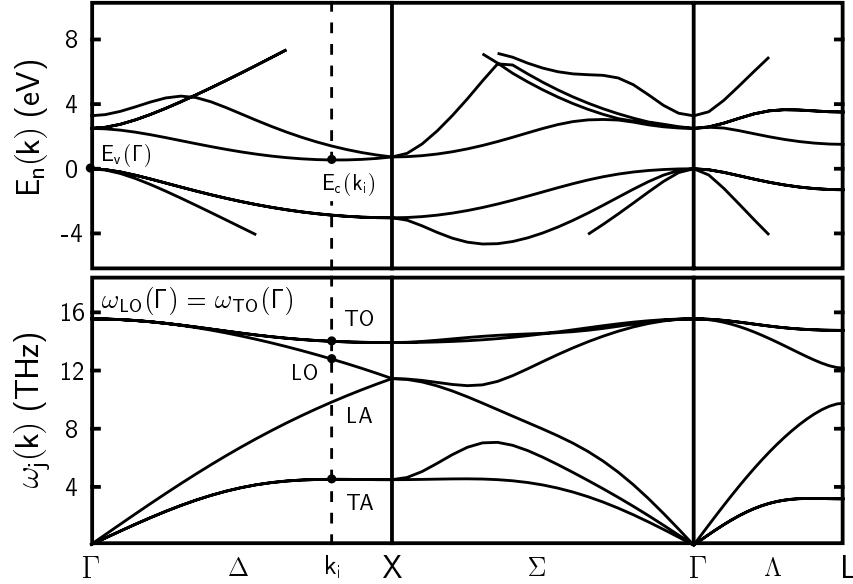
Figure 2.5: One-electron band structure $E_n(\mathbf{k})$ (top), and phonon dispersion relations $\omega_j(\mathbf{k})$ (bottom). Band gap $E_c(\mathbf{k}_i) - E_v(\Gamma) = 0.54$ eV is a consequence of LDA. The phonon dispersion curves were calculated using an extended Keating interatomic potential (Keating, 1966) described by Sangster *et al.* (1992).

around a hole screened by a medium with dielectric constant ϵ, the exciton bound states $E_x(n)$ are given by (Kittel, 1986),

$$E_x(n) = E_g - \frac{\mu\,e^4}{2\hbar^2\epsilon^2 n^2}, \tag{2.31}$$

where E_g, μ and n are the band-gap, the reduced mass of the electron-hole pair and the principal quantum number respectively. Given the ellipsoidal character and location in $\mathbf{k}$-space of the conduction band bottom in Si, a mass tensor must be used, and a more sophisticated approach is normally employed where band-extrema wavefunctions are used as a basis set to describe the exciton states (Cho, 1979). In this case s and p states are split due to the non-spherical conduction band minima as described in effective-mass theory (EMT). Direct optical transitions between $1s$ and three non-degenerate $2p$ states have been observed in silicon at 10.2, 11.4 and 12.0 meV (Lipari and Altarelli, 1976).

FE travel with a crystal momentum $\hbar\mathbf{k}_i$ (see Figure 2.5). In principle FE recombination must be accomplished by creation or annihilation of a phonon with momenta $\hbar\mathbf{k}_i$ or $-\hbar\mathbf{k}_i$ respectively.[2] At low temperatures and in very pure crystals (trap free), FE luminescence can however be observed when multi-phonon coupling occurs (Dean *et al.*, 1967). In Figure 2.5 a calculation of the phonon dispersion relations for silicon is shown, where one can see that single-phonon assisted luminescence must be compensated by $\hbar\omega_{TO} = 58.0$ meV, $\hbar\omega_{LO} = 56.2$ meV, or $\hbar\omega_{TA} = 18.4$ meV at $\mathbf{k}_i$, producing a series of phonon side-bands on the low energy side of a very weak ZP-line.

2.2.4 Bound-exciton luminescence

Given the wide separation in $\mathbf{k}$-space between the conduction band bottom and the valence band top, FE recombination probability is low in pure Si crystals. The FE life-time is strongly dependent on defect concentration. It goes from as long as 60 μs in the purest floating-zone crystals, to 2 μs when the boron concentration is only $\sim 10^{12}$ cm^{-3}. Impurities and defects can act as traps, confining the electron-hole pair on its neighbourhood with a binding energy E_{bx}. E_{bx} is a defect dependent quantity, representing the necessary energy to free the exciton. An exciton bound to a defect is referred as a bound exciton (BE) in contrast with the highly mobile FE. A BE can also be thought of an excited state of the defective crystal. Here, the defect is "partially" ionised, simultaneously binding an electron and a hole, much like a long lived transition state between the neutral and the ionised defects. Calculations on bound-excitons has been successful by using effective-mass theory (see Subsection 2.5.2) Stoneham and Harker (1975).

Returning to the configurational diagram (Figure 2.4), the excited state now represents a BE trapped by a defect with a vibrational coordinate Q. The ground state is attained after BE-recombination. In the excited state, either electron and hole can be more or less tightly bound to the defect. For example, the C-line in Si, believed to arise from the interstitial carbon-oxygen complex, has been shown to have an excited state made up

---

[2]Zero-phonon recombination has been reported due to small deviations from the cubic environment (Dean *et al.*, 1967).

from a strongly bound hole and a weakly bound electron (Thonke *et al.*, 1985). In fact, Kleverman *et al.* (1988) had shown that this excited state is responsible by a series of effective-mass-like photoluminescence excitation lines due to an electron weakly bound to a positive "pseudo"-ion.

2.2.5 Experimental aspects

Photoluminescence experiments can be performed using above or below band-gap excitation. Using below band-gap photoexcitation, light is not absorbed by the crystal, but centres can be directly excited, and by tuning the photon energy one can measure the response of the centre in frequency. This is called photoluminescence excitation spectroscopy (Davies, 1999). More commonly, above band-gap sources are used. Here, Ar^+ (2.41 eV) or Kr^+ (1.84 eV) gas state lasers are then employed. The penetration depth of these sources is of few μm, which has drastic experimental implications. In indirect band-gap semiconductors like silicon, FE's can travel through the crystal, and store energy in defects by being captured. We then expect radiative decay to mirror somewhat the chemical and structural environment of the excited centre.

Isotopic effects can be detected in phonon sidebands As $\omega \propto 1/\sqrt{\mu}$, the change of the reduced mass μ of an oscillator leads to a shift in the side-bands separation. However, in a particular local vibrational mode not all atoms necessarily contribute to μ, and symmetry considerations must be taken into account. Nevertheless, it is possible to extract useful information about the chemical nature of a defect when a shift of a phonon sideband series is observed after isotopic substitution. For example, in a vibrational mode strongly localised around an oxygen atom, the isotopes ^{16}O and ^{18}O will be responsible for the appearance of two phonon replicas, where the frequency of the heavier mode will be approximately $\sqrt{16/18} = 0.943$ of its lighter counterpart.

Isotopic effects are not an exclusive feature of phonon sidebands. Normally, as the electronic wavefunctions for excited and ground states are different, one should expect a different zero-phonon frequency for each of them, i.e., $\hbar\omega_g \neq \hbar\omega_e$, and therefore, any change

in the reduced mass of the mode that couples both states should produce a shift in the ZP-line.

2.3 Deep level transient spectroscopy

In contrast to substitutional dopants that produce shallow states near the band edges, other impurity complexes are associated with deep and localised states. This is the case of various radiation-induced defects such as the vacancy (Watkins, 1992), divacancy (Watkins and Corbett, 1965; Coomer *et al.*, 1999*b*), or the vacancy-oxygen complex (Watkins and Corbett, 1961*a*; Kimerling, 1976). In this section, another spectroscopic technique, namely deep level transient spectroscopy (DLTS), first introduced by Lang (1974*a*), is described. Excellent review articles can be found in the literature (Miller *et al.*, 1977; Palmer, 1990; Mooney, 1999), and therefore a brief overview is given here.

2.3.1 Deep states in semiconductors

Defects having deep states in the band gap are characterised by ionisation or affinity energies of about or greater than $E_g/10$, implying a deep potential valley that makes the electron or hole wavefunction strongly localised around the defect. In thermal equilibrium, the charge state of a particular defect is governed by the steady state ejection and capture processes, which depend on doping, temperature and sample compensation. As a consequence, the chemical potential of electrons or holes for which a defect changes its charge state, will define a level within the band gap. Defects are normally classified as traps, generation or recombination centres, depending on the relative capture processes. If (e_n, e_p) are the electron and hole emission rates, and (c_n, c_p) their respective capture rates, we can classify deep level defects according to Figure 2.6. In that figure, a) shows an electron trap, where electron capture and ejection rates are favoured, and governing its charge state. An analogous situation is the one in b), but here, the defect behaves as a hole trap. Generation centres are those where electron and hole emission rates dominate the occupancy dynamics, and recombination centres are those that have large capture rates,
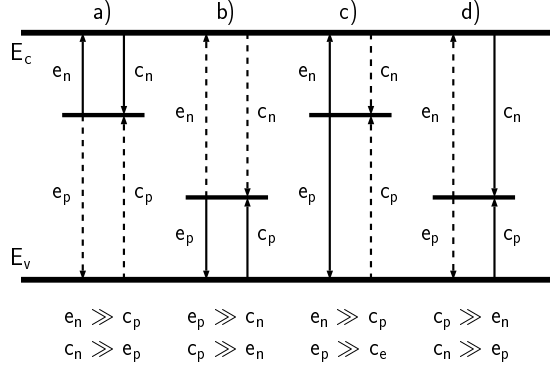
Figure 2.6: Scheme of traps, generation and recombination centres. E_c and E_v are the conduction and valence band edges respectively. e_x and c_x are the carrier ejection and capture rates, where x can be n or p for electrons and holes respectively.

so favouring the annihilation of electron-hole pairs [see c) and d) respectively]. Capture rates are given by

$$c_n = \sigma_n \langle v_n \rangle n \tag{2.32}$$

$$c_p = \sigma_p \langle v_p \rangle p, \tag{2.33}$$

where σ_n and σ_p are the electron and hole capture cross sections, and n and p are the free electron and hole concentration, respectively. The average electron or hole velocities $\langle v_n \rangle$ and $\langle v_p \rangle$ correspond to thermal averages, and assuming free carrier gases, these are given by

$$\langle v_n \rangle = \sqrt{\frac{3k_B T}{m_e^*}} \quad \text{and} \quad \langle v_p \rangle = \sqrt{\frac{3k_B T}{m_h^*}}, \tag{2.34}$$

where k_B is the Boltzmann constant and m_e^* and m_h^* are the electron and hole effective masses at their respective band edges.

At non-zero temperatures, thermal emission occurs. If $\Delta E_n = E_c - E_T$ and $\Delta E_p = E_T - E_v$ are depths of electron and hole traps measured from the conduction and valence

band extrema respectively, e_n or e_p will be proportional to a Boltzmann factor involving these energy differences. Hence ΔE_n and ΔE_p are free energies of ionisation. Following the principle of detailed balance, the emission and capture rates must match in thermal equilibrium, allowing us to write

$$e_n = \frac{\sigma_n \langle v_n \rangle N_c}{g} \exp\left(\Delta S_n / k_B\right) \exp\left(\Delta H_n / k_B T\right) \tag{2.35}$$

$$e_p = \sigma_p \langle v_p \rangle N_v \, g \exp\left(\Delta S_p / k_B\right) \exp\left(\Delta H_p / k_B T\right). \tag{2.36}$$

Here, we split each free energy into the entropy S and enthalpy H for the electron and hole trapping processes respectively. N_c and N_v are the densities of states for the conduction and valence bands respectively, and g the degeneracy of the trap. Note that $N_{c \atop v} \propto T^{3/2}$ and the average velocities $\langle v_{n \atop p} \rangle \propto T^{1/2}$, and therefore $\langle v_{n \atop p} \rangle N_{c \atop v} \propto T^2$ which must be taken into account when plotting the Arrhenius relations given by 2.35 and 2.36.

2.3.2 Measurements of the transient capacitance

In a semiconductor p-n junction or a Schottky diode, a carrier-depleted space charge region is formed as a consequence of an electric dipole across the junction. The width of this space charge layer can be controlled by applying an external potential difference, and therefore, we can think of this device as a variable capacitor. For p^+-n or n-type Schottky diodes, the width of the space-charge is given by the well known expression,

$$W = \sqrt{\frac{2\epsilon\left(V_0 + V\right)}{e N_D}} \tag{2.37}$$

where ϵ is the permitivity of the material, V_0 and V the built-in and external potentials, e is the electron charge, and N_D the density of ionised donor dopants in the lightly doped side of the junction. The device capacitance is readily obtained as

$$C = \frac{\epsilon A}{W} = \sqrt{\frac{e\epsilon N_D}{2(V_0 + V)}} \tag{2.38}$$
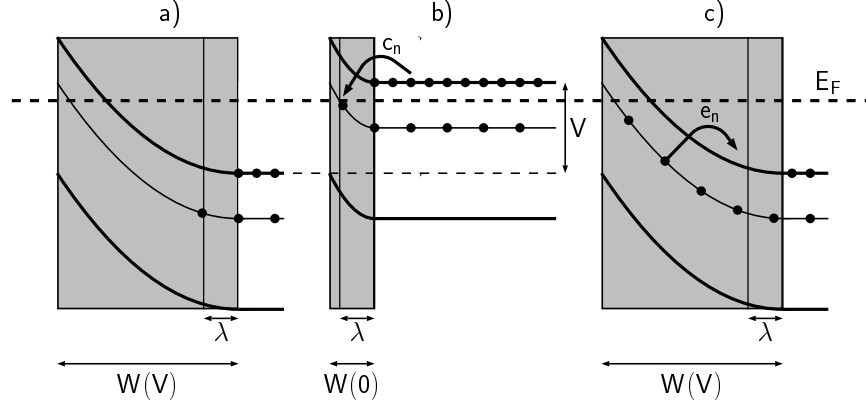
Figure 2.7: Band-structure diagram for the n-type side of a p$^+$-n junction or Schottky diode, under a majority-carrier pulse. Steps shown are a) before the pulse under reverse-bias, b) during pulse with zero voltage, and c) after pulse under reverse-bias applied voltage V.

where A is the junction area. The very important feature of these junctions is that after an electron or hole is emitted to the respective band edge, it is promptly expelled out of the depletion region in a time scale of 10^{-12} to 10^{-10} s, and therefore avoids being re-trapped by the impurity or other defects Mooney (1999).

As an example, lets consider Figure 2.7. Here we show the variation of the depletion region during a majority-carrier pulse. In the same figure we also show the band bending and a deep electron trap in the top half of the band gap. Outside the space-charge region the Fermi level is locked around the dopant level. Let us assume that the input signal is V (reverse bias) when $t < t_i$ and $t > t_f$, and zero when $t_i < t < t_f$. Starting in a), with a steady state reverse bias V, one can notice that all the carriers are depleted from a region of width W given by equation 2.37. However, in the right-most side of the depletion region there is a low concentration of free carriers that can be captured by electron traps. This is called the transition region and its width λ depends on the Fermi and trap levels E_F and E_T, i.e.,

$$\lambda = \sqrt{2\epsilon \frac{E_F - E_T}{e^2 \left(N_D - N_T\right)}}, \tag{2.39}$$

where normally $N_D - N_T \approx N_D$. In the transition region the electron capture rate is higher than the ejection rate, and therefore the charged defect has a long life time here. After $t = t_i$ [see b)], a zero-bias pulse is applied to the junction for sufficient time that all traps are filled; then after the pulse (at $t > t_f$), there is a transient regime that is due to thermally-induced emission of electrons from the traps [see c)] at a rate e_n such that the space-charge region is recovered.

During the filling process, the density of filled traps $n_T(t)$ is given by

$$n_T(t) = N_T \left(1 - e^{-c_n t}\right) \tag{2.40}$$

whereas during the transient emptying process,

$$n_T(t) = N_T e^{-e_n t}. \tag{2.41}$$

Assuming $N_D \gg N_T$, the capacitance of the junction per unit area can be written as

$$C(t) = C_0 \left[1 - \frac{N_T}{2 N_D} \exp(-e_n t)\right], \tag{2.42}$$

where C_0 is the quiescent capacitance given by Equation 2.38. The relative temporal capacitance change $(\Delta C / C_0)$, which is the sensitivity of the junction to trapped charges, is then

$$\frac{\Delta C}{C_0} = -\frac{N_T}{2 N_D} \exp(-e_n t). \tag{2.43}$$

Note that the sign of the capacitance change is negative when emission majority carriers takes place and positive for minority carriers. This feature makes it easy to know which type of carriers are being emitted.

In a DLTS experiment, periodic filling pulses are applied to a reverse biased junction, where the $C(t)$ transients having different temperature-dependent time constants $\tau = 1/e_n$ are
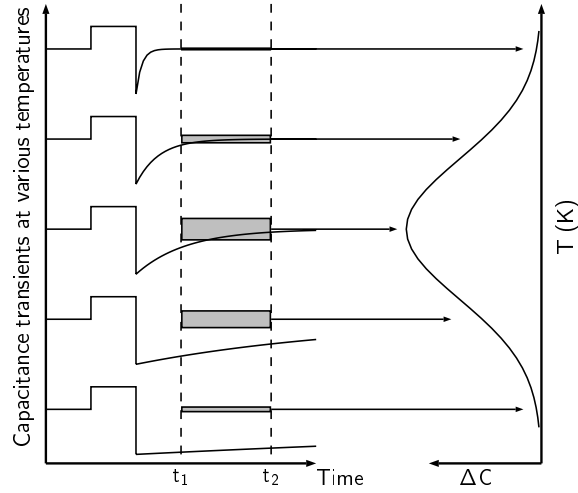
Figure 2.8: Implementation of a DLTS rate window by means of a boxcar differentiator with gates set at times t_1 and t_2

studied. In Figure 2.8 the box-car method (Lang, 1974a,b), is depicted. Here, a DLTS signal defined as $C(t_2) - C(t_1)$ is measured, and this signal has a maximum value at the temperature for which

$$\max(e_n) = \frac{1}{t_2 - t_1} \ln\left(\frac{t_2}{t_1}\right). \tag{2.44}$$

By changing t_1 and t_2, we alter the temperature T for which $\max(e_n)$ occurs. Several pairs (T, e_n) for the peak of the DLTS signal are extracted, plotted as $\ln(e_n/T^2)$ versus $1/T$, and finally, by fitting the pre-exponential factor and power arguments in Equations 2.35 and 2.36, we obtain ΔH and the capture cross section of the defect.

2.3.3 DLTS signal of the VO complex in Si

The vacancy-oxygen complex in silicon (or A-centre), is probably one of the best examples of an electron trap. Among other observations, the thermal behaviour of the DLTS and EPR signals were soon correlated. The defect was shown to be stable in the neutral and negative charge states, with an acceptor state 0.17 eV deep below the conduction band (Kimerling, 1976; Meese $et~al.$, 1983).
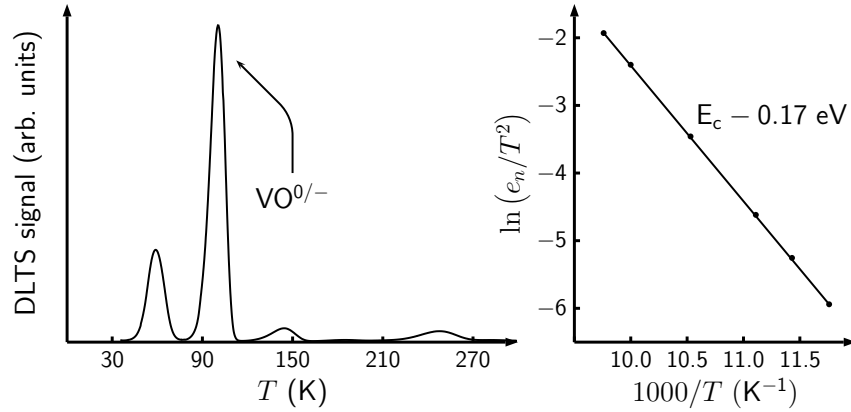
Figure 2.9: DLTS spectrum from a Cz-Si sample which has been irradiated with fast electrons at room temperature (on the left). The main defect produced after this treatment is the vacancy-oxygen complex (VO), which has a deep acceptor state 0.17 eV below the conduction band (on the right). Experimental data kindly provided by L. Rubaldo.

On the left side of Figure 2.9, a typical DLTS spectrum of silicon irradiated with fast-electrons (2 MeV) at room temperature, is shown. Among all features, the labelled peak around 100 K corresponds to the A-centre signature. Its thermal analysis allows us to obtain a thermal enthalpy $\Delta H = 0.17$ eV for emission of the trapped electron into the conduction band. It must be noticed here that the temperature at which the emission rate is measured is much less than that to anneal out the VO defect ($\sim$300-350°C). Obviously this is not always the case, where deeper traps with low thermal stability may not be measurable by DLTS.

2.4 Infra-red vibrational spectroscopy

The presence of defects in a crystalline host destroys at least the translational symmetry of the lattice, modifying the storage of vibrational energy in two main ways: By perturbing the vibrational density of states, where any new mode strongly overlaps existing host modes, or by introducing modes such their frequencies lie in spectral regions which are forbidden in the perfect crystal. In the first case the mode is called resonant, whereas in
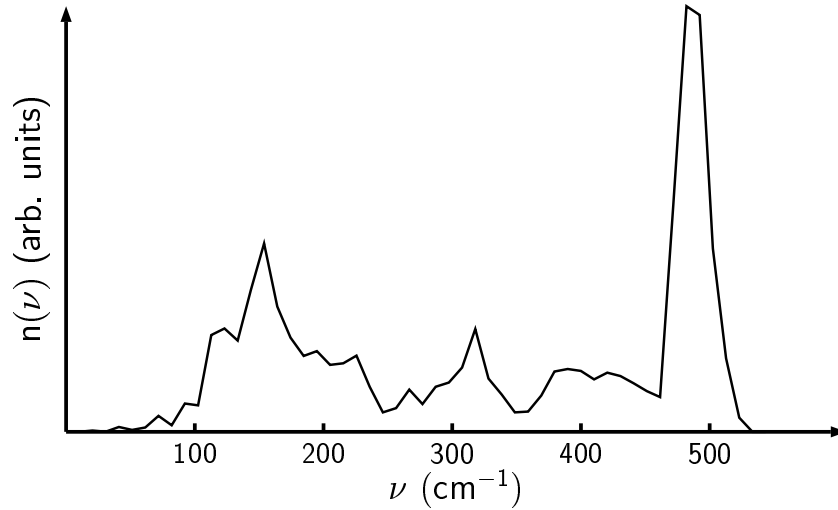
Figure 2.10: Calculated phonon density of states in silicon, using the extended Keating potential (Sangster *et al.*, 1992).

the second the mode is said to be localised, and its coupling with the lattice phonons is weak. Localised modes are normally divided into two classes, i.e., the local modes which appear above the maximum frequency allowed by the perfect crystal, and the gap modes which appear within gap regions. One can see from Figure 2.10 that we can not have gap modes in Si, as phonons with energies $0 \leq \nu \leq \nu_R$ are allowed, with a maximum $\nu_R = 523$ cm^{-1} called Raman frequency for Si.

Absorption of IR radiation by one-phonon excitation processes in group-IV semiconductors is forbidden. The presence of the inversion element in the space group implies a vanishing coupling between the optical modes at Γ and the electric field. However, multi-phonon processes are possible, providing that the total momentum created is zero and the selection rules are satisfied. In fact, particularly strong absorption occurs around $\sim$600 cm^{-1} and $\sim$1000 cm^{-1} in Si, which unfortunately is the region of many impurity related absorption features, including the thermal double donors.

In this section, the interpretation of vibrational IR absorption measurements is given. This includes the IR band strength and line width, mass and charge state effects. More detailed sources and further information can be found in works by Newman (1973); Stavola (1999)

and McCluskey (2000).

2.4.1 Local modes and integrated absorption

Not all local modes are IR-active. The electric dipole moment $\boldsymbol{\mu}$ induced by a group of atoms oscillating about their equilibrium positions with a normal mode Q, can be expanded in a power series of Q, i.e.,

$$\boldsymbol{\mu} = \boldsymbol{\mu}_0 + \left(\frac{d\boldsymbol{\mu}}{dQ}\right)_0 Q + \left(\frac{d^2\boldsymbol{\mu}}{dQ^2}\right)_0 Q^2 + \cdots , \tag{2.45}$$

where $\boldsymbol{\mu}_0$ is the static electric dipole, and the derivatives are to be taken at the equilibrium configuration. For small vibration amplitudes, we can assume that $\boldsymbol{\mu}$ is linear with Q. The transition probability between any initial and final states i and j respectively is proportional to $|\langle i \, |\hat{\mathbf{e}} \cdot \boldsymbol{\mu}| \, j\rangle|^2$, where $\hat{\mathbf{e}}$ is the polarisation direction of the external electric field. Clearly, only odd terms from equation 2.45 will contribute to a non-zero transition probability. Higher order terms only contribute for a transition probability to higher harmonic states.

The integrated absorption (IA) of an IR band is proportional to the concentration of illuminated defects. Dawber and Elliot (1963) derived the commonly used expression for the IA of a non-degenerate mode with effective mass m as

$$\text{IA} = \int \alpha(\nu)\, d\nu = \frac{\pi\, \eta^2\, N}{m\, n\, c^2}, \tag{2.46}$$

where α is the absorption coefficient, n is the refractive index of the crystal, N the concentration of absorbing centres, and c the velocity of light. The quantity $\eta = |d\boldsymbol{\mu}/dQ|$ has units of electric charge, and is normally referred to as the effective charge of the mode Q. Note that η is not related to the charge of the defect. In fact, neutral defects with values of $\eta = 2$ or even higher have been reported (Newman, 1973). The absorption coefficient α has units of cm^{-1}, and is the actual quantity that is measured during the experiments. This is done by relating the intensity of the incident light to that of the escaping beam. In

the absence of internal interference (due to multiple reflections), the transmitted intensity I_t is related to the incident intensity I_0 by

$$I_t = \frac{(1-R)^2 \, e^{-\alpha \, d}}{1 - R^2 \, e^{-2\alpha \, d}}, \qquad (2.47)$$

where the d is the sample thickness, and the reflection coefficient R is given by

$$R = \frac{(n-1)^2 + \kappa^2}{(n+1)^2 + \kappa^2}, \qquad (2.48)$$

where n and κ are the refractive index and the extinction coefficient respectively.

Equation 2.46 is of fundamental interest for spectroscopists since it allows the direct determination of the defect concentration once a calibration factor is known.

2.4.2 Temperature effects and band-shape

In general, the band frequency and its width depend on several factors. Among them is the thermal expansion of the lattice, which can perturb the local geometry of the defect, anharmonic coupling with other vibrations including host modes, or the life-time of excited states. Considering the dependence on the temperature due to thermal expansion, we start by defining a second rank tensor A that gives us the band shift due to an applied stress given by another second rank tensor $\boldsymbol{\sigma}$,

$$\Delta\omega = \mathsf{A} \cdot \boldsymbol{\sigma}, \qquad (2.49)$$

Here, A is normally referred as a piezospectroscopic tensor, and can be measured by a variety of spectroscopic techniques (Kaplianskii, 1964). Assuming thermal expansion as a negative hydrostatic pressure, one can express $\boldsymbol{\sigma}$ with help of the crystal elastic constants c_{11} and c_{12}, and the fractional change in the lattice parameter $\Delta a_0(T)/a_0(0)$, i.e.,

$$\sigma_{ij} = (c_{11} + 2c_{12})\frac{\Delta a_0(T)}{a_0(0)} \, \delta_{ij}, \qquad (2.50)$$

84

where $\Delta a_0(T) = a_0(T) - a_0(0)$, and $a_0(T)$ is the crystal lattice parameter at any temperature T. Any quantitative estimate of $\Delta \omega$ can by obtained by relating $\Delta a_0(T)/a_0(0)$ with the thermal expansion coefficient $\alpha(T)$ for the appropriate material.

Most commonly, low temperature (LT) absorption bands in Si are enhanced by $\sim 3 - 8$ cm^{-1} when compared with those measured at room temperature (RT). Obviously, $\Delta \omega$ is strongly dependent on the crystal-defect coupling, and in particular situations, anomalous shifts can in fact be observed. One example is the interstitial oxygen dimer in Si, where the room-temperature frequencies were found to lie ~ 0.3 cm^{-1} above those measured at $T = 10$ K (Murin *et al.*, 1998; Öberg *et al.*, 1998).

Line broadening is normally explained as due to the finite life-time of the promoted state. When anharmonic coupling with other modes takes place, an additional contribution which is dependent on the occupancy of the partner mode, and therefore strongly T-dependent, must also be considered. This is true in the case of 1136 cm^{-1} dominant band of the interstitial oxygen, where the coupling of an asymmetric mode stretch mode with a low-energy doubly-degenerate bend-mode makes the band shape vary dramatically with temperature (Bosomworth *et al.*, 1970). As recently proposed by Budde *et al.* (2001), a similar picture seems to be applied for the bond-centred hydrogen atom in Si.

2.4.3   Isotope and charge effects

Identification of the chemical composition of defects in semiconductors is a primary goal in spectroscopy. IR vibrational spectroscopy, can provide this information from band shifts that occur when samples containing different isotopes are investigated. It is known from a *ball and spring* that model, a diatomic molecule vibrates with a frequency $\omega \propto \sqrt{1/\mu}$, where μ is the reduced mass of the atomic pair. A similar analysis can be applied to an infinite chain of atoms of mass M with the appropriate periodic boundary conditions (Kittel, 1986; Stavola, 1999; McCluskey, 2000). Here we get a Raman frequency of

$$\omega_R = \sqrt{\frac{4f}{M}}, \tag{2.51}$$

where f is some intrinsic force constant associated with the spring that binds each atom to its neighbours. Substitution of one chain-atom by another with mass m (keeping the same force constants), can lead to two distinct situations. If $m \geq M$, the density of vibrational states will be perturbed by the presence of an impurity mode below ω_R, i.e., a resonant mode. However, if $m < M$, this perturbation appears above ω_R as a local vibrational mode (LVM) with some frequency ω_L. This last situation is of particular interest here, since these LVMs can be accurately predicted with *ab-initio* calculations. Resonant modes are normally calculated by perturbative methods (Montroll and Potts, 1955; Maradudin, 1966), and will not be discussed here.

The empirical diatomic model has been applied quantitatively to estimate isotopic shifts of impurities in crystals (Newman, 1973). Here, the LVM frequency is given by

$$\omega_L = \sqrt{f\left(\frac{1}{\alpha M} + \frac{1}{m}\right)} \tag{2.52}$$

where $1 \leq \alpha \leq 4$ is a parameter that takes into account the coupling of the impurity with the host atoms. For example, the interstitial oxygen in silicon sits in the bond centre site, where ^{16}O and ^{18}O isotope versions produce absorption bands at 1136 and 1084 cm^{-1} at liquid He temperatures respectively. The ratio $^{16}\omega/^{18}\omega = 1.048$ can be compared with its estimated value by using equation 2.52, where $^{16}\omega/^{18}\omega = 1.046$ is obtained by using $\alpha = 2$ to account for two Si neighbours.

Although this approach works well with simple substitutional and interstitial impurities, it gives rather poor results for the absolute band frequencies. One certainly loses any faith on this model when treating complex defects where chemical bonding properties can be accurately described only with more sophisticated methods.

Another important phenomenon which can produce a shift in a LVM is associated with charge state effects. When a particular defect is electrically active, the capture or emission of carriers can change dramatically the local environment. The bonding properties (which can be interpreted as the spring force constants), are then perturbed, and the vibrational mode frequency will differ from that of the uncharged defect. The vacancy-oxygen complex

in Si is perhaps an obvious example, where the absorption band associated to the anti-symmetric mode of the Si-O-Si unit is shifted by $\sim$50 cm^{-1} when comparing the negative charge state with the neutral defect.

2.4.4   IR absorption of the VO defect

The vacancy-oxygen complex (or substitutional oxygen) in silicon is the main product after annealing irradiated Cz-Si. It is a well studied defect by LVM-spectroscopy (Corbett *et al.*, 1961; Bean and Newman, 1971; Lindström *et al.*, 1999*a*). As the O atom bridges two second neighbouring Si atoms (see Figure 2.3), the longer Si-O-Si unit when compared with that in O$_i$, is responsible for a lower anti-symmetric stretch mode frequency at 835 cm^{-1}, compared with 1136 cm^{-1} for O$_i$. Since the VO defect can be in two different charge states, we concentrate first on the neutral. The 835 cm^{-1}-band can be seen in lower spectrum on Figure 2.11 under the $V^{16}O^{(0)}$ label. In the upper spectrum, at 799 cm^{-1}, we have the same mode observed in a sample doped with ^{18}O isotopes. This observation demonstrates unequivocally the presence of at least one O atom in the defect. In samples with both ^{18}O and ^{16}O isotopes only the 835 and 799 cm^{-1}-bands are observed, where the absence of mixed modes strongly supports the presence of only one O-atom in the defect.

As it was shown in Subsection 2.3.3, the VO defect possesses an acceptor level at $E_c -$ 0.17 eV. Therefore, in thermodynamic equilibrium, the negative charge state will be populated according to the position of the Fermi level. Although the spectra in Figure 2.11 were recorded from high resistivity samples, the constant presence of the excitation source pumps electrons to the conduction band, which are then trapped by VO defects. Therefore VO$^{(0)}$ and VO$^{(-)}$ are detected simultaneously. From the same figure we can notice dramatic increase in the frequencies (by $\sim$50 cm^{-1}) for the negative defects compared with their neutral counterparts. The ^{18}O rich sample had a high concentration of carbon, leading to the presence of a band at 865 cm^{-1} which belongs to an interstitial carbon-oxygen complex.

LVM calculations on the VO defect was previously done by Ewels *et al.* (1995) and Pesola *et al.* (1999*a*), who assigned an anti-symmetric stretch mode localised on the Si-O-Si
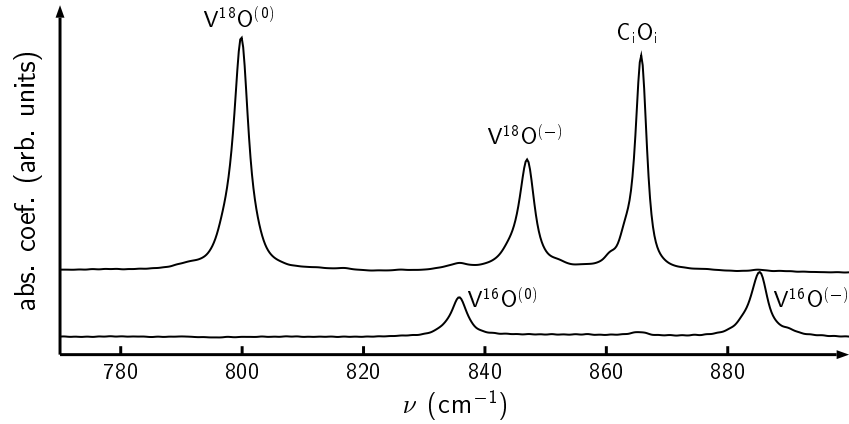
Figure 2.11: Infra-red absorption of the VO defect in Cz-silicon at 10 K. Upper spectrum was measured in a C-rich sample enriched with ^{18}O. Lower spectrum is from a C-lean with naturally abundant oxygen. Experimental data kindly provided by J. Hermansson.

unit to the 835 cm^{-1}-band. Also recently, a frequency enhancement mechanism for the negative defect was proposed (Coutinho *et al.*, 2000*b*). It is suggested that after filling an anti-bonding state with the trapped electron, a Coulombic repulsion between the high electron density region between the two Si-dangling bonds and the O-atom, flattens the Si-O-Si unit, strengthening the Si-O bonds.

2.5 Electronic IR-Absorption

2.5.1 Introduction

Substitution of a host Si atom by a singly-ionised group-V species, leaves all neighbouring Si atoms saturated, and the band-gap free of deep states. However, the excess of positive charge at the substitutional defect creates an attractive potential. In fact this potential is asymptotically Coulombic and slowly varying. This property is particularly useful as any electron moving in this potential spends most of its time in this far region. The properties of the extra electron (needed to neutralise the system), are then analogous to those in the hydrogen problem. However, as the potential is strongly screened by the medium, the

binding energy of this electron is of the order of 50 meV in Si. That is why these defects are normally called shallow donors or acceptors, or shallow dopants when deliberately introduced. Energy levels of excited states are commonly observed in the form of a Lyman series ($1s \rightarrow 2p$, $1s \rightarrow 3p$, ...), or even the Balmer series ($2s \rightarrow 3p$, $2p \rightarrow 3s$, ...). All these observations are very well described by effective-mass theory (EMT), early developed by Kohn (1955, 1957), and reviewed by Stoneham (1975); Ramdas and Rodriguez (1981).

On the other hand, some group-VI atoms (S, Se and Te), as well the thermal double donors, are known to produce a He-like series of excited states, behaving as double donors (Glodeneau, 1967; Ning and Sah, 1971; Grimmeiss and Janzén, 1992). Although substitutional chalcogen atoms create deep states in the gap (about 0.2-0.3 eV for the first ionisation energy), their infrared absorption spectra can still be interpreted within the EMT, and the comparison with the TDD defects is of considerable interest.

2.5.2 Effective-mass theory

The electronic band structure of Si has an indirect gap. This is shown on the top half of Figure 2.5, where the conduction band minima at $\mathbf{k}_i$ is about $0.8 \times 2\pi/a_0$ away from the valence band top. There are six equivalent minima along $\langle 100 \rangle$ directions with effective mass of $m_t = 0.19\,m_e$ and $m_l = 0.92\,m_e$, where m_e is the free-electron mass.

Let us imagine that a singly ionised group-V or doubly ionised group-VI atom replaces a host atom from a group-IV crystal with an isotropic conduction band minimum, and effective mass m_e. All four valence electrons may be assumed to form sp^3 hybrid orbitals with four neighbours. The excess of positive charge Z at the impurity then generates a screened Coulomb potential

$$V_i = -\frac{Z}{\epsilon r}, \tag{2.53}$$

within the crystal with permitivity ϵ. This equation is not valid in the neighbourhood of the impurity (often referred as central-cell region), but it is a good approximation for

$r \gg a_0$. If an electron is brought back into the crystal, it will move with effective-mass m_e in the hydrogen-like potential V_i, and similarly to the hydrogen atom, a series of bound states at E_b below the conduction band will appear, where

$$E_b = \frac{Z^2 m_e}{2\epsilon^2 n^2} \tag{2.54}$$

In Equation 2.54, $n = 1, 2, \ldots$. For a singly ionised group-VI impurity in the ground state, partial screening occurs and we may assume $Z \approx 1$ when considering to bring back another electron.

In a more rigorous way to treat the problem in Si, we must assume all six equivalent conduction band minima, and an *hydrogenic* wavefunction is expanded in terms of Bloch functions $\psi_{n\mathbf{k}}$, but assuming that only conduction-band states ($n = 0$) contribute appreciably to the wavefunction, i.e.,

$$\Psi(\mathbf{r}) = \sum_{j=1}^{6} \alpha_j F_j(\mathbf{r}) \psi_{0\mathbf{k}_j}(\mathbf{r}). \tag{2.55}$$

Here the index j runs over the six conduction-band minima, the coefficients α_j are evaluated numerically (disregarding redundancy arising from time-reversal and defect symmetry). F_j is known as hydrogen-like envelope function belonging to the j-th minimum, and solution of the the following hydrogenic Hamiltonian,

$$\left[-\frac{\hbar^2}{2m_t} \left(\frac{\partial^2}{\partial x^2} + \frac{\partial^2}{\partial y^2} \right) - \frac{\hbar^2}{2m_l} \frac{\partial^2}{\partial z^2} + V_i(\mathbf{r}) \right] F_j(\mathbf{r}) = E_b F_j(\mathbf{r}). \tag{2.56}$$

In Equation 2.56 the anisotropy of the conduction band minima is taken into account, hence splitting the p states into p_0 and $p_\pm$. This makes every s, p_0 and $p_\pm$ states six-, six- and twelve-fold degenerate for an impurity with T_d symmetry. However, due to inter-valley coupling, this symmetry is lifted as a maximum of three-fold degeneracy is possible in Si. Fully symmetric s and p_0 states unfold into $A_1 + E + T_2$, and $p_\pm$ states into $2T_1 + 2T_2$ (Ramdas and Rodriguez, 1981). This splitting is shown schematically in Figure 2.12 for a

Conduction band

$2p_\pm$ ——— $2p_\pm$ $(2T_1 + 2T_2)$

$2p_0$ ——— $2p_0$ $(A_1 + E + T_2)$

$1s$ ——— $1s$ (E)

$1s$ (T_2)

$1s$ (A_1)

Effective-mass theory   Observations
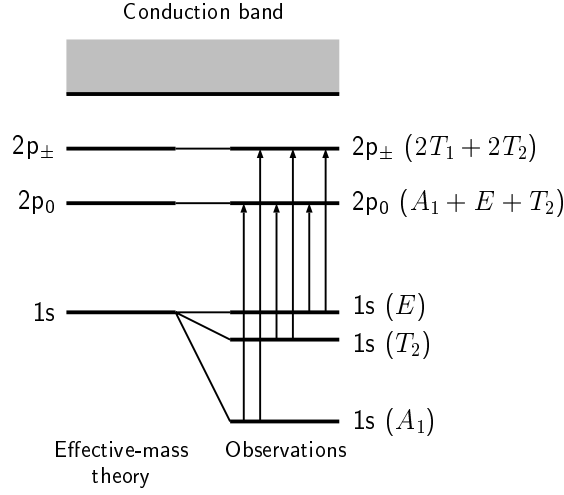
Figure 2.12: Energy level scheme of a substitutional donor in Si. Irreducible representations from a T_d point group are also shown.

substitutional donor, where the coefficients α_i for an s state can be deduced by inspection (Tinkham, 1964) as

$$
\begin{aligned}
\alpha_i^{A_1} &= \tfrac{1}{\sqrt{6}}\,(1,\ 1,\ 1,\ 1,\ 1,\ 1) \\
\alpha_i^{E'} &= \tfrac{1}{\sqrt{12}}\,(-1,\ -1,\ -1,\ -1,\ 2,\ 2) \\
\alpha_i^{E''} &= \tfrac{1}{2}\,(1,\ 1,\ -1,\ -1,\ 0,\ 0) \\
\alpha_i^{T_2'} &= \tfrac{1}{\sqrt{2}}\,(-1,\ 1,\ 0,\ 0,\ 0,\ 0) \\
\alpha_i^{T_2''} &= \tfrac{1}{\sqrt{2}}\,(0,\ 0,\ -1,\ 1,\ 0,\ 0) \\
\alpha_i^{T_2'''} &= \tfrac{1}{\sqrt{2}}\,(0,\ 0,\ 0,\ 0,\ -1,\ 1).
\end{aligned}
\tag{2.57}
$$

We note that the wavefunction of the fully symmetric A_1 s-state possesses the maximum amplitude at the origin, making it the ground state for attractive centres. Its binding energy is therefore strongly dependent on the chemical nature of the defect. This is the case of common dopants like substitutional phosphorus or arsenic, according to early EPR experiments by Fletcher *et al.* (1954*a,b*) and Feher (1959*a,b*). However, as group theory is unable by itself to establish the ordering of the split-up, other arrangements are possible. This is the case of interstitial Li in Si, where the ground state was attribute to a five-

fold degenerate $1s(E + T_2)$ state, 1.8 meV below the $1s(A_1)$ state (Watkins and Ham, 1970). The isotropic hyperfine interaction on ^{7}Li was found to be less than 0.1 MHz. This corresponds to a minute spin localisation. Especially when comparing with the 3 MHz measured for the ^{17}O hyperfine on the VO defect, despite the fact the the O atom sits at a node of the paramagnetic wavefunction. This situation is of particular interest here, as the TDD defects in Si were shown to possess a 1s(T2) ground state, where only two conduction band minima contribute to $\Psi(\mathbf{r})$ (Stavola et al., 1985). The 12-fold degenerate p-states, in principle, also split. However, as the amplitude of the wavefunction is very small nearby the defect, the split-up is often negligible.

2.5.3   Absorption of double donors

It is expected that the substitutional group-VI impurities like S, Se and Te should behave as double donors. DLTS experiments reported emission barriers of 0.587 and 0.302 eV to ionise S^+ and S^0 defects (Grimmeiss et al., 1980). These values were confirmed by IR-absorption, where ground state binding energies of 613.5 and 318.3 meV were found for S^+ and S^0 respectively (Grimmeiss et al., 1982; Jazén et al., 1984). The strong deviation of these values from the EMT binding energies of a He-like donor double donor D [125.08 and 31.27 meV for D^+ and D^0 respectively (Faulkner, 1969)], was reproduced after including a central-cell correction and multi-valley scattering effects in the Hamiltonian (Pantelides and Sah, 1974). This term, affects then the energy separation between s-states. As the $1s(E)$ states have zero amplitude at $r = 0$, their binding energies are expected to be close to the values predicted by EMT. In fact, both $1s(E)$ and $1s(T_2)$ states in S^0 were measured to lie 31.6 and 34.62 meV below the conduction band respectively (Jazén et al., 1984, 1985). These are to be compared with EMT $1s(A_1 + E + T_2)$ degenerate states at $E_c - 31.27$ meV (Faulkner, 1969). For the same reason, good agreement between theory and experiment is also observed for the binding energy of p-states.

In general, further splittings of s- and p-states can occur. This is the case for defects with lower symmetry than T_d such as the thermal donors. As these have C_{2v} symmetry, s-states will split into singlets. The same occurs for p-states. In fact, a small splitting of the $p_\pm$-

states was measured for these defects, somewhat mirroring their anisotropy (Wagner and Hage, 1989).

2.6 Summary

Several experimental techniques which are commonly used to probe the properties of defects have been described. These consist of not only spectroscopic methods, where a precise quantum of energy is emitted or absorbed by the system, but also of thermodynamic methods like DLTS, where a transient signal between two equilibrium states is monitored.

A great deal of information can be obtained, especially if one is able to correlate different techniques. EPR gives us the anisotropy and symmetry of a gap state, providing that partial occupancy takes place. Combined with LCAO analysis, many details of a defect and its surroundings might be accessible. Optical measurements like IR absorption or PL are among the most popular type of experiments. Local mode frequencies and isotopic shifts are vital regarding the chemical constituents, dynamics and bonding arrangement of a defect. Absorption due to electronic transitions in shallow defects also take part within the IR spectral region. Here, the interpretation of the experiments on the basis of effective-mass theory has proven very effective. Again, this allows us to *draw* a considerably detailed picture of the electronic structure associated with the defect.

Despite the fact that only a description of the basic physics underlying each method has been given here, a comprehensive understanding of the properties of a defect normally involve a cooperation between several techniques, and very often the introduction of some sort of external field which will perturb the Hamiltonian. This is the case of uniaxial stress, electric or magnetic fields. These perturbations must then be explained on the basis of a theoretical model. Other variants involve the creation of anisotropy such as stress-induced alignment, which in partnership with polarised excitations sources, allow experimentalists to monitor the resulting dichroism in the output signal, and eventually its recovery kinetics.

Chapter 3

Oxygen, Vacancies and Hydrogen

3.1 Introduction

The vacancy-oxygen (VO or A-centre), is one of the most common defects produced by
room-temperature electron irradiation of Si or Ge containing oxygen (Watkins and Cor-
bett, 1961a,b; Whan, 1965). It is believed to form through trapping of mobile vacancies by
interstitial oxygen atoms. The accepted structure is shown in Figure 3.1(a) and involves a
weak Si-Si reconstructed bond between the Si atoms labelled 3 and 4. In Si, the defect has
an acceptor level at $E_{\rm c} - 0.17$ eV (Watkins and Corbett, 1961a), while the corresponding
defect in Ge has an acceptor level located at $E_{\rm c} - 0.25$ eV (Fukuoka et $al.$, 1983). The
acceptor level of the defect in Si has been calculated previously by the cluster method to
be $E_{\rm c} - 0.13$ eV (Resende et $al.$, 1999).

In Si, VO^0 and VO^- are known to possess IR-active LVMs with B_1 symmetry at 835 cm^{-1}
and 885 cm^{-1} respectively (Watkins and Corbett, 1961b; Bean and Newman, 1971). How-
ever, in Ge only one band at 620 cm^{-1} has been attributed to the defect (Whan, 1965),
probably in the neutral state.

Previous theoretical work has successfully investigated the defect in Si, although the up-
ward shift in the LVM for VO^- was not explained (Ewels et $al.$, 1995; Pesola et $al.$, 1999a).
Recent experimental work has assigned a combination band $A_1 + B_1$ around 1400 cm^{-1},

94
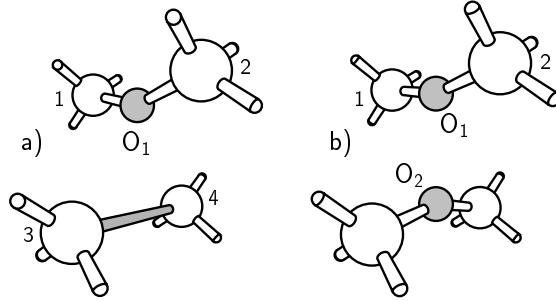
Figure 3.1: The VO (left), and VO$_2$ (right) centres. In a), the dark bond represents a reconstructed bond between Si or Ge atoms 3 and 4.

where A_1 is a symmetric stretching mode at $\sim$540 cm^{-1} (Murin *et al.*, 1999; Lindström *et al.*, 1999*b*).

3.1.1 Structure and energetics

Table 3.1 gives structural details of the neutral VO^0 and charged VO$^-$ defects in both Si and Ge as found in cells with 64 atoms. The O atom in both charge states moves away from the T-site and bridges two second neighbour host atoms. The length of the reconstructed bond increases from 3.26 Å in the neutral defect to 3.42 Å in the negatively charged centre. This small change leads, as we shall show below, to a dramatic change in the piezospectroscopic tensor and local vibrational modes.

Table 4.2 gives the formation energies of the interstitial and neutral substitutional oxygen centres. It is clear that the formation energy of VO exceeds O$_i$ by more than 2 eV, and thus the substitutional defect is only expected to be found at high temperatures or in the presence of a non-equilibrium concentration of vacancies produced for example by irradiation. Nevertheless, there is a strong binding between a vacancy and interstitial oxygen. The reaction energies are given in Table 3.2. Here a positive value indicates that the reaction is exothermic. This table shows there is a binding energy of about 1.6 eV between V and O$_i$. The formation energies for the vacancies in Si and Ge used in Table 3.2 were evaluated in 64 atom cells to be 3.61 and 2.20 eV respectively, in good agreement

95

Table 3.1: Bond lengths (Å) and angles (degrees) for VO and VO_2 centres in Fig. 3.1. X is Si or Ge and V denotes the centre of the vacancy

	Si			Ge		
	$VO^{(0)}$	$VO^{(-)}$	VO_2	$VO^{(0)}$	$VO^{(-)}$	VO_2
O_1–X_1	1.70	1.68	1.67	1.79	1.79	1.77
X_1–X_2	3.26	3.27	3.28	3.45	3.46	3.48
X_3–X_4	3.32	3.42	3.28	3.36	3.36	3.48
X_1–O–X_2	150	154	158	150	152	158
O–V	1.05	1.08	1.23	1.13	1.14	1.31

with recent plane-wave calculations (Puska *et al.*, 1998; Fazzio *et al.*, 2000).

3.1.2 Vibrational modes

The VO complex in Si has two fundamental local modes, whose combination frequency is estimated from a simple sum of the two fundamental A_1 and B_1 modes (see Table 3.3). The calculated values agree with the experiments within $10 \, \text{cm}^{-1}$ for Si and about $20 \, \text{cm}^{-1}$ for Ge. In Si, all three modes are strongly dependent on the charge state of the complex and increase in frequency for the negative charge state. In Ge only one localised mode is found.

In the negative charge state, the O atom is displaced away from the reconstructed bond consistent with the idea that the additional electron is trapped in this bond and repels the negatively polarised O atom. This movement leads to a compression of the bonds around O implying an enhancement in the LVM as shown in Table 3.3. It should be noted that within the LDA approximation, Ge is predicted to be a semimetal – the conduction band minimum at L has the same energy of the valance band maximum at Γ. This implies that the acceptor wavefunction in VO^- is delocalised and consequently the calculated shift in the B_1 mode probably underestimates the true shift (Coutinho *et al.*, 2000*b*).

Table 3.2: Reaction energies (eV) of vacancy-oxygen-hydrogen defects in Si and Ge. Negative values indicate endothermic behaviour.

			Silicon		Germanium
Reactants	$\longrightarrow$	Products	Calc.[a]	Calc.[b]	Calc.[a]
$V + O_i$	$\longrightarrow$	VO	1.57	1.4[c], 0.8[d]	0.36
O_i	$\longrightarrow$	$VO + Si$	-2.04		-1.86
$V + O_{2i}$	$\longrightarrow$	VO_2	2.76	2.6[c], 1.6[d]	1.04
O_{2i}	$\longrightarrow$	$VO_2 + Si$	-0.85		-1.18
$O_i + VO$	$\longrightarrow$	VO_2	1.73	1.8[c], 1.0[d]	1.30
$VO + O_{2i}$	$\longrightarrow$	$VO_2 + O_i$	1.19	1.2[c], 0.8[d]	0.68
$VO + H_{BC}$	$\longrightarrow$	VOH	2.02		
$VO + H_2$	$\longrightarrow$	$VOH + H_{BC}$	-0.09		
$VO + H_2$	$\longrightarrow$	VOH_2	2.41		
$VO + 2H_{BC}$	$\longrightarrow$	VOH_2	1.19		
$VOH + H_{BC}$	$\longrightarrow$	VOH_2	2.51		
$VOH + H_2$	$\longrightarrow$	$VOH_2 + H_{BC}$	0.40		

[a]This work.

[b]Pesola *et al.* (1999*a*)

[c]Using MP-2[3] for BZ sampling

[d]Using Γ-point for BZ sampling

Table 3.3: LVMs and their downward isotopic shifts (cm^{-1}) for VO and VO_2 complexes in Si and Ge. These are compared with experimental infra-red data.

	Mode	^{16}O Obs.	^{16}O Calc.	^{18}O Obs.	^{18}O Calc.	^{16}O, ^{18}O Obs.	^{16}O, ^{18}O Calc.
	$A_1 + B_1$	1370.0	1387	37.5	38		
Si:VO^0	B_1	835.8	839	35.9	37		
	A_1	$\sim$534	548	$\sim$1	1		
	$A_1 + B_1$	1430.1	1404	39.1	39		
Si:VO$^-$	B_1	885.2	872	38.2	38		
	A_1	$\sim$545	532	$\sim$1	1		
	E	894	893	39	41	0, 39	0, 41
Si:VO$_2$	A_1		593		6		3
	B_2		557		0		0
Ge:VO^0	B_1	620	642	31	33		
Ge:VO$^-$	B_1		643		33		
Ge:VO$_2$	E		690		36		0, 36
	A_1		363		13		6

3.1.3 Reorientation of VO

Two other configurations for the VO complex were investigated. Firstly, when the O atom is situated at the substitutional T-site, and secondly when it lies along one of the [111] directions with C_{3v} symmetry. In the neutral charge state, these configurations are less stable than the C_{2v}-form being 0.51 (0.10) eV and 0.26 (0.05) eV higher in Si (Ge) respectively (Coutinho *et al.*, 2000*b*). In the negative charge state these energies increase by factors of about 2 in Si and 4 in Ge. These results give an estimate of the activation barrier for the reorientation of the stable C_{2v} defect when its alignment changes from one [100] axis into another. Electron paramagnetic (EPR) studies in Si reveal that the reorientation barrier of the neutral defect is activated with an energy of 0.38 eV in good agreement with the calculated value of 0.26 eV (Watkins and Corbett, 1961*a,b*). Our calculations predict that in the negative charge state the reorientation barrier will be higher. This is in support of measurements on the recovery of the stress-induced dichroism of the 885 cm^{-1} vibrational band, where a value between 0.4 and 0.5 eV was estimated (Pajot *et al.*, 1994). Stress-DLTS experiments by Andersen (2001) also came up with an activation energy of $\sim$0.5 eV. However, here the barrier enhancement is interpreted as the the sum of two processes. The first involves electron emission with a 0.17 eV high barrier. This is then followed by atomic reorientation mediated by a 0.38 eV barrier.

3.1.4 Stress-energy tensor

The calculated values of the stress tensor for the VO defect in Si also depends on the charge state (Coutinho *et al.*, 2000*b*). For the neutral defect, we find the three principal values and directions to be: $B_1 = -9.79$ eV (along [100]: the C_2 axis); $B_2 = 5.49$ eV (along [011]) and $B_3 = 4.48$ eV (along [01$\bar{1}$]). The [011] and [01$\bar{1}$] directions are parallel to the Si-O-Si and reconstructed Si-Si bonds respectively. The experimental values for B_1, B_2 and B_3 are -11.1, 6.1 and 4.9 eV respectively (Watkins and Corbett, 1961*a*).

For the negative charge state, B_1, B_2 and B_3 are found to be -6.83, 7.81 and -0.55 eV compared with experimental values of -8.4, 8.8 and -0.4 eV respectively (Watkins and

Corbett, 1961a). The change of sign of B_3 indicates that the defect is now compressive along the *reconstructed* bond. This arises as the additional electron occupies an anti-bonding orbital and pushes the surrounding lattice outwards. However, this argument ignores the differences in the volumes of the neutral and charged defects. In fact we found that the neutral defect led to a decrease in the volume of the supercell compared with bulk Si whereas the charged defect led to a slight increase.

3.2 The VO$_2$ defect

3.2.1 Introduction

The A-centre in Si is known to anneal out around 300°C with a simultaneous appearance of a strong IR-band at 894 cm^{-1}. This band was originally assigned to the VO$_2$ centre (Corbett *et al.*, 1964b), formed when an interstitial oxygen atom traps a mobile VO-centre. However, there are some difficulties with this assignment. The concentration of O$_i$ appears to remain constant during the formation of the 894 cm^{-1}-band, stress splitting measurements indicate a defect with low symmetry (Bosomworth *et al.*, 1970) and, in addition, the two O atoms must be dynamically decoupled as additional modes are not detected in isotopically mixed samples (el Fotouh and Newman, 1974; Svensson and Lindström, 1986). Previous modeling however supports the assignment to VO$_2$ with D_{2d} symmetry (Deleo *et al.*, 1985; Ewels *et al.*, 1995; Pesola *et al.*, 1999a). There the O atoms were found to be dynamically decoupled and the calculated modes were in fair agreement with the data. In addition, when the defect anneals out three high frequency O-related LVMs are observed which are consistent with the formation of VO$_3$ (Ewels *et al.*, 1995). Moreover, recent stress alignment experiments find the symmetry of the centre to be D_{2d} consistent with a VO$_2$ defect (Nielsen, 1996).

3.2.2 Defect structure

Our results support previous theoretical work in finding the ground state structure to possess D_{2d} symmetry. Here both oxygen atoms occupy equivalent positions by bridging atoms neighbouring the vacancy as shown in Figure 3.1(b). Structural details are given in Table 3.1, where it is noted that the Si-O bond lengths are shorter than in VO and there is a larger displacement of both oxygen atoms from the centre of the vacancy.

Table 4.2 shows that the formation energy of the defect in Si (Ge) is 0.85 eV (1.18 eV) higher that that of the staggered dimer. Thus arguments based on simple volumetric considerations implying that the aggregation of pairs of oxygen atoms lead to the creation of Si (Ge) interstitials are unlikely to be correct. The binding energy of O_i with a pre-existing VO defect is 1.73 eV.

3.2.3 Local vibrational modes

The LVMs of the defect are given in Table 3.3. These are in excellent agreement with the observed 894 cm^{-1}-band and the O atoms, without any O-O bond, are found to be decoupled without any additional modes appearing in the mixed isotopic case. Thus the model correctly describes the observations (el Fotouh and Newman, 1974).

The VO$_2$ centre in Ge has similar properties to the Si centre but has not yet been detected. The vibrational modes, given in Table 3.3, also consist of independent modes at 690 cm^{-1} and 363 cm^{-1}.

3.2.4 Stress-energy tensor

The stress tensor is axial with $B_3 = -11.81$ eV and the principal direction is along the C_2 axis joining the two O atoms and $B_1 = B_2 = 5.9$ eV. It has however not yet been measured. The axial value of the B-tensor mirrors a considerably stronger compressive strain when compared with the VO defect. This stronger anisotropy must arise from the mutual Coulombic repulsion between the O atoms.

Figure 3.2: Defect structures for VOH_2 in Si. Silicon, oxugen and hydrogen atoms are shown as light gray, white and dark gray spheres.

3.3 Hydrogenation of the VO defect

3.3.1 Introduction

It is known that hydrogen complexes with single vacancies by saturating the Si or Ge dangling bonds leading to VH_n defects where n runs from 1 to 4 (Nielsen *et al.*, 1995, 1997; Estreicher, 1995; Coomer *et al.*, 1999*a*). In addition, recent work has demonstrated that hydrogen is easily trapped by the A-centre in Si forming VOH_n defects where n is 1 or 2. The latter, shown in Figure 3.2, produces infrared absorption bands at 2151, 2126 and 943 cm^{-1}, which were assigned to the symmetric and asymmetric stretch modes of Si-H, and the asymmetric stretch mode of the oxygen atom respectively (Markevich *et al.*, 2000). However no indication of the presence of the partially passivated A-centre (VOH) was found in this work. IR bands related to VOH_2 were clearly shown to be correlated with a precipitated disapearance of the A-centre at 150°C. These observations were also supported by cluster calculations (Markevich *et al.*, 2000). Here we report similar calculations done with the supercell code.

The VOH centre was suggested to account for the E3 DLTS acceptor level at $E_c - 0.31$ eV formed in proton-implanted Fz-Si crystals (Svensson *et al.*, 1989). EPR experiments identify the centre which persists until 290°C in proton-implanted Cz-Si (Johannesen *et al.*, 2000). The hyperfine interaction with the proton located 2.5 Å from the Si atom with a dangling bond was resolved. The defect has C_{1h} symmetry below 180 K, but above 240 K the centre possesses C_{2v} symmetry arising from a thermally activated hopping of

the H atom between dangling bonds (Johannesen *et al.*, 2000; Nielsen *et al.*, 1999). The activation energy for the hopping of H and D atoms was found to be 0.18 and 0.26 eV respectively for the neutral defect. The same C_{2v} symmetry was found from a recent stress Laplace DLTS study on the E3 centre (Nielsen *et al.*, 1999). This is because the electron emission rate measured in DLTS occurred at a temperature where the H atom was able to hop between Si dangling bonds.

No vibrational modes of the defect have been reported to date. Previously, the defect had been investigated theoretically using a Hartree-Fock cluster method (Artacho and Ynduráin, 1989).

3.3.2 Defect structure

Relaxation of the neutral VOH defect with C_{1h} symmetry gave the Si-H and Si-O lengths to be 1.50 and 1.68 Å. The distance between the H atoms and the Si atoms with a dangling bond is 2.7 Å in good agreement with the experimental estimate of 2.5 Å. The ground state structure is shown in Figure 3.3(a). A trigonal form of the defect was also investigated (see Figure 3.3(b)), but this defect is unstable by 0.5 eV in favour of the C_{1h} structure.

Two configurations of the VOH_2 defect were investigated. In the first, both hydrogen atoms were placed inside the vacancy (see Figure 3.2(a)) in a manner similar with VH_2 (Nielsen *et al.*, 1995). In the second configuration, they lay outside, at anti-bonding sites, as in NiH_2 (Jones *et al.*, 1995). Both configurations have C_{2v} symmetry. We found that the second configuration was 1.25 eV higher in energy than the first where the hydrogen atoms lie inside the vacancy.

For the relaxed configuration, the Si-O bond lengths were 1.65 Å compared with 1.70 Å in the A-centre. Clearly, the saturation of the Si dangling bonds has increased the strength of the Si-O bonds. The calculations indicate that the energy released when the hydrogen molecule interacts with the the A-centre to form VOH_2, is 2.4 eV. This strongly supports the view that A-centres are effective traps for mobile H_2 molecules.
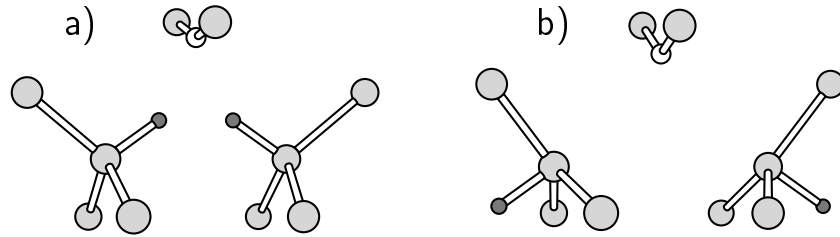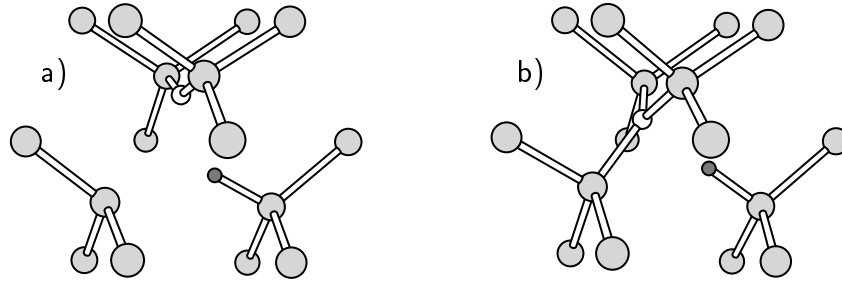
Figure 3.3: Defect structures for VOH in Si. Silicon, oxygen and hydrogen atoms are shown as light gray, white and dark gray spheres. Structures in a) and b) have C_{1h} and C_{3v} symmetry.

3.3.3 Local vibrational modes

The vibrational activity of VOH arises from almost decoupled oscillations of Si-O-Si and Si-H units. The 854 cm^{-1}-mode is due to asymmetric stretch of Si-O-Si while hydrogen related stretch and bend modes are found at 2042, 578 and 532 cm^{-1} respectively. These are recognized as such from the displacements of these atoms in the modes. Mixed isotopic data show these modes are almost decoupled. The 565 cm^{-1}-mode is a breathing mode showing a small shift for both ^{18}O and D substitution. The Si-D wag modes fall within the lattice modes, and thus, no isotopic shifts are available in Table 3.4. In the negative charge state, the 854 cm^{-1}-mode increases to 901 cm^{-1}. This mirrors the changes in the local mode of VO when it traps an electron.

The local vibrational modes for VOH$_2$ along with their isotope shifts are given in Table 3.5. The calculated and observed frequencies and their isotopic shifts are in reasonable agreement (Markevich *et al.*, 2000). The two highest frequencies, at 2248 and 2219 cm^{-1}, are the symmetric and anti-symmetric Si-H stretching modes respectively. The 907 cm^{-1}frequencies correspond to the anti-symmetric stretching mode of the Si-O-Si unit, $\sim$50 cm^{-1}above the analogous mode in VOH.

The calculated isotopic shifts (Table 3.5) show that the oxygen and hydrogen-related LVMs are completely decoupled: in either case, oxygen or hydrogen isotopic substitution

Table 3.4: LVMs of VOH in Si and their downward isotopic shifts (cm^{-1}) for ^{18}O and D substitution. R labels indicate resonant modes.

	^{16}O, H	^{18}O, H	^{16}O, D	^{18}O, D
	2042.4	0.0	575.3	575.4
	854.4	37.6	0.0	37.6
VOH^0	578.5	0.0	R	R
	565.2	1.5	5.9	7.8
	532.5	0.4	R	R
	2045.7	0.0	576.0	576.0
	901.2	40.2	0.0	40.0
VOH^-	594.3	0.0	R	R
	571.8	0.3	5.5	6.9
	554.1	1.6	R	R

Table 3.5: Calculated and measured LVM frequencies for VOH$_2$ in silicon. All frequencies and isotopic shifts (IS) are in cm^{-1}.

	Obs.[a]	IS	Calc.[a]	IS	Symm.
	2151.5		2248		A_1
V^{16}OH$_2$	2126.4		2219		B_1
	943.5		907		B_2
	1567.4	584.1	1605	643	A_1
V^{16}OD$_2$	1549.1	577.3	1594	625	B_1
	943.2	0.3	907	0	B_2
	2140.6	10.9	2224	24	A'
V^{16}OHD	1557.3	569.1	1609	610	A'
	$\sim$943.5	~ 0	907	0	A''
			2248	0	A_1
V^{18}OH$_2$			2219	0	B_1
			868	39	B_2

[a]Markevich *et al.* (2000)

does not affect the LVMs. For example, the 907 cm^{-1} O-related mode is unaffected by deuteration in agreement with observations.

The two highest H-related LVMs are also almost independent. The highest LVM is an A_1 mode and lies 29 cm^{-1} above the anti-symmetric B_1 mode, in very good agreement with the observed splitting of about 25 cm^{-1}. The observed splitting is similar to the one found (22.5 cm^{-1}) for the VH$_2$ centre (Nielsen *et al.*, 1995).

The calculated oxygen-related mode at 907 cm^{-1} is about 40 cm^{-1} below the observed frequency, but it is much higher than that calculated for the A-centre at 839 cm^{-1}(Coutinho

et al., 2000*b*). This increase in frequency demonstrates that the saturation of the Si recon- structed bond leads to stronger Si-O-Si bonds and mirrors what is seen experimentally: namely the neutral A-centre has a mode at 835 cm^{-1} while the O-related mode in VOH_2 lies at 943.5 cm^{-1}.

3.3.4 Energy levels

The VOH_2 defect has the vacancy fully saturated. In fact, no electrical activity was found for this centre. However, VOH has a Si dangling bond, and an acceptor level has been claimed for this defect. We also investigated the possibility for the existence of a donor state, or even a double donor level. In the doubly positive charge state, the defect was also considered as shown in Figure 3.3(b), with the oxygen and H atoms lying in the same $\langle 111 \rangle$ direction. Here the oxygen is three-fold coordinated, and as in OH_3 molecule, easy to ionize.

The chosen standard defects (see Subsection 1.8.2) are the VO defect (for the accetor level), and substitutional sulphur (for donor and double donor levels). These defects have levels at $E(-/0) = E_c - 0.17$ eV (Watkins and Corbett, 1961*a*), $E(0/+) = E_c - 0.30$ eV and $E(+/++) = E_c - 0.59$ eV (Grimmeiss *et al.*, 1980).

The calculations indicate that the VOH defect has single acceptor and donor levels at $E(-/0) = E_c - 0.32$ and $E(+/0) = E_v + 0.42$ eV. No second donor state was found. The acceptor level is very near the experimental value at $E(-/0) = E_c - 0.31$ eV (Svensson *et al.*, 1989). Recently, (Feklisova *et al.*, 2001) assigned a hole trap (H4) at $E(+/0) = E_v + 0.28$ eV to VOH, and therefore we suport those conclusions.

It is worthy to note that using for example carbon-interstitial as standard (with well known acceptor and donor levels at $E(-/0) = E_c - 0.10$ and $E(+/0) = E_v + 0.28$ eV respectively (Song *et al.*, 1990)), one gets acceptor and donor levels at $E(-/0) = E_c - 0.40$ and $E(+/0) = E_v + 0.21$ eV respectively for VOH — also in good agreement with the experiments.

The VOH defect is paramagnetic in the neutral charge state. A large ^{29}Si hyperfine

splitting associated with a unique silicon site was identified in EPR experiments. The hyperfine tensor is almost axial and the unique principal axis deviates only 3.9° from the $\langle 111 \rangle$ direction. This is a characteristic of a Si dangling bond. This dangling bond was found to accout for 60% of the spin-density, of which 89% is of p-character. The hyperfine on H is nearly vanishing. Its isotropic component is 4.7 MHz, and thus much smaller than the 1420 MHz for atomic hydrogen (Johannesen *et al.*, 2000).

The Mulliken bond population for the highest occupied band was averaged using the MP-2^3 sampling scheme. Here we found no localization either on O or H atoms. The state is mostly localized on the Si atom. We estimated 53% of localization on this dangling bond, 86% of which is p-like. These values are in very good agreement with the EPR observations, and provide extra support for its assignement.

3.3.5   Hydrogen hopping

The activation energy for H hopping between the Si dangling bonds in the VOH defect can be estimated by relaxing the defect with C_{2v} symmetry. This gave a barrier, E_a, of 0.11 eV for the neutral defect but this neglects the zero-point energy of the H atom. If we assume that the contribution of this vanishes at the saddle point, where the Si-H bonds are very long at 1.80 Å, then the barrier will include the contribution of $-\hbar\omega/2$ where ω is the frequency of the Si-H stretch mode given in Table 3.4. The inclusion of this term effectively eliminates the barrier and implies that tunneling must become important. It is known that the barrier is apparently greater in the D case by about 0.07 eV Johannesen *et al.* (2000). For the negatively charged centre, the barrier increases to 0.18 eV.

In addition to the hopping of H, the O atom can also jump between different $\langle 100 \rangle$ axes. An upper limit to this barrier can be found by constraining both O and H to lie on the same $\langle 111 \rangle$ axis (see Fig. 3.3(b)). This configuration is found to be 0.42 and 0.72 eV above the ground-state for the neutral and negatively charged defects respectively. These values are greater than found for the A-centre consistent with the view that both H and a trapped electron impede the hopping of the O atom.

3.4 Summary

These studies reveal a number of previously unknown features. The VO and VO_2 defects are examined and it is found that charging the former defect leads to an increase in frequency as observed, while the latter is responsible for the 894 cm^{-1} band in Si. Confirmation that the 894 cm^{-1} band is due to VO_2 could come from an evaluation of the stress tensor which is given here.

The piezospectroscopic stress-energy tensor for VO has been evaluated for the first time. It demonstrates that the reconstructed bond in VO breaks when an electron occupies the anti-bonding state and the atoms with broken bonds move away from each other compressing the lattice. This type of calculation can be extended to many defects and links directly total energy calculations with spectroscopic data obtained from stressed crystals in which defects have been aligned.

The VOH defect is remarkable in that the H and O atoms can break their bonds leading to reorientation of the defect with activation barriers of a few tenths of an eV. The barriers are larger for the negatively charged defects. Calculated occupancy levels at $E(-/0) = E_c - 0.32$ eV and $E(+/0) = E_v + 0.42$ eV are in very good agreement with the measurements.

The calculated LVMs for VOH_2 and their isotopic shifts reproduce well the experimental values, and therefore support experimental findings that the H_2 molecule can interact with the A-centre.

Chapter 4

Early oxygen aggregates

4.1 Introduction

Oxygen is the most common and best studied impurity in Cz-Si (Shimura, 1994; Jones, 1996; Newman, 2000). Nevertheless, in spite of work extending over 50 years, many of its properties remain poorly understood. Even the structure of the isolated interstitial impurity — long believed to be a simple bent Si-O-Si unit similar to the arrangement in quartz — has come under recent debate. Detailed analysis of its far infra-red local vibrational modes (LVMs) has suggested that the energy barrier between the bent form with an Si-O-Si angle of around 160°, and the highly symmetrical configuration where the O atom lies at the bond centre (BC) is negligible.

Another dramatic suggestion is that the aggregation of two O atoms leading to an oxygen dimer does not lead to the ejection of a Si interstitial forming a VO_2 centre, but is a defect with the remarkable property of migrating through the lattice at a rate faster than that of the single interstitial. This result has led to a reappraisal of both the rates at which larger oxygen clusters form, and the oxygen composition of the thermal donor defects which arise after sustained annealing of Cz–Si below about 450°C (Fuller *et al.*, 1954).

All these issues have tremendous implications on the overall picture of the early states of oxygen clustering, in particular on the chemical composition of thermal donor defects. We

start with the simplest and best studied oxygen defect — the interstitial oxygen (O_i).

4.2 Interstitial oxygen defect

4.2.1 Introduction

Interstitial oxygen is known to lie near a bond centred site with equal Si-O bonds and the static defect can, in principle, assume either C_1, C_{1h}, C_2 or D_{3d} symmetry. The different symmetries depend on the position of O with respect to the back bonded Si atoms as shown in Figure 4.1(a) and (b). In D_{3d}, the O atom lies at the bond centre. The defect possess several LVM-bands which, at low temperatures ($T < 40$ K), lie around 30, 517, 1136 and 1750 cm cm^{-1}. Although these bands have been intensively investigated in the last 50 years, only those at 30 and 1136 cm^{-1} are clearly understood (Bosomworth *et al.*, 1970; Yamada-Kaneta *et al.*, 1990; Yamada-Kaneta, 1998)

The first arises from the motion of the O atom in a {111} plane normal to the Si-O-Si direction. These modes were analysed in terms of an empirical potential which led to the conclusion that the equilibrium Si-O-Si angle is 164° and that the energy barrier to the bond centre site is of the order of 10 meV (Bosomworth *et al.*, 1970). Further investigations have lowered the barrier to about 1 meV so that the O atom tunnels between equivalent sites leading to an effective D_{3d} symmetry (Yamada-Kaneta *et al.*, 1990). The 1136 cm^{-1} (A_{2u}) band arises from an asymmetric stretch of the two Si-O bonds, while the 517 cm^{-1}-band, lying near the Raman line of bulk Si, has been assigned either to a symmetric stretch mode (A_{1g}), or to an E_u mode with little amplitude on the O atom. The latter is required as the mode is insensitive to the oxygen mass.

The 1750 cm^{-1}-band has been attributed to a combination of the 1136 cm^{-1}-mode and an IR inactive band around 600 cm^{-1} (Yamada-Kaneta *et al.*, 1990). This has recently been supported by the discovery of a new oxygen-related band at 648.2 cm^{-1} assigned to a combination between a weak, or inactive mode, at ~618 cm^{-1} and the low energy band at 30 cm^{-1} (Hallberg *et al.*, 1998).

In the case of Ge, the situation is less clear. Here, interstitial oxygen produces three absorption bands at $\sim$1, 860, and 1260 cm^{-1} (Gienger *et al.*, 1993; Kaiser, 1962). These can be considered as analogues of the 30, 1136, and 1750 cm^{-1} bands in Si. Gienger *et al.* (1993) suggested that in Ge, the Ge-O-Ge angle is smaller than in Si and the low energy excitations are between different axial angular momentum states of a rigid buckled Ge–O–Ge rotator as shown in Figure 4.1(b). It is thus expected that the barrier for moving the O atom to the bond centre site is larger in Ge than Si.

Previous modelling studies in Si have determined both the structure of the defect and two high frequency O-related fundamentals (Snyder *et al.*, 1989; Jones *et al.*, 1992). These were located at 1104 and 554 cm^{-1} and assigned to the asymmetric and symmetric modes of the buckled Si-O-Si unit respectively. The modes related to E_u fell below the Raman and were hidden by the lattice modes.

Calculations carried out in Ge, gave a symmetric stretch mode around $\sim$400 cm^{-1} (Artacho *et al.*, 1982), but no band near the Raman edge was reported. Again, the 1260 cm^{-1}-band is assigned to a combination between the symmetric ($\sim$400 cm^{-1}) and anti-symmetric (860 cm^{-1}) modes.

4.2.2 Defect structure

Table 4.1 shows the relative energies and structure of the defect when confined to C_2, C_1, C_{1h}, and D_{3d} symmetry calculated in a 64 Si or Ge atom supercell (Coutinho *et al.*, 2000*b*). It is clear that in Si, there is very little energy difference between all the structures consistent with a tunnelling model.

In Ge, however, the bent Ge-O-Ge configuration, with an angle about 144°, is preferred with about 0.1 eV barrier to the D_{3d} structure. In these calculations the cell size was fixed using the calculated host lattice parameter a_0 equal to 5.39 Å in Si, and 5.58 Å in Ge. However, the high concentration of defects ($\sim$10^{21} cm^{-3}) may result in a substantial volume change and this was investigated by allowing the cell volume to relax. Figure 4.2(a) shows the variation in the total energy when the lattice parameter is varied. The energy

Table 4.1: Relative energies (in meV) and structural details of configurations for O_i in Si or Ge (denoted by X).

	Si				Ge			
	C_2	C_1	C_{1h}	D_{3d}	C_2	C_1	C_{1h}	D_{3d}
E_{rel}	0	9	1	13	0	12	3	106
X–O, Å	1.62	1.61	1.62	1.61	1.73	1.73	1.73	1.71
X–O–X, degrees	158	166	157	180	143	146	144	180
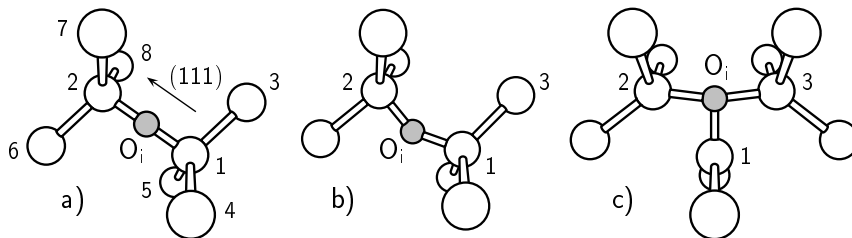
Figure 4.1: D_{3d} (a), C_{1h} (b) and Y-lid (c) configurations for interstitial oxygen.

difference between the C_2 and D_{3d} structures vanishes for lattice dilations larger than 0.5% but the C_2 structure is increasingly favoured under compression. The decrease in the energy of the cell when the lattice parameter is varied in this way is ∼30 meV in Si, while the bulk modulus is shifted downwards by ∼2% in Si and upwards by 0.5% in Ge. The effect of this concentration of oxygen is to increase the lattice parameter by 0.3% in both Si and Ge. Since the density of oxygen is 1/64 of that of Si, then this corresponds to a increased lattice parameter by $\epsilon\,[\text{O}]/[\text{Si}]$, where ϵ is found to be 0.19. This agrees precisely with X–ray data giving the same value of ϵ (Shaw, 1973; Imai *et al.*, 1987).

Table 1.3 gives the formation energy E_f of O_i in different sized cells. The calculated value lies between 1.66 and 1.81 eV in Si, somewhat larger than found by a plane wave method Pesola *et al.* (1999a). Assuming the solubility is given by $N_{\text{BC}} \exp(-E_f/kT)$ where N_{BC} is the density of bond centre sites, we obtain an equilibrium solubility between 6×10^{16} and 2×10^{17} cm^{-3} at 1300°C. This compares with a measured solubility of about 3×10^{18} cm^{-3}

Table 4.2: Formation energies (eV) for the single oxygen and di–oxygen centres in Si and Ge. *fccN, scN, bccN* and *ttrN* denote face-centred-cubic, simple-cubic, body-centred-cubic and tetragonal cells with N Si or Ge atoms. In the third column, n denotes the BZ sampling scheme utilised.

		MP-n^3	Cell	O_i	O_{2i}^{st}	O_{2i}^{sk}	O_{2i}^{dy}	VO	VO_2
	Si	1	*sc*216	1.66	2.88				
This work	Si	2	*sc*64	1.81	3.08	3.27	4.79	3.85	3.93
	Si	2	*ttr*96		3.04				
	Si	1	*fcc*128	1.1	2.0	2.1			
Pesola *et al.* (1999*a*)	Si	2	*sc*64					3.7	3.7
	Si	2	*bcc*32	1.8	3.0	3.4			
This work	Ge	2	*sc*64	1.19	1.76	2.31	3.61	3.05	2.94
	Ge	2	*ttr*96		1.73				

which corresponds to a formation energy of interstitial oxygen of around 1.4 eV Newman and Jones (1994). These estimates have ignored the vibrational entropic contributions.

The O atom with C_2 symmetry is displaced by 0.31 Å from the BC site in a $\langle 110 \rangle$ direction leading to an Si-O-Si angle of 158°. The Si-O length is 1.62 Å, slightly longer than that in the D_{3d} configuration. Table 4.1 shows that similar geometries are obtained in the C_1 and C_{1h} configurations.

4.2.3 Vibrational modes

The calculated LVMs for the C_2 and D_{3d} structures and their isotopic shifts are shown in tables 4.3 and 4.4 (Coutinho *et al.*, 2000*b*). These are compared with values obtained previously and the observed modes. The frequencies for the combination bands were obtained by summing the fundamental modes.
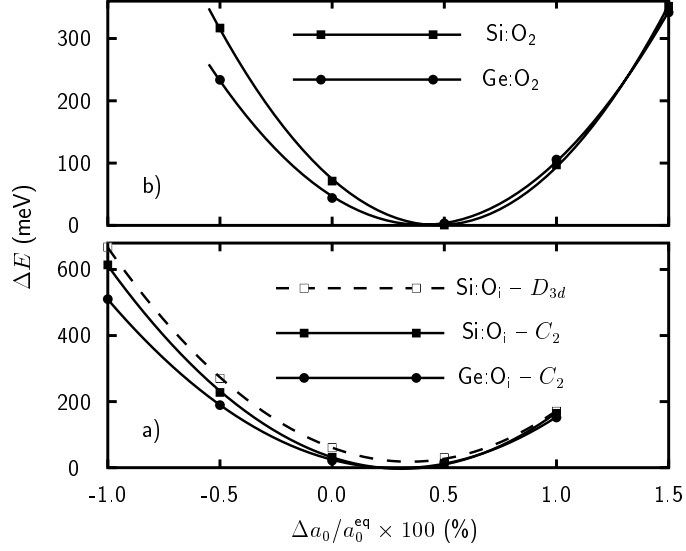
Figure 4.2: Relative Energies of a) interstitial oxygen in Si (squares) or Ge (circles), and b) staggered dimers in Si (squares) or Ge (circles) versus lattice parameter of 64 atom cell. a_0^{eq} refers to calculated Si and Ge bulk lattice constants of 5.39 Å and 5.58 Å respectively.

There are four fundamental modes for the C_2 defect. Asymmetric (B) and symmetric (A) stretch modes lie at 1108 and 621 cm^{-1} and a near degenerate pair of modes lie at 518 cm^{-1}. The latter are split by 0.2 cm^{-1}, and lie below the 526 cm^{-1} Raman frequency given by the Musgrave-Pople potential. They are recognized by their large amplitude on the two shells of Si neighbors to oxygen and arise from the compression of the back bonds by oxygen, but the oxygen atom does not participate in their motion. This follows from the insensitivity of these two lower modes to the oxygen mass (Table 4.3). However, a shift of 1 cm^{-1} occurs when one of the neighboring Si atoms is replaced by ^{30}Si. In D_{3d}, the two highest modes have A_{2u} and A_{1g} symmetry. The latter is infra-red inactive and implies that its analogue in C_2 at 621 cm^{-1} would be only weakly IR-active. The lower pair of modes have E_u symmetry. The vibrational modes associated with these frequencies are shown in Figure 4.3(a), (b) and (c).

The calculated LVMs for both C_2 and D_{3d} symmetries are similar to each other and in good agreement with the experimental data. This is especially true for the mode around

Table 4.3: Calculated LVMs, cm^{-1}, and their downward isotopic shifts for different configurations for O_i in Si. Results of previous calculations are given along with observed modes. Two-phonon modes are estimated by simple summation of asymmetric and symmetric fundamentals.

	Mode	^{28}Si ^{16}O ^{28}Si	^{30}Si ^{16}O ^{28}Si	^{28}Si ^{18}O ^{28}Si	^{30}Si ^{18}O ^{28}Si
	$A + B$	1729	14	53	66
Calc.[a]	B	1108	4	50	54
C_2	A	621	10	3	12
	A, B	518	2	0	2
	$A_{1g} + A_{2u}$	1803	14	54	68
Calc.[a]	A_{2u}	1184	4	55	58
D_{3d}	A_{1g}	619	10	0	10
	E_u	519	1	0	1
Calc.[b]	B	1098		50	
	A	630		2	
Calc.[c]	A	1104		53	
	B	554		1	
		1748.6	12.2	52.6	—
		1136.4	3.7	51.4	55.2
Observed[d]		$\sim$618	9.5	$\sim$0	—
		517.8	—	0.0	—

[a]This work.

[b]Pesola *et al.* (1999*a*)

[c]Jones *et al.* (1992)

[d]Pajot *et al.* (1995), except the 618 cm^{-1} band from Hallberg *et al.* (1998).
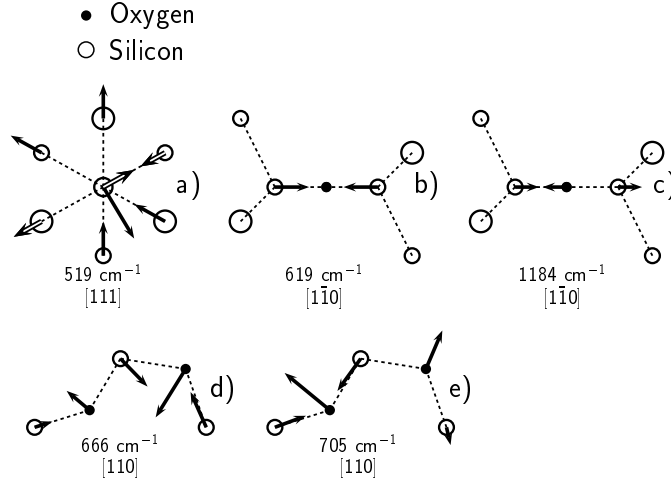
Figure 4.3: Normal coordinates of the vibrational modes for O_i in Si [a), b) and c)], and for the dimer modes at 666 and 705 cm^{-1} [d) and e)]. The two components of the E_u mode in a) are distinguished by filled and outlined arrows. The 666 cm^{-1} mode in d) has a small induced dipole moment arising from the movements of the oxygen atoms which are out of phase with each other. The normal to the projected plane is given in each case.

621 cm^{-1} which has been detected as a partner in two combination bands (Yamada-Kaneta *et al.*, 1990; Hallberg *et al.*, 1998). Thus, there is nothing in the observed or calculated modes which allows the symmetry of the defect to be unambiguously identified. As described above, the D_{3d} model has been singled out as it can explain the fine structure of the 30 cm^{-1}-band. However, this band is too low in frequency to be accurately modeled using *ab-initio* methods. Nevertheless, the effect of pressure on the high frequency modes allows us to discriminate between these models.

Figure 4.4 shows the LVMs as a function of pressure. This dependence can be expressed through either the isotropic piezospectroscopic tensor element A_1, given in Table 4.5, and appropriate for a trigonal defect, or through the Gruneisen parameter, $\gamma = -\partial \ln \omega / \partial \ln V$. We find that, for the D_{3d} structure, A_1 is positive for all LVMs — in agreement with experiment at low pressures (Hrostowski and Kaiser, 1957; Hallberg *et al.*, 1998; Kaiser, 1962; Artacho *et al.*, 1982). The large difference between the values of A_1 for the 1136 cm^{-1}-band found by uniaxial and hydrostatic stress experiments is in part due to the non-linear

Table 4.4: Calculated LVMs, cm^{-1}, and their downward isotopic shifts for O$_i$ in Ge. Results of previous calculations are given along with observed modes. Two-phonon modes are estimated by simple summation of asymmetric and symmetric fundamentals.

	Mode	^{70}Ge ^{16}O ^{70}Ge	^{74}Ge ^{16}O ^{74}Ge	^{70}Ge ^{18}O ^{70}Ge	^{74}Ge ^{18}O ^{74}Ge
	$A + B$	1248	8	55	63
Calc.[a]	B	847	2	44	46
C_2	A	401	6	11	17
	$A + B$	1293	8		
Calc.[b]	B	878	3		
	A	416	6		
		1274.0	8.3	—	—
Observed[c]		862.91	1.01	43.28	45.45
		412.1[d]	7.3[d]	—	—

[a]This work.

[b]Artacho et $al.$ (1982)

[c]Mayur et $al.$ (1994)

[d]This frequency was calculated by assuming the existence of a combination mode $A + B$ at 1274.0 cm^{-1}.

fit employed in the latter (McCluskey, 1999).

However, A_1 is negative for the C_2 structure as the buckling increases with pressure and leads to slightly dilated Si-O bonds. Experimentally, the asymmetric stretch mode decreases with increasing hydrostatic pressures beyond about 1 GPa (McCluskey and Haller, 1997). This can be explained as a change from a D_{3d} configuration at low pressures to the buckled form for pressures ∼1 GPa.

Table 4.5: Calculated values for the isotropic piezospectroscopic tensor element A_1 ($cm^{-1}GPa^{-1}$) for local modes of O_i along with the experimental data. Grüneisen parameters for each mode are between parentheses.

Mode	Si:C_2		Si:D_{3d}		Obs.	Ge:C_2	
$A_{2u} + A_{1g}/A + B$	−0.78	(−0.13)	2.28	(0.37)		3.68	(0.50)
A_{2u}/B	−2.11	(−0.55)	1.81	(0.45)	0.77[a], 0.2[b]	1.64	(0.44)
A_{1g}/A	1.33	(0.62)	0.47	(0.22)		0.82	(0.50)
$E_u/A, B$	0.86	(0.47)	0.84	(0.47)	∼1.1[b]		

[a]McCluskey and Haller (1997)

[b]Bosomworth *et al.* (1970)
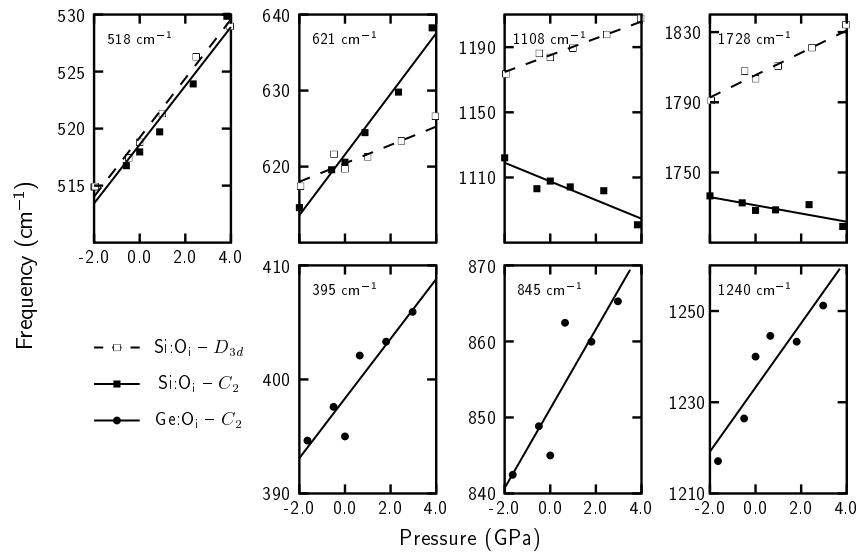
Figure 4.4: Effect of pressure on LVMs of interstitial oxygen in Si (upper row) and Ge (lower row).

4.2.4 Stress-energy tensor

The stress tensor for O_i in Si has been calculated as described above. We find the principal values for the D_{3d} structure are $B_3 = -2B_2 = -2B_1 = -10.71$ eV with the principal direction of B_3 along the C_3 axis. The negative value of B_3 indicates that the defect is compressive along the Si-O-Si bond as expected. These are in fair agreement with the experimental results of $B_3 = -2B_2 = -2B_1 = -15.2$ eV (Watkins, 1996).

4.2.5 Diffusion of interstitial oxygen

Detailed experimental studies have established that the diffusion process is governed by the hopping of a single oxygen atom between bond centered sites with an activation energy of 2.53 eV (Mikkelsen, 1986). However, theoretical studies have enjoyed mixed success in reproducing this fundamental property. Early cluster calculation by Jones *et al.* (1991) gave 2.8 eV but this value has not been found by supercell calculations where an underestimation has been consistently reported (Ramamoorthy and Pantelides, 1996; Needels *et al.*, 1991*a*; Oshiyama and Saito, 1990; Capaz *et al.*, 1999). The diffusion barrier is the energy difference between the buckled stable configuration and the saddle point which has long been considered to be the Y-lid configuration where the oxygen atom lies mid-way between two second neighboring Si atoms. This energy difference has been found between 1.8 and 2.2 eV and it has been suggested that this discrepancy arises from the neglect of the kinetic energy of the O atom (Needels *et al.*, 1991*b*), and subsequently to the neglect of a simultaneous motion of Si neighbors (Ramamoorthy and Pantelides, 1996). However, reaction rate theory includes both of these effects and assumes only that the system once reaching the saddle point executes a diffusive step (Flynn, 1975).

The activation energy for an oxygen atom hopping between neighboring bond centers in Si has been measured by stress-induced dichroism (Corbett *et al.*, 1964*a*) to be 2.56 eV and the same barrier was found for the long range diffusion of oxygen as measured by secondary-ion mass spectrometry (Mikkelsen, 1986). In Ge, the diffusion energy is 2.08 eV (Corbett *et al.*, 1964*a*). The similarities in the oxygen diffusion energies in Ge and Si suggests an

identical diffusion mechanism.

The saddle point for hopping between bond centers has been found to be the Y-lid configuration with C_{2v} symmetry and shown in Figure 4.1(c) (Jones *et al.*, 1991). In this configuration, both the O atom and the Si_1 neighbor are three-fold coordinated.

The energy of the Y-lid was calculated by relaxing 32, 64 and 128 atom cells with the symmetry maintained to be C_{2v}. The lattice parameter was again taken to be given by the calculated bulk value. We found that in Si this energy is 2.1 to 2.2 eV higher than the C_2 structure when using cells with these sizes (Coutinho *et al.*, 2000b). Allowing the volume of the cell to relax lowered the energy of the Y-lid configuration by 10 meV. This has negligible effect on the diffusion energy, and gives us confidence regarding the size of the supercell. If the O atom is slightly perturbed, then, upon relaxation without any constraint, it returns to the stable C_2 site. Thus the calculated diffusion energy is about 2.2 eV compared with an experimental value of 2.5 eV. This may be compared with previous estimates of 2.8 (Newman and Jones, 1994), 1.8 (Needels *et al.*, 1991a), 2.2 (Ramamoorthy and Pantelides, 1996), and 2.0 eV (Oshiyama and Saito, 1990).

In a similar way, the energy of the Y-lid structure in Ge is found to be 1.70 eV above its ground state. In both materials, the diffusion barrier is underestimated by about 0.3 eV. This may result from inadequacies in local density functional theory or slow convergence in cell size or basis.

An intriguing problem is the fact that pre-exponential factor D_0 has been measured as 0.13 cm^{2}s^{-1}, corresponding to an attempt frequency of 3.5×10^{14} s^{-1}. This also suggests a hopping enhancement due to about $4k_B$ of motional entropy (Newman and Jones, 1994). Although this is not clear, several reasons could explain this effect (Stoneham, 1989): (i) vibrational entropy, (ii) configurational entropy, (iii) thermal expansion.
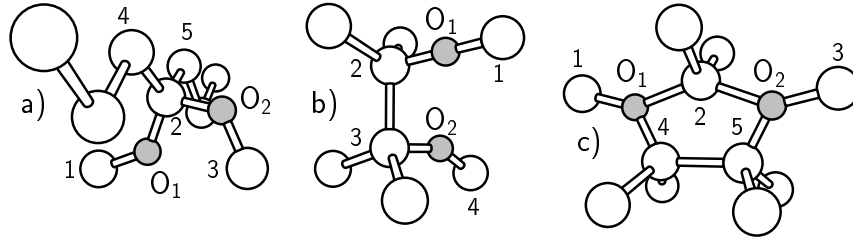
Figure 4.5: Schematic structure of oxygen dimers. a) Staggered (O_{2i}^{st}), b) Skewed (O_{2i}^{sk}), and c) Double Y-lid (O_{2i}^{dy}). Oxygen atoms are grey.

4.3 Interstitial oxygen dimer

4.3.1 Introduction

One puzzling feature that characterizes the TDD growth process, is its low ~1.8 eV activation energy (Wagner *et al.*, 1992; Newman and Jones, 1994). If the conversion is due to oxygen aggregation, then this implies that some oxygen species can diffuse at a much faster rate than isolated oxygen atoms. Moreover, careful studies of the loss of the intensity in the 1136 cm^{-1}-band with prolonged anneals below 500°C, strongly suggest a fast diffusing dimer. This makes the dimer species a key entity in kinetic studies of oxygen aggregation in Si (Åberg *et al.*, 1998; McQuaid *et al.*, 1999).

The first suggestion for a fast diffusing oxygen-related species was made by Gösele and Tan (1982) and attributed to an O_2 molecule. However, later calculations indicated that the molecule was less stable than an oxygen dimer where both oxygen atoms are tilted along the $\langle 110 \rangle$ direction with respect to each other (see Figure 4.5(a)) (Needels *et al.*, 1991*a*). Here the oxygen atoms were found to be bound by 1 eV.

Subsequent infra-red absorption studies have identified the LVMs of an oxygen dimer. These lie at 1060, 1012, 690 and 556 cm^{-1}. The intensities of these modes vary with the square of the O_i concentration (Öberg *et al.*, 1998) and in the ^{16}O-^{18}O mixed isotopic case, unique modes are detected demonstrating the presence of two oxygen atoms that are dynamically coupled. The two oxygen atoms, O_1 and O_2, must be inequivalent as

122

these unique modes are only found in one of the $^{16}O_1$–$^{18}O_2$ combinations. This unusual behavior is reflected in the intensities of the modes (Öberg *et al.*, 1998).

Further investigations suggested that a second dimer, called the skewed (see Figure 4.5(b)) because a Si-Si bond separates the Si-O-Si units which lie in different {110} planes, is energetically competitive with the staggered dimer (Murin *et al.*, 1998; Öberg *et al.*, 1998). Previously, we found, using the cluster method, that the skewed dimer possesses LVMs closer to the experimental values than those of the staggered dimer. The converse was, however, found by Pesola *et al.* (1999*b*). To address this problem, the LVMs have been re-evaluated using the supercell method.

In Ge, interstitial oxygen dimers have only been identified recently (Litvinov *et al.*, 2001). Here only the high-frequency bands were observed. Their location at 780.5 and 818.0 cm^{-1} is very near to what we would expect after scaling bands in Si by $\nu_{Ge}/\nu_{Si} = 862/1136$, where ν_{Ge} and ν_{Si} are the asymmetric stretch mode frequencies of O_i in Si and Ge respectively. Annealing kinetics studies estimate that to O atoms are bound by $\sim$0.4 eV — about 0.1 eV stronger than the dimer in Si (Litvinov *et al.*, 2001). Despite that only few theoretical studies have been performed (Chadi, 1996), it is reasonable to expect that oxygen clustering in Ge will start with the dimer formation as in Si.

4.3.2 Structure of the oxygen dimer

The structures investigated, i.e., the staggered, skewed, and double-Y-lid dimers shown in Figure 4.5, were calculated mainly in 64 atom supercells, although some calculations used 96 or 216 atom supercells (Coutinho *et al.*, 2000*b*).

Table 4.2 gives the formation energy of these dimers. Cells with 64 and 96 silicon atoms give values within 0.04 eV, suggesting that they are sufficiently large. The formation energy calculated in the largest 216 cell is not necessarily more accurate than found in the 64 or 96 atom cells as only one **k**-point (Γ) was used to sample the band structure in this case. Figure 4.2(b) demonstrated that the effect of allowing the cell volume to relax is negligible consistent with the view that 64 atom cells are sufficiently large.

Table 4.6: Binding energies (eV) for interstitial di-oxygen centers in Si and Ge. *fccN, scN, bccN* and *ttrN* denote face-centered-cubic, simple-cubic, body-centered-cubic and tetragonal cells with N Si or Ge atoms. In the third column, n denotes the BZ sampling scheme utilized.

	Crystal	MP-n^3	Cell	O_2^{st}	O_2^{sk}	O_2^{dy}
	Si	1	sc216	0.44		
This work	Si	2	sc64	0.54	0.35	−1.17
	Si	2	ttr96	0.58		
Pesola *et al.* (1999a)	Si	1	fcc128	0.2	0.1	
	Si	2	bcc32	0.6	0.2	
Chadi (1996)	Si		bcc32	0.4		
Needels *et al.* (1991a)	Si		fcc16 − sc64	1.0		
This work	Ge	2	sc64	0.62	0.07	−1.23
	Ge	2	ttr96	0.65		
Chadi (1996)	Ge		bcc32			0.7

The binding energies for the dimers obtained from the formation energies in Table 4.2 are given in Table 4.6 where they are compared with previous studies.

The binding energy of the oxygen atoms in the staggered dimer is found to be about 0.5 and 0.6 eV in Si and Ge respectively. An experimental estimate in Si is about 0.3 eV Murin *et al.* (1998). The skewed configuration is less favored by about 0.2 eV in Si, but is only marginally bound in Ge. Table 4.7 gives structural details of the dimers.

The symmetric double-Y-lid dimer is found to be energetically disfavored by about 1.2 eV relative to two isolated oxygen atoms in both Si and Ge. This is in contrast with previous work on this structure in Ge which found this structure to be bound with an energy of 0.7 eV.Chadi (1996) Nevertheless, the 1.2 eV required to form the symmetric double Y–lid suggests that the dimer can diffuse with at least this activation energy which is lower than the barrier for single oxygen diffusion. This is a subject we shall investigate in the next

Table 4.7: Bond lengths (Å) and angles (degrees) for oxygen dimers in Si and Ge (represented by X), shown in Figure 4.5.

Crystal	Si			Ge		
Dimer	staggered	skewed	double-Y-lid	staggered	skewed	double-Y-lid
O_1–X_1	1.66	1.61	1.75	1.77	1.73	1.86
O_1–X_2	1.64	1.62	2.11	1.74	1.74	2.19
O_1– X_4			1.75			1.85
O_2– X_2	1.63		2.11	1.74		2.19
O_2– X_3	1.67	1.63	1.75	1.77	1.75	1.86
O_2– X_4		1.63			1.74	
O_2– X_5			1.75			1.85
X_2–X_3		2.29			2.39	
X_4–X_5			2.37			2.57
X_1–O_1–X_2	130	166	146	125	147	147
X_1–O_1–X_4			131			128
X_2–O_2–X_3	127		146	124		147
X_3–O_2–X_4		148	131		138	128

section.

We also investigated the O_2 molecule lying at a T–site. This oxygen dimer is not stable: being 6.03 eV higher in energy than the staggered dimer. We discuss the stability relative to VO_2 in Subsection 4.5.2 and now turn to the vibrational modes of the dimers.

4.3.3   Local vibrational modes

The LVMs for the staggered and skewed dimers were found by evaluating the energy second derivatives between the O atoms and their Si neighbors. They are given in Tables 4.8 and 4.9 along with the observed modes. There are five modes of the dimer but only four have been detected. The calculated modes are within 40 cm^{-1} of the observed ones. However, of great importance is their isotopic shifts. For the staggered dimer, when the oxygen atom labeled O_2 in Figure 4.5 is replaced by its ^{18}O isotope, the 1017 cm^{-1}-mode drops only by 2 cm^{-1} but the 984 cm^{-1} mode drops by 41 cm^{-1}. These are in excellent agreement with observed drops of ~ 0 and 42 cm^{-1} respectively. However, when O_1 in Fig. 4.5 is replaced by ^{18}O, the 1017 cm^{-1}-mode is expected to drop by about 40 cm^{-1} bringing it close to the 984 cm^{-1}-mode. The two modes then are in resonance and become coupled leading to shifts of 28 and 17 cm^{-1} in each mode. These are to be compared with observed shifts of 39 and 8 cm^{-1}. Clearly the degree of coupling is overestimated but is less than that found by the cluster method previously.

The calculated shifts in the 705, and 666 cm^{-1}-modes are 14 and 10 cm^{-1} respectively and 0 cm^{-1} for the 543 cm^{-1}-mode. These shifts are in reasonable agreement with shifts in the observed bands at 690 and 556 cm^{-1}.

In the skewed configuration, the modes are essentially decoupled and the frequencies too high. They resemble those of two isolated oxygen interstitials. This suggests that the observed modes arise from the staggered dimer.

Only one of the modes around 690 cm^{-1} has been detected probably because the transition moment in the other is very small. The displacements of the atoms are shown schematically in Figure 4.3(d) and (e). Locating point charges at each O and neighboring Si atoms, leads

Table 4.8: Calculated LVMs (cm^{-1}) and their downward isotopic shifts for staggered and skewed dimers (O_{2i}^{st} and O_{2i}^{sk} respectively) in Si, along with the experimental observations.

	$^{16}O_1, {}^{16}O_2$		$^{16}O_1, {}^{18}O_2$		$^{18}O_1, {}^{16}O_2$		$^{18}O_1, {}^{18}O_2$	
	Calc.[a]	Calc.[b]	Calc.[a]	Calc.[b]	Calc.[a]	Calc.[b]	Calc.[a]	Calc.[b]
	1017	1033	2	1	28	40	46	46
	984	984	41	42	17	6	42	42
Si:O_{2i}^{st}	705	697	4	4	9	6	14	11
	666	661	9	6	3	3	10	8
	543	566	0	0	0	0	0	0
	1166	1104	0	1	52	52	53	50
	1094	1091	48	48	1	−3	49	50
Si:O_{2i}^{sk}	636	643	3	2	0	1	3	3
	624	627	1	1	0	2	1	3
	552	558	0	0	0	0	0	0
	1060		∼0		39		48	
	1012		42		8		43	
Observed[c]	690		4		∼4		10	
	—		—		—		—	
	556		∼0		∼0		0	

[a]This work

[b]Pesola *et al.* (1999*b*)

[c]Öberg *et al.* (1998)

to an induced dipole moment which is three times greater in the 705 cm^{-1}-mode than in the 666 cm^{-1}-mode. This probably occurs as the displacements of the oxygen atoms are in phase in the 705 cm^{-1}-mode and out of phase in the 666 cm^{-1}-mode. We therefore assign the observed 690 cm^{-1}-band to the higher frequency.

In Ge, the dimer modes are very similar to those in Si and the two high frequency stretch modes are reduced by a factor of 0.77 from the asymmetric stretch mode of O_i while the lower pair are reduced by a factor of about 0.73. A band at 780 cm^{-1} detected in annealed electron irradiated oxygen-doped Ge has been attributed to the dimer (Whan, 1965). In a recent work by Litvinov et $al.$ (2001), this band was correlated with a second band at 818 cm^{-1}. Both 818 and 780 cm^{-1}-bands shift downwards by 42 and 40 cm^{-1} in ^{18}O doped samples, and its intensity has a square dependence on the concentration of oxygen. The position of the dimer bands and its isotopic shifts agrees with the calculated modes at 784 and 749 cm^{-1} which shift 41 and 38 cm^{-1} with ^{18}O doping. However, further work is necessary to observe the other modes of the dimer. Further support for the assignment of this band to an oxygen aggregate comes from recent findings of a strong enhancement in thermal-donor concentrations consequent upon annealing irradiated material containing the 780 cm^{-1} band (Klechko et $al.$, 1999).

The dimer modes in Si are observed to display an anomalous temperature dependence. Normally, the fundamental frequency of a defect increases with decreasing temperature resulting from a strengthened bonds arising from the lattice contraction. However, the bands at 1012 and 1060 cm^{-1} shift downwards with temperature (Öberg et $al.$, 1998). To investigate this anomaly we decreased the lattice parameter in the 64 atom supercell containing the staggered dimer. The effect was to decrease further the Si-O-Si angles, i.e., increase their buckling, and reduce the asymmetric stretch modes as shown in Figure 4.6. Thus, if the effect of lowering the temperature is simply to contract the lattice and impose a pressure on the dimer, then the upper two modes would decrease in frequency while the lower modes would increase. The same situation holds for the dimer in Ge — in contrast with what was found for O_i in this material. However, the band at 780 cm^{-1}, attributed to dimers in Ge does not appear to shift anomalously with temperature. There clearly are

Table 4.9: Calculated LVMs (cm^{-1}) and their downward isotopic shifts for staggered and skewed dimers (O_{2i}^{st} and O_{2i}^{sk} respectively) in Ge, along with the experimental observations.

	$^{16}O_1$, $^{16}O_2$	$^{16}O_1$, $^{18}O_2$	$^{18}O_1$, $^{16}O_2$	$^{18}O_1$, $^{18}O_2$
	784	8	17	41
	749	32	23	38
Ge:O_{2i}st	517	8	11	22
	466	13	9	18
	849	4	1	44
	843	40	42	44
Ge:O_{2i}sk	389	1	10	11
	366	7	0	7
	818			42
Observed[a]	780			40

[a]Litvinov *et al.* (2001)
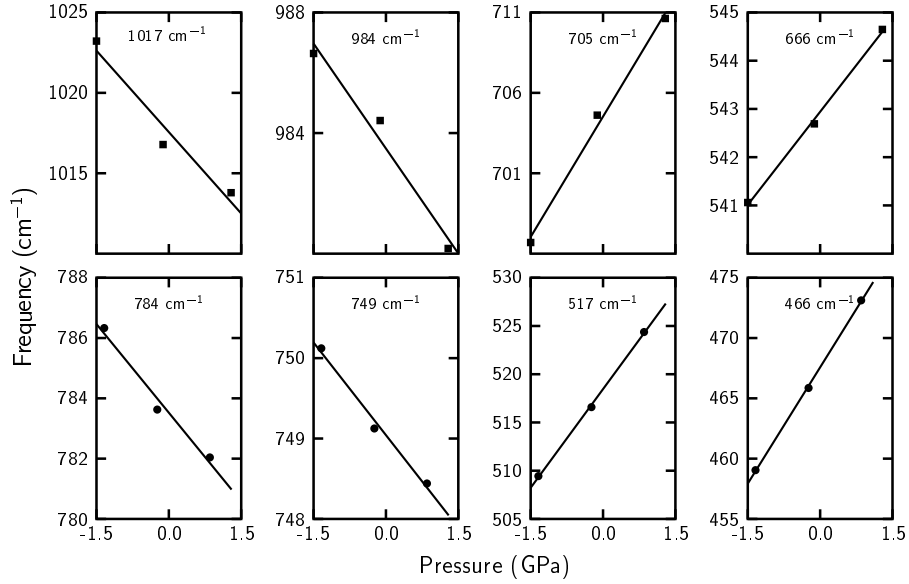
Figure 4.6: Effect of pressure on LVMs of the staggered dimer in Si (upper row), and Ge (lower row).

two opposing effects at work: the first is an increased buckling which leads to a downward shift in frequency, and the second is the compression of the X-O bond lengths which lead to a frequency increase. In Si, the first effect is dominant, but the second dominates in Ge.

4.3.4   Stress-energy tensor

The staggered dimer has C_{1h} symmetry, and hence its stress-energy tensor will have one principal direction (say B_2) normal to a $(10\bar{1})$ plane where the defect lies. The other two principal directions, B_1 and B_3, lie on that plane, but will be rotated by an angle θ away from the crystallographic directions [010] and [101] respectively. This can be seen in Figure 4.7. The calculations give principal values of -9.29, 6.17 and 3.12 eV for B_1, B_2 and B_3 respectively, with $\theta_B = 31°$. This defect can be then understood as a perturbed O_i. Figure 4.7 indicates that the compressive component B_1 is $\sim 4°$ away from the $[1\bar{1}1]$ trigonal direction. The staggered dimer is formed by two unequivalent O-atoms. One of them (O_1 in Fig. 4.5(a)), is near the bond-center site, and dominates the B-tensor
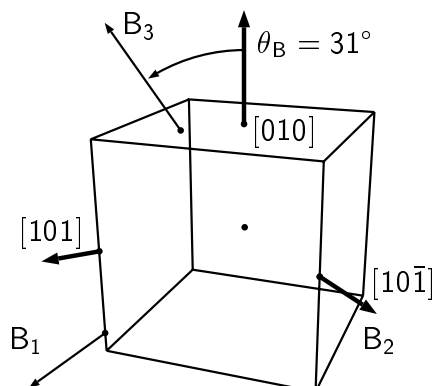
Figure 4.7: Principal directions of the stress-energy tensor for the oxygen dimer. The defect lies on the $(10\bar{1})$ plane.

properties. The other O-atom is strongly buckled and acts as a perturbation.

4.3.5 Diffusion of the dimer

The activation energy for movement of the dimer was investigated using three different diffusion paths (Coutinho *et al.*, 2000*b*): (i) a correlated jump of both oxygen atoms from the staggered configuration through the asymmetric double-Y-lid structure of Figure 4.8(i), (ii) a partial dissociation involving an asymmetric Y-lid as in Figure 4.8(ii), and a transition between the staggered and skewed dimers as proposed by Pesola *et al.*Pesola *et al.* (1999*b*) and shown in Figure 4.8(iii). The migration energies were determined by relaxing the cell with constraints on the lengths of the O-X bonds as described earlier and shown in the figure.

Path (i) leads to a migration energy of 1.4 eV, (ii) leads to a similar barrier of 1.6 eV, although the complete diffusion event requires the oxygen atom at the left side to make a similar jump to reform the dimer. However, symmetry considerations require this second step to be equivalent to the first. Path (iii) is activated by a barrier of 2.2 eV, and resembles the diffusion of isolated interstitial oxygen.

One can rationalize these results by noting that in (i) both three-fold coordinated Si
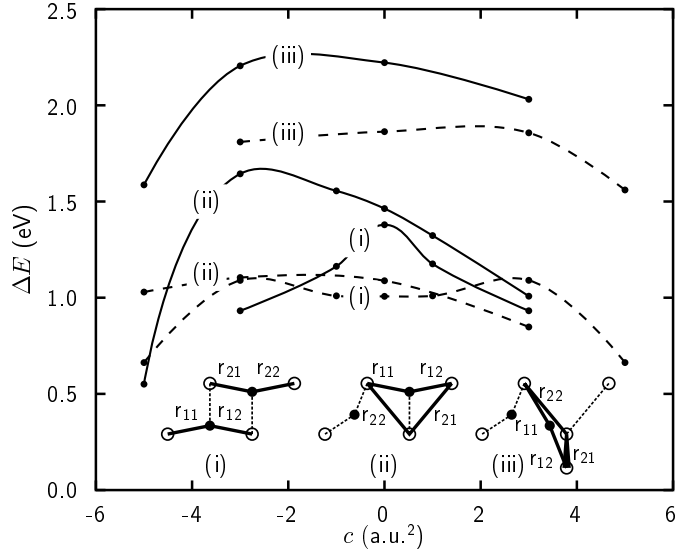
Figure 4.8: Energies, eV, along three diffusion paths discussed in the text for oxygen dimers in Si (solid lines) and Ge (dashed lines). ΔE is the energy relative to a stable dimer. The x-axis refers to the value of the constrained variables $c = \mathbf{r}_{11}^2 - \mathbf{r}_{12}^2 = \mathbf{r}_{21}^2 - \mathbf{r}_{22}^2$.

atoms labeled 1 in Figure 4.1(c) are now bonded to the other O-atoms. Similarly, in (ii) the tensile strain along [110] in the Y-lid is off-set by the presence of the second O atom. The effect of both these processes is to transport the dimer along [110] but both lead to a staggered dimer which tilts in the opposite direction. Before long range migration can occur, the dimer must reorientate and point in the opposite direction. The energy barrier for this is found to be below 0.38 eV in Si and 0.65 eV in Ge.

Thus we conclude that the diffusion path probably occurs by the staggered dimer migrating along its [110] axis with a correlated jump of both oxygen atoms.

For Ge, Figure 4.8 shows that the energy surface around the saddle-point is flatter than in Si. This is because the smaller Ge-O-Ge angle means that the oxygen atom is *closer* to the saddle point and consequently the *length* of the trajectory is shorter.

In summary, the calculations demonstrate that oxygen dimers diffuse in Si and Ge with barriers about 0.8 and 0.6 eV respectively below the calculated barriers for O_i.

4.4 Formation of staggered aggregates

4.4.1 Introduction

The idea of a fast-diffusing O-dimer opens up several questions. Such dimers would be expected to be trapped mainly by single oxygen interstitials and form trimers. If the trimer were stable and immobile, then their concentration would gradually build up and larger oxygen aggregates would not easily form. The trimer bottleneck can be removed in two ways. Either the binding energy of the trimer is negligible so that they dissociate into dimers and O_i, and further growth is based on dimer association, or the trimer is stable but mobile and O_{4i} defects are rapidly formed. The first hypothesis requires that the trimer is unstable but previous calculations suggest that this is not the case (Chadi, 1996; Pesola *et al.*, 1999*a*). However, the other proposal leaves unresolved the rate at which larger aggregates can form. One suggestion is that these aggregates along with thermal donors are all mobile (Murin and Markevich, 1996).

4.4.2 Chain energetics

We find that oxygen atoms cluster preferentially along [110] directions with decreasing Si-O-Si angles with increasing chain length (see Fig. 4.9(a). As all O-atoms bridge first nearest Si neighbours, we shall refer as O_n-1NN to these chains.

Formation energies relative to quartz, vary from 1.81 eV, for the single interstitial, to about 1.0 eV per oxygen atom for the longer chains. Despite the clear *driving force* to form these 1NN aggregates, saturation is attained for chains with more that 6-7 oxygen atoms.

4.4.3 Migration of oxygen-chains

Consider, now the migration of such chains. As the chain moves through the lattice along the [110] valley in which it lies, a single or group of O atoms moves to the symmetric Y-lid

Table 4.10: Formation energies per oxygen atom of O_n-1NN chains in Si, with n between 1 and 9. All values are relative to the energy of each O-atom in a α-SiO$_2$ environment. Binding energies $E_b = [E_f(n-1) + E_f(1)] - E_f(n)$ are also included. All values in eV.

	1	2	3	4	5	6	7	8	9
$E_f(n)/n$	1.81	1.54	1.33	1.23	1.18	1.13	1.10	1.06	1.05
E_b		0.54	0.91	0.88	0.84	0.91	0.90	1.04	0.80

configuration as illustrated in Fig. 4.9(b). An upper limit for the diffusion barrier is found by relaxation with a constraint that forces atoms to approach this configuration. In Si, this energy drops from 2.2 eV for the single oxygen species to 1.4, 1.3 and 1.2 eV for O_n, $n = 2$, 3 and 4 Coutinho et $al.$ (2000a). For Ge, there are similar reductions. Despite the underestimation of the migration barrier for O_i, a rapid diffusion of oxygen chains is to be expected with a barrier around 1.2 eV and 1.0 eV in Si and Ge respectively. The marked reduction of the migration barriers comes from two effects. Firstly, the decreasing Si-O-Si angles which bring the staggered form closer to the Y-lid form, and secondly, the absence of Si dangling bonds at the saddle point for all clusters $except$ O_1. This is clearly shown in Figure 4.9(b). With isolated oxygen concentrations of $\sim 10^{18}$ cm^{-3} and maximum donor concentrations of $\sim 10^{16}$ cm^{-3} the diffusing chain will most likely encounter a single oxygen interstitial, either lying in the same or a nearby $\langle 110 \rangle$ valley. In the latter case, there will have to be single oxygen jump before a longer chain is formed. It is this rapid chain diffusion which enables long chains to grow rapidly Lee et $al.$ (2001), but raises the question as to whether the increasing stress leads to a kick-out of a Si interstitial. This issue is dealt in Section 4.5.
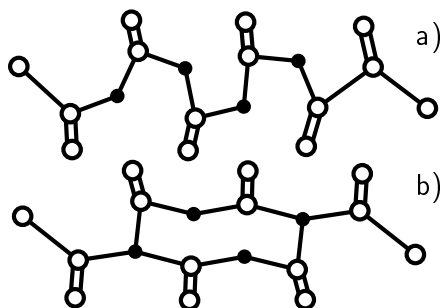
Figure 4.9: The staggered O_4 chain aligned along [110]. b) structure close to saddle-point for migration of the chain. This structure could be displaced to *fall* either into a) or the structure in a) displaced along [110]. White and black spheres are Si and O atoms respectively.

4.5 Ejection of self-interstitials

4.5.1 introduction

Another important question concerns the critical size of an oxygen aggregate which is thermodynamically unstable against vacancy-oxygen (VO_n) formation. As oxygen clusters grow, there is a an increase in strain energy which will be relieved at a critical size by the ejection of a self-interstitial (I). We will show here that VO_n formation becomes exothermic only for $n = 4$ but the activation barrier probably prevents this happening around 450°C.

4.5.2 Energetics of VO_n against O_n defects

Simple geometric considerations suggests that oxygen clusters beyond a certain size are unstable and release a Si self-interstitial forming a VO_n defect. We investigate these reactions in detail and conclude that they can spontaneously occur only for n equal or greater than 4 (Coutinho *et al.*, 2000*a*). The energy of the reaction $O_{ni} \rightarrow VO_n$ is found by moving the abstracted Si atom to a reservoir of bulk Si. Thus for neutral defects, ΔE_f is simply $E_f(VO_n) + \mu - E_f(O_{ni})$ where μ is the energy of a Si atom in bulk material.

Figure 4.10: Formation energies of VO_n defects and staggered O_n chains, a) Si, b) Ge. Formation of each VO_n defect imply the creation of a bulk Si/Ge atom.
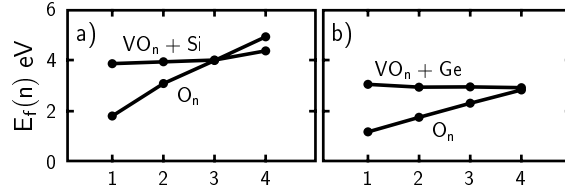
Figure 4.10 (right) gives these formation energies found from supercells of 128 atoms and demonstrates that the threshold for the reaction is around $n = 4$.

The activation barrier to the process must include the formation energy of the self-interstitial near the vacancy aggregate. It is not clear what this barrrier is but when the interstitial is far from VO_n, then the energy difference includes the formation energy of the interstitial which is found to be around 3.3 eV in both Si and Ge respectively. It is unlikely that this barrier can be reduced significantly by the formation of an IO_n defect as such complexes are not thought to be stable above 200°C (Abdlullin *et al.*, 1998; Hermansson *et al.*, 1999). As the formation rates of thermal donors are activated with much smaller barriers, we conclude that VO_4 defects will not be formed around the temperatures where thermal double donors are stable.

4.6   Summary

In summary, the calculations find that interstitial oxygen in Si, at normal pressures, is likely to tunnel between bent Si-O-Si configurations with effective D_{3d} symmetry. In this configuration, there are two localized fundamentals at 1184 (A_{2u}), 619 (A_{1g}) and an E_u resonance at 519 cm^{-1}. The frequency of the modes increase with pressure. However, for a critical pressure, the energy difference between the C_2 and D_{3d} configurations increases, and tunneling no longer occurs. In this case the O atom could still rotate around the $\langle 111 \rangle$ axis with the asymmetric stretch mode decreasing with increasing pressure.

In germanium, the D_{3d} structure has energy 0.1 eV higher than the others which are all

degenerate (see Table 4.1). The Ge-O-Ge angle is $143°$ and the oxygen atom lies 0.55 Å away from the BC site with the Ge-O bond length at 1.73 Å. The energy barrier to the D_{3d} case suggests that tunneling cannot occur, but the oxygen atom may rotate around the $\langle 111 \rangle$ axis. Table 4.4 gives the calculated and experimental LVMs. Two fundamental LVMs lie at 847 and 401 cm^{-1} and represent asymmetric and symmetric stretch modes of the Ge-O-Ge buckled unit. In general, these results are in agreement with previous investigations (Martinez *et al.*, 1987; Jones *et al.*, 1992; Artacho *et al.*, 1982; Pesola *et al.*, 1999a; Laßmann *et al.*, 1999). In contrast with Si, these frequencies do not drop with increasing pressure and no mode around the Raman frequency occurs. The difference in behavior is probably due to the very different bond angle in the two materials.

The oxygen dimer, in both Si and Ge, is stable in the staggered form with modes calculated to be in good agreement with experiment. It is surprising that the two stretch modes of the dimer, in which the oxygen atoms share a common Si neighbor, are *almost* dynamically decoupled. The anomalous temperature dependence for the modes in Si has been linked to an increased buckling occurring during the contraction of the crystal when cooled. This seems to be a signature of a buckled oxygen bridge in Si and its observation has implications for other defects. The dimer is found to be stable against the formation of O_2 molecules. The barrier to diffusion of the dimer is about 0.8 eV and 0.6 eV lower in Si and Ge respectively than that of O_i. The diffusion path involves a concerted movement of the pair of atoms along a path which eliminates dangling bonds at the saddle point.

In conclusion, we have shown that oxygen atoms lying in chains diffuse quickly and form extended chains lying along [110]. The most stable small chains involve O atoms linking first neighbouring Si atoms (O-1NN). The chains are less stable than an SiO_2 precipitate but form through their rapid kinetics.

A comparison between the formation energies of O_{ni} and VO_n defects, leads us to conclude that the ejection of self-interstitials from O_{ni} aggregates does not occur for $n \leq 4$. The reaction is exothermic for O_{4i} defects in Si but the activation barrier prevents this happening during TDD growth.

Chapter 5

Thermal double donors

5.1 Introduction

Thermal double donors (TDD) are formed by annealing oxygen rich Si or Ge at temperatures between 300 and 500°C. They comprise a family of at least 16 double donors which form sequentially and are distinguished by their increasingly shallow levels (Jones, 1996). In spite of extensive studies, they remain a mystery. There are in essence two current models. The first, much favoured in theoretical studies (Snyder and Corbett, 1985; Jones, 1990; Chadi, 1996; Pesola *et al.*, 1999*b*; Ramamoorthy and Pantelides, 1999), suggests that they consist of an increasing number of O atoms surrounding a core containing at least one over-coordinated oxygen defect. The second considers them to be a silicon self-interstitial-oxygen complex $I_n O_m$ (Newman, 1985; Deák *et al.*, 1992). It must be admitted that the bulk of experimental evidence favours the latter. Three examples reveal the difficulties of the oxygen-only model. Firstly, the activation energy for the transformation of TDD(N) into TDD($N+1$) varies from 1.2 eV for $N = 1$, to 1.7 eV for larger N in Si. This leads to an anomalously fast transformation when compared with the 2.5 eV migration barrier for oxygen (Newman, 2000). Secondly, EPR and ENDOR studies on the NL8 family, assigned to TDD(N)$^+$, reveal two shells of O atoms, apparently bridging neighbouring Si atoms, possessing almost infinitesimally small spin-densities (Michel *et al.*, 1989; Spaeth, 1996).

The isotropic ^{17}O hyperfine interaction is less than 0.5 MHz in NL8 and much less than 3 MHz found on oxygen in VO$^-$, in spite of the fact that oxygen in VO$^-$ is located in a nodal plane of the spin-density (van Kemp *et al.*, 1989*b*). How, one wonders, can the source for the donor activity be oxygen when there is so little spin-density associated with it? Thirdly, the oxygen-only model requires an increasing number of oxygen related local vibrational modes (LVMs) to be associated with the later donors, but only at most two such modes have been assigned to any donor (Lindström and Hallberg, 1994, 1996). Thus, any credible model must address all these well established observations.

5.2   The self-interstitial model

It is well known that carbon suppresses TDD formation in Si (Newman and Willis, 1965; Bean and Newman, 1972). Although this suppression process is not well understood, both the oxygen-only and self-interstitial-oxygen models give an explanation. In the oxygen-only model it is argued that diffusing oxygen is trapped by substitutional carbon. The resulting C_sO_n defects have been reported in the literature to appear during TDD annealing conditions (Bean and Newman, 1972; Yamada-Kaneta *et al.*, 1996). However, according to the self-interstitial-oxygen model, I defects are trapped by C_s (Ourmazd *et al.*, 1984), and via Watkins replacement mechanism, produce carbon-interstitial defects (C_i). The later are necessary to explain the appearance of the photoluminescent T-line at 0.935 eV, associated with the C_iC_sH complex, which appears after prolonged 450°C heat treatments of oxygen-rich Si (Safonov *et al.*, 1996).

The most successful TDD model containing self-interstitials was proposed by Deák *et al.* (1992). As shown in Figure 5.1(c), labelled as form-U_1 (*unstable one*), its active core consists of two oxygen atoms bonded to a self-interstitial located nearby the T-site. The popularity of this model relies fundamentally on the fact that it possesses C_{2v} symmetry, and no O atom is present in the C_2 symmetry axis along [001], consistent with the ENDOR data. Its donor activity arises from the overlap of anti-bonding crystal states with the silicon-interstitial.

Table 5.1: Binding energies E_b, and relative energies E_r^q in charge state q (eV) for all structures considered (see Figs. 5.1 and 5.2). Binding energies represent the total energy difference between an IO_2 defect and a staggered dimer plus a split-interstitial infinitely separated.

Structure	E_b	E_r^-	E_r^0	E_r^+
A	0.39	0.57	0.35	0.00
B	0.75	0.03	0.00	0.07
C	0.63	0.00	0.13	0.34
U_1	-4.78		5.53	
U_2	-0.19		0.94	
U_3	-0.43		1.18	
U_4	-0.38		1.13	

In agreement with Deák *et al.* (1992), we found the symmetric IO_2 model to be a good candidate as a shallow double-donor. It possesses a fully occupied Kohn-Sham band *touching* the conduction-band. However, we abandoned this model as it is not stable. Its total energy is 5.53 eV higher than that the form-B of the IO_2 defect depicted in Figure 5.2(c). In fact the symmetric U_1 model is 4.78 eV more costly than a split-interstitial far away from a staggered O_{2i} defect (see Table 5.1). Figure 5.1 shows other IO_2 complexes with C_{2v} symmetry, but as shown in Table 5.1, all were found to be unstable.

Within the IO_n defects investigated, none of them possess binding energies compatible with the thermal stability of the TDD defects (see Table 5.1). Observations seem to support these results, as no IO_n complex has been observed above $\sim200°$C (Hermansson *et al.*, 1999). Early infra-red experiments by Whan (1966a,b) revealed three IR absorption bands located at about 936, 944 and 956 cm^{-1}, later assigned to arise from a I_2O_i (936 cm^{-1}) and IO_i (944 and 956 cm^{-1}) complexes (Whan and Vook, 1967; Hermansson *et al.*, 1999).
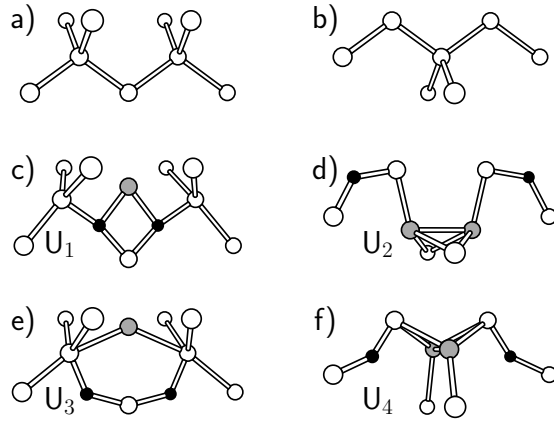
Figure 5.1: Unstable and metastable structure candidates for an IO_2 complex. Oxygen and Si atoms are black and white respectively. a) and c) are pure Si regions where the defects lie. In c) and e), the self-interstitial is near the T-site — grey atom. In d) and f) two Si atoms share a Si site (grey atom), making a *split-interstitial*.

Recent IR absorption measurements in electron irradiated Cz-Si revealed an IO_2 complex (Lindström *et al.*, 2001). Here, a clear correlation was found between the disappearance of bands from the oxygen dimer with the appearance of two bands at 1037 and 922 cm^{-1}. Again, this defect was found to break slightly above 200°C, and therefore also incompatible with the thermal stability of TDD defects.

Figure 5.2 shows the three favourite structures for the IO_2 defect. From Table 5.1 one can notice that all structures have similar formation energies, and each one is favoured for a particular charge state. Neutral forms B and C are separated by an energy barrier as small as 0.3 eV. This suggests that the defect could be bi-stable, or even tri-stable, depending on the position of the Fermi level. Bi-stability has been observed in a variety of defects like the EL2 in GaAs (Martin and Markram-Ebeid, 1992), thermal double donors (Makarenko *et al.*, 1985), C_sC_i pair (Song *et al.*, 1988), or the D1 shallow donor (Markevich *et al.*, 1994). This problem was reviewed by Watkins (1990), and is normally associated with large structural relaxations after capture or emission of carriers.

LVMs were calculated for forms B and C. These are compared with the observations
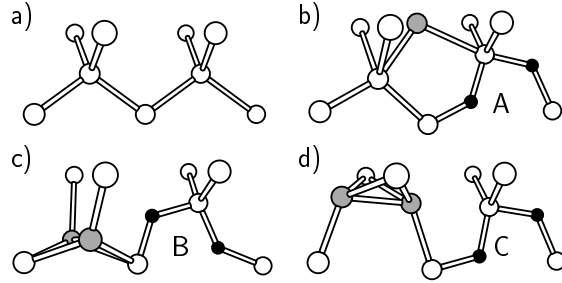
Figure 5.2: Lowest energy structures for an IO_2 complex. Oxygen and Si atoms are black and white respectively. a) is pure Si region where the defects lie. In b) the self-interstitial is near the T-site (grey atom). In c) and d) two Si atoms share a Si site (grey atom), making a *split-interstitial*. Structures b), c) and d) are the most stable in the positive, neutral and negative charge states.

in Table 5.2. Clearly, form-B is the one that better reproduces the measured absolute frequencies. Moreover, the absence of mixed modes is also accounted by form-B. The mixed-mode calculations indicate that despite their spatial proximity, both O atoms are almost dynamically decoupled, and splittings should be hidden under the ~ 6 cm^{-1}-wide ^{16}O-^{16}O and ^{18}O-^{18}O absorption bands.

DLTS experiments assigned an acceptor level at $E_c - 0.11$ eV to the IO_2 defect (Lindström *et al.*, 2001). However, no IR-bands were yet observed for the defect in the negative charge state. This could be an indication of bi-stability, and further work needs to be done. Nevertheless, the small binding energies of IO_n complexes and the high energy cost to eject a self-interstitial from a small O$_n$ defect, clearly favour the oxygen-only model.

5.3 Infinite oxygen-chains

As oxygen atoms were found to cluster preferentially long the [110] direction, several *periodic infinite* chains were investigated (see Fig. 5.3).

The most stable is the O-2NN model, shown in a), where oxygen atoms are bonded to second neighbour Si atoms in two parallel chains along [110] (Jones *et al.*, 2001). An inonic

Table 5.2: Calculated and measured LVM frequencies (cm^{-1}) for the IO_2 defect. First two columns are absolute frequencies, and columns three onwards are downwards isotopic shifts (cm^{-1}). ND stand for not detected.

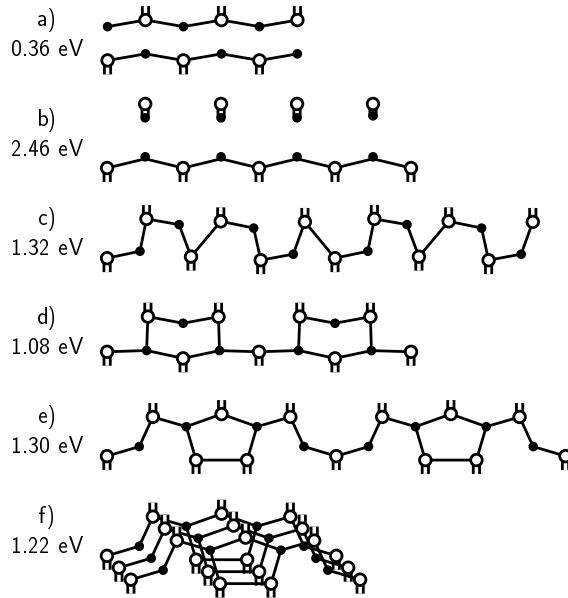|	^{16}O-^{16}O	^{16}O-^{18}O	^{18}O-^{16}O	^{18}O-^{18}O
	1020.7	44.9	0.3	45.8
	958.9	0.7	40.9	41.0
form-B	703.0	1.4	12.9	14.9
	659.1	7.1	1.4	7.9
	545.0	0.1	0.1	0.2
	929.6	2.4	23.5	41.1
	898.7	37.1	17.3	39.2
form-C	720.5	14.6	2.9	18.9
	667.4	2.8	12.3	13.7
	541.6	0.1	0.1	0.2
Obs.[a]	1037	ND	ND	46
	922	ND	ND	39

[a]Lindström *et al.* (2001)

Figure 5.3: Periodic infinite sub-oxide chains. a) O-2NN, b) VO_2, c) O_2-1NN, d) Ring, e) D-Ylid, f) parallel D-Ylid. Formation energies per O-atom are shown on the left hand side of each structure.

bonding character was found across and along the chains. We can then think that each oxygen atom is divalent, and each Si atom tetravalent. This is shown in Figure 5.4, where a plot of the total charge density reveals electrons much more localised on the anions (oxygen atoms), than on cations (Si atoms), i.e. the chain is a sub-oxide. The formation energy per oxygen atom (0.36 eV) is very small when compared with the 1.81 eV to for an isolated O_i defect. Nevertheless, this chain is metastable with respect to quartz, and it must break after sufficient annealing time.

It is tempting to identify the O-2NN chains with the donors. Although they have the same C_{2v} symmetry for odd n, this cannot be correct. The band structures for bulk Si and the infinite O-2NN chain, in same supercell, are shown in Figs. 5.5(a) and 5.5(b) respectively. These demonstrate that the chain is insulating with a highest occupied band close to that of bulk Si. They also reveal that the six degenerate lowest empty bands associated with the $\langle 100 \rangle$ valleys in bulk Si are split in O_∞-2NN, with the lowest pushed downwards by $\sim$0.2 eV from their centre of mass by the [001] stress arising from oxygen. The ionic
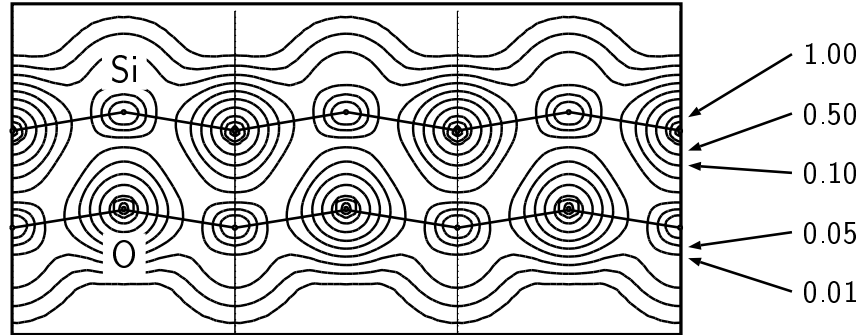
Figure 5.4: Contour plot of the charge density along the infinite O-2NN chain (see Fig. 5.3(a)). Contour levels (a.u.$^{-3}$) are shown on the right hand side of the plot.

character of the sub-oxide is supported by Fig. 5.9(a), which shows that the wavefunction of the empty stress induced gap level is localised on the Si cations and avoids the oxygen anions as expected for conduction band states in ionic materials.

5.4 The O-2NN model

5.4.1 Energetics and bi-stability

Finite O_n-2NN chains are terminated by O-atoms bridging Si nearest neighbours as shown in Fig. 5.6(b). Consequently, a topological defect involving an over-coordinated O-atom or an under-coordinated Si-atom, must be present at the interface between the two types of oxygen atoms. While short O_n-1NN chains — where all O atoms bridge first Si neighbours (see Fig. 4.9(a)) — are more stable than short O_n-2NN chains, the reverse is true for long ones and the cross-over occurs around $N = 6$ and $N = 8$ oxygen atoms. This cross-over is shown in Figure 5.8, where the stabilising factor in O_n-2NN chains is its low formation energy core. Note that each core oxygen atom only costs 0.36 eV.

It is known that the first three TDD members in Si (the first four in Ge), are bi-stable. They have an inactive species labelled X(N) and a double donor TDD(N) form. As shown in Figure 5.7, for $0 \leq N \leq 2$ the neutral X-form is more stable than the active form. As the
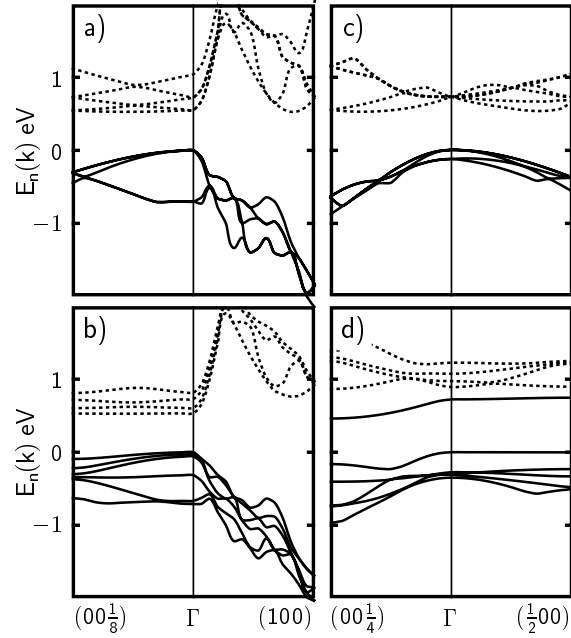
Figure 5.5: Band structure for a) defect-free Si in 48 Si atom supercell, and b) the same supercell containing the infinite O-2NN chain from Fig 5.6(a). Solid and dashed lines represent filled and empty states. Band gap of 0.54 eV in a) is consequence of density functional theory. Reciprocal-space points are in units of $2\pi/a_0$, where a_0 is the Si lattice constant. Note that degenerate valleys along (001) and (100) in a) are split in b). c) and d) show band structures for 112 Si atom defect-free supercell and same cell containing O_9-2NN as in Fig. 5.6(b). Note that d) exhibits double donor behaviour.
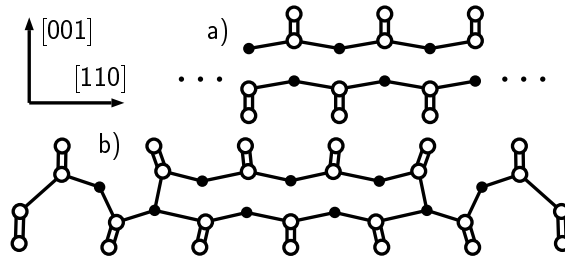
Figure 5.6: Most stable structures for a) *infinite chain* (referred as O_∞-2NN), and b) the TDD model O_9-2NN finite chain. O and Si are shown as black and white circles respectively.

donor form can be populated after illuminating the sample with above-band-gap light, non-equilibrium $(0/+)$ deep levels occur at 0.75, 0.48 and 0.29 eV bellow the conduction-band. In the TDD-form, the donor levels are shallow, and the system forms a negative-U, i.e., it is energetically favourable to form $TDD^{++} + TDD^0$ than $2 \times TDD^+$, and the positive defect is not thermodynamically stable. Hence the equilibrium $(0/++)$ occupancy level lies mid-way between the $(0/+)$ and $(+/++)$ levels. As the aggregation process goes on, the TDD(N)-form is stabilised, and a cross-over occurs for $N = 3$. Now the defects have a ground state with double donor character. Further details about bi-stability of defects can be found in a review by Watkins (1990).

In the TDD-form, the first ionisation energy is 69.2 meV $\geq E(0/+) \geq$ 49.9 meV for $1 \leq N \leq 11$, and second ionisation energy 156.3 meV $\geq E(+/++) \geq$ 116.0 meV for $1 \leq N \leq 9$. These are very close to He-like effective-mass binding energies, where $E(0/+) = 55.8$ meV and $E(+/++) = 126.8$ meV. For $N = 0$, the donor form is metastable by about 0.7 eV and of difficult preparation. Hence its donor levels where not measured yet (Murin, 2001).

As first suggested by Chadi (1996), the short 1NN chains (see Figure 4.9(a)) are good candidates for the X-form of the thermal donor defects. Here we support this assignment. As we shall see in Subsection 5.4.2, finite O_n-2NN chains are shallow double donors, and after looking again to Figure 5.8, we conclude that the first non bi-stable O_n-2NN defects have about 6 or 7 oxygen atoms.

5.4.2 The quantum dot analogy

Whereas the infinite chain is insulating, the finite chain is not. The highest occupied state in O_9-2NN shown in Fig 5.5(d) now borders the conduction band. It might then be expected that the wavefunction of this shallow double donor level must be localised on the over-coordinated oxygen atoms but, as Fig. 5.9(b) shows, this is not the case. The donor state is the *same* stress-induced gap state found for the infinite O-2NN chain. We understand this as follows. The interface region leads to an energy level lying *above* the strain
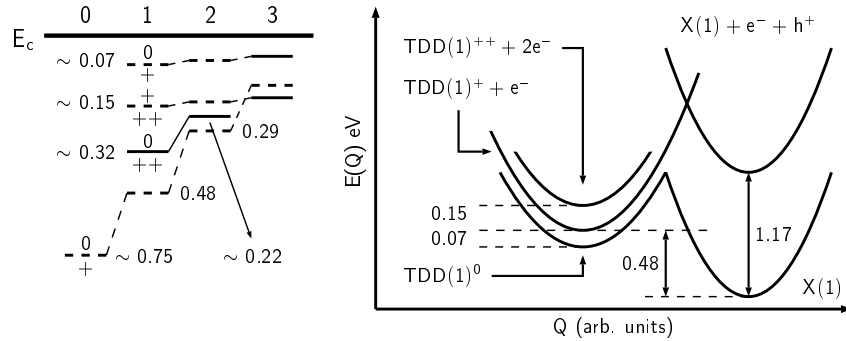
Figure 5.7: Configuration coordinate diagram for the thermal double donors in Si after Makarenko *et al.* (1985). All energies are given in eV. Solid and dashed levels represent equilibrium and non-equilibrium occupancy levels respectively.

induced gap level due to the O-2NN core. Consequently, electrons drop into the stress induced gap state with minimal overlap with oxygen. This explains the ENDOR/EPR results for a lack of spin-density on oxygen even though oxygen is the source of the donor activity (Jones *et al.*, 2001).

A simple analogy can be made with an externally doped GaAs quantum dot embedded in AlAs. An electron arising from a Si donor in the AlAs matrix drops into the lower lying unoccupied dot state arising from the band off-set between GaAs and AlAs. A magnetic resonance experiment then reveals a spin-density on Ga but not on Si. It might be then erroneously concluded that the source of the donor activity is a Ga interstitial. The important point is that these experiments do not reveal the primary cause of donor activity in the thermal donors. The strain induced level is also consistent with the effect of uniaxial-stress on electronic IR absorption (Stavola *et al.*, 1985).

5.4.3   Interaction with hydrogen

Thermal donors can interact with atomic hydrogen leading to the formation of TDD-H defects (Johnson and Hahn, 1986; Weber and Bohne, 1996). The kinetics of dissociation of TDD-H was studied in DLTS, where an activation barrier of 1.9 eV and 1.1 eV was derived for TDD(1) and later donors respectively (Weber and Bohne, 1996; Pearton *et al.*, 1992).
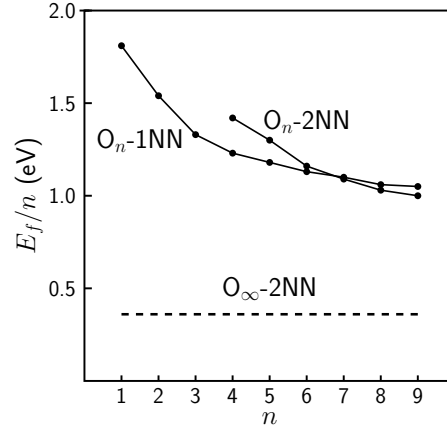
Figure 5.8: Formation energy per oxygen atom (eV), for O_n-1NN and O_n-2NN finite chains. The *driving force* to form O_n-2NN structures is its low energy core (see E_f/n for O_∞-2NN).
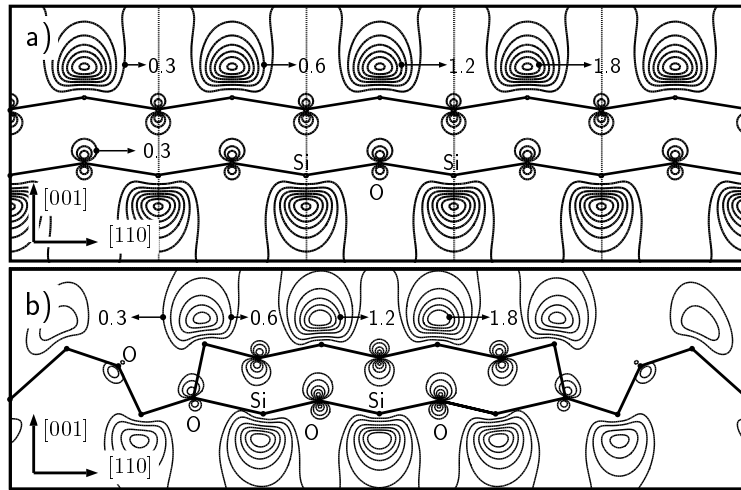
Figure 5.9: Contour plot of $|\psi_{n\mathbf{k}}(\mathbf{r})|^2 \times 1000$ for a) the lowest unoccupied band in the infinite O-2NN chain, and b) the highest occupied band in the O_9-2NN chain. For both, $\mathbf{k}$-points in the middle of the zone along (001) were taken. Contour levels are the same in both plots.

Hydrogen has also been detected by ENDOR in the shallow thermal donor (STD) family (Martynov *et al.*, 1995). However the thermal stability of the STD defects — formed at 450°C — implies a fundamental difference between TDD-H and the STD single donors.

Efficient H-attachment to the O-2NN TDD model can be attained if the topological defect is eliminated. This is done in a manner shown in Figure 5.10. Here, the coordination of all silicon, oxygen and hydrogen atoms is such so that the two electrons in the stress-induced states fall into the valence band. The binding energy of each H atom, compared when it is bond-centred and away from the chain, is 1.8 eV. This value is near the experimental observations, 1.9 eV for the first TDD members. As shown in Fig. 5.10, the H-atom is already near a Si-Si bond-centre site, and hence we expect a low capture barrier. Standard sp^3 Si-H bonds are very strong. In Si crystals these normally have 1.5 Å, with a Si-H bond energy of about 2.5 eV (Hourahine *et al.*, 1999). However, in the case of the H-(O_n-2NN)-H defects, the Si-H bond is almost 1.7Å. This is due to a complex hybridisation of the end-Si atom, still interacting with the end-O atoms (see Fig. 5.10), leading to a weaker binding energy, and hence explaining the low thermal stability of the TDD-H defects.

Although there is still no experimental evidence for the kind of structure shown in Fig.5.10, these results can be useful for experimentalists in two main aspects. (i) The stress-induced state is not removed after H-attachment — it is simply depopulated. This would suggest that TDD-H defects can act now as acceptors, with a deep electron trap at ∼0.15 eV, and possibly a second acceptor level at ∼0.07 eV. These are the donor levels observed in DLTS for the active TDD species (Henry *et al.*, 1984; Benton *et al.*, 1985). The second aspect is (ii) that the longer Si-H bonds in the O_nH_2-2NN defects imply than any Si-H related stretch vibrational mode should fall below the usual 2000 cm^{-1} region. Further work on this issue is required.

5.4.4 TDD family members

We can now identify the donors with different oxygen chains. The chains with odd number of oxygen atoms have C_{2v} symmetry but ones with even numbers have C_{2h} symmetry. The
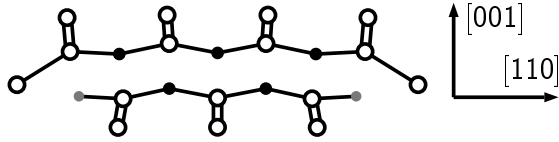
Figure 5.10: Structure for the hydrogenated O_5-2NN defect. Silicon, oxygen and hydrogen are shown in white, black and gray circles. Note that all Si, O and H atoms are four-fold, two-fold and mono-coordinated respectively.

vibrational modes of O_2 and O_3 have been identified and these species are not thermal donors (Murin and Markevich, 1996). TDD(0) may be identified with a chain of perhaps four or five O atoms suggesting TDD(N) is O_n with $n = N + 4$ or $N + 5$ (Jones *et al.*, 2001). This agrees with observations that a loss of around 9-10 oxygen atoms per TDD from solution accompanies the formation of the average donor, taken to be TDD(5) or TDD(6) (Schroder *et al.*, 1988; Newman, 1985). We have also mentioned above that O_n-2NN chains are more stable than O_n-1NN chains for more than 6-8 O-atoms. We are not convinced by the recent suggestion that different donors are alternative conformations with the same number of O-atoms. This is because the barriers between these conformations are too low – around 0.3 eV (Lee *et al.*, 2001), and stress-alignment experiments show that the donors can be aligned with barriers comparable with single oxygen diffusion. Thus during stress alignment, the cluster appears to dissociate and subsequently reforms with a different alignment.

Recent high field EPR experiments indicate that the symmetry of all the donors, except the second, is not strictly C_{2v} although the difference appears small (Dirksen *et al.*, 1998). Furthermore, ENDOR studies (Michel *et al.*, 1989; Spaeth, 1996) indicate the presence of two shells of ^{17}O hyperfine tensors with axes around $62°$ with [001] and close to that expected from oxygen lying between neighbouring Si atoms.
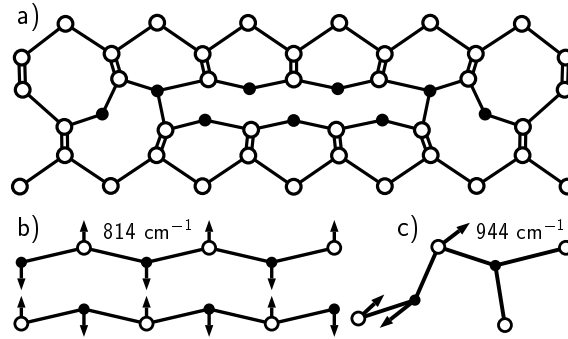
Figure 5.11: a) O_9-2NN double donor. The white and black circles denote Si and O atoms respectively. The two observed O-bands in TDD(N) at $\sim$720 and $\sim$1000 cm^{-1} in Si ($\sim$600 and $\sim$780 cm^{-1} in Ge), are assigned to chain and end oxygen modes shown in b) and c) respectively.

5.4.5 Infrared absorption spectra

Further support for the model comes from the observations and analysis of the LVMs associated with each donor. The bands related to TDD are positioned in the wavenumber regions of 945-1000, 700-730 and 575-580 cm^{-1} (Lindström and Hallberg, 1994; Murin et al., 2001). These can be seen in Figure 5.12. The 1000 and 730 cm^{-1}-bands undergo upward sequential shifts (with N) of about 10 and 4 cm^{-1} respectively, and display an oxygen origin as they shift with ^{18}O. The 580 cm^{-1}-band does not shift noticeably with N or oxygen isotopic mass. By using mixtures of ^{16}O and ^{18}O, it has been found that the upper band does not yield any new modes (spectra 3 and 4), suggesting that any oxygen atom is decoupled from any other. However, the 730 cm^{-1}-band exhibits mixed modes proving for the first time that oxygen atoms are coupled together and in close spatial proximity (Murin et al., 2001).

Similar results have also been obtained for the 600 cm^{-1}-band in Ge co-doped with ^{16}O and ^{18}O (see Fig. 5.13), i.e., an unique mixed mode at about 595 cm^{-1} is observed after HT at 370°C for 15 h. However, unlike in Si, a mixed mode appears also in the upper band region at 755 cm^{-1}, along with ^{16}O and ^{18}O modes at 780 and 742 cm^{-1}(Murin et al., 2001).
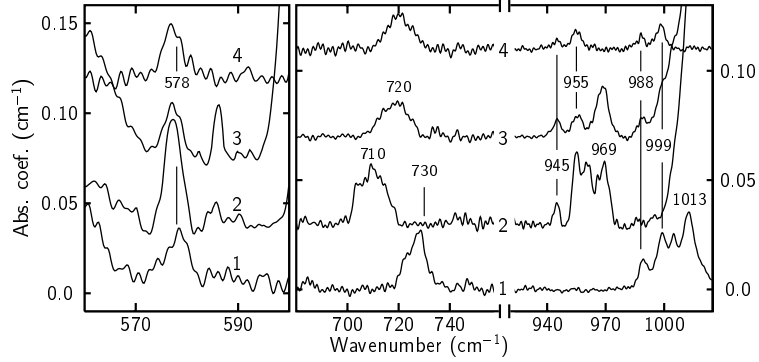
Figure 5.12: Absorption spectra measured at 300 K for Si:O samples heat-treated at 420°C for 15h: 1 - $[^{16}O_i]$=1.3×10^{18} cm^{-3}; 2 - $[^{18}O_i]$=1.5×10^{18} cm^{-3}; 3 and 4 - $[^{16}O_i]$=8×10^{17} cm^{-3}, $[^{18}O_i]$=7×10^{18} cm^{-3}. The spectrum of a non-annealed sample was used as a reference in 4. Data kindly provided by L. I. Murin.
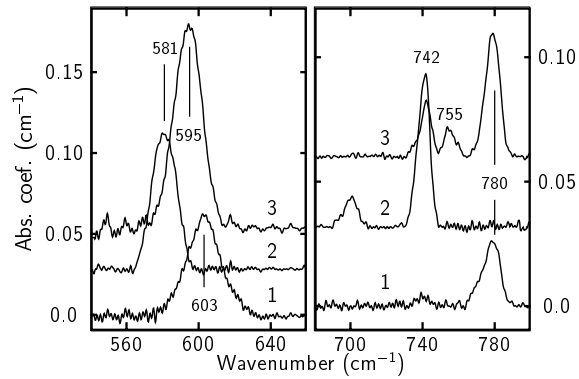
Figure 5.13: Absorption spectra measured at 300 K for Ge:O samples heat-treated at 370°C for 20 h: 1 - $[^{16}O_i]$=2.3×10^{17} cm^{-3}; 2 - $[^{18}O_i]$=3.2×10^{17} cm^{-3}; 3 - $[^{16}O_i]$=2.3×10^{17} cm^{-3}, $[^{18}O_i]$=1.7×10^{17} cm^{-3}. Data Kindly provided by V. V. Litvinov.
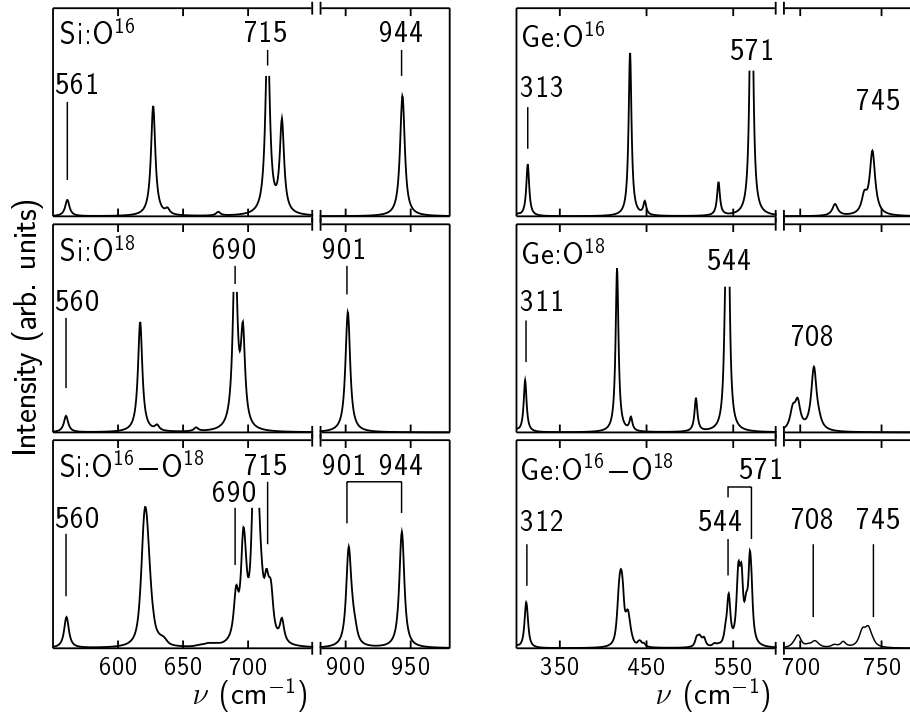
Figure 5.14: Calculated IR-intensities of the modes for O_7-2NN in Si, broadened with Lorentzian functions by 4 cm^{-1}, and evaluated as described above. ^{16}O and ^{18}O spectra are shown in a) and b) respectively, whereas the 2^7 combinations for a 50-50 ^{16}O-^{18}O mixture is depicted in c).

To understand the LVMs of the donors, we first calculate the long wavelength modes of an infinite periodic O-2NN chain. The two IR-active modes lie at 564 and 814 cm^{-1} in Si and 323, 625 cm^{-1} in Ge. The 814 cm^{-1} is shown in Fig. 5.11(b) and clearly induces a dipole moment along [001]. The 564 cm^{-1} mode involves very little movement of oxygen atoms, and is localised to the Si atoms above and below the core whose bonds are compressed by the [001] stress. This has a dipole moment along [1$\bar{1}$0], and orthogonal to the chain. Thus the simple periodic chain model explains why only a few oxygen modes can be detected in each donor, as only transverse long wavelength modes are IR-active.

We now consider the oxygen related modes arising from the ends of the chain (Fig. 5.11(c)). The highest frequency modes, evaluated from the dynamical matrices of the end-O atoms,

Table 5.3: Observed and calculated high frequency ^{16}O modes (cm^{-1}), of TDD(N) and O$_{N+4}$-2NN respectively.

N	1	2	3	4
Calc.	940	951	963	969
Obs.	975	988	999	1006

are given in Table 5.3. There is a 11:12:6 cm^{-1} increase with N in excellent agreement with the observed increases of 13:11:7 cm^{-1} for TDD(1), TDD(2), TDD(3) and TDD(4). For Ge, the calculated increments are 9:8:7 cm^{-1} compared with 5:4:3 cm^{-1} observed for TDD(1), TDD(2), TDD(3) and TDD(4). Thus the model accounts for the shift in the high frequency mode with N.

We turn now to the effect of a 50-50 mixture of ^{16}O and ^{18}O. We consider O$_7$-2NN and plot in Fig. 5.14 the calculated relative intensities of the local modes. We note that the end-mode at 944 cm^{-1} does not split in agreement with the data. This is because the displacement of the atoms shown in Fig. 5.11(c) is localised to the end O-1NN atom. However, in contrast with this, the mode around 715 cm^{-1} due to the O-2NN core splits in the mixed case (Fig 5.14), again in agreement with the data. This reflects its chain origin illustrated in Fig. 5.11(b). The chain related 560 cm^{-1} Si mode is quite insensitive to O-substitution consistent with an assignment to the observed 580 cm^{-1}band. It is also important to note that the calculated $^{16}\nu/^{18}\nu$ ratios for the 715 and 944 cm^{-1}-modes are 1.036 and 1.046, in good agreement with the observations. Fig. 5.14 also shows that other modes around 726 and 627 cm^{-1} in Si are expected to be IR-active but have not yet been detected.

In the case of Ge, both the end-mode at 745 cm^{-1} and the chain mode at 571 cm^{-1} (^{16}O) are, however, split in the mixed isotopic case, again in agreement with the data. The different behaviour of the end-mode from that in Si is striking and originates from the the closeness in the Ge-O-Ge angles at the ends and middle of the chain when compared with Si. This can be compared with the $\sim$140° Ge-O-Ge and $\sim$160° Si-O-Si angles for

interstitial oxygen (Coutinho *et al.*, 2000*b*). In Ge, two superimposed modes at $\sim$745 cm^{-1} are IR-active. The stronger mode behaves as in silicon — with no mixed modes, but the weaker mode gives rise to mixed bands. Hence, the integrated absorption of the mixed bands is considerably smaller than twice of the ^{16}O- and ^{18}O-bands.

5.4.6 Stress-energy tensor

The compressive stresses exerted by the O-2NN core and O-1NN ends are different. The former lies along [001] and the latter along [111] and [$\bar{1}\bar{1}1$]. Thus the [001] displacement of Si along the chains is different for the two regions. Table 5.4 shows that the central Si atoms exert a very large compressive strain which decreases with the length of the chain. This has implications for the stress-energy or piezospectroscopic tensors for the donors. Table 5.4 shows that the calculated tensors for the smaller C_{2v} chains possess principal values very close to those observed by electronic infra-red and EPR experiments. Note that O$_6$-NN has C_{2h} symmetry, and hence two principal directions of the tensor are rotated by $\theta = 9°$ from the [001] and [110] crystallographic axes. It is unclear whether this angle lies inside the experimental error for the tensors of those donors displaying lower symmetry than C_{2v} (Dirksen *et al.*, 1998). However, the calculations correctly reproduce the principal values of the stress tensor and their variation with donor species. We note that the decreasing [001] strain with increasing N would result in shallower strain induced states consistent with the decreasing donor level.

5.5 Summary

In conclusion, we have shown that oxygen atoms lying in chains diffuse quickly and form extended chains lying along [110]. The most stable long chains involve O atoms linking second neighbouring Si atoms (O-2NN). The chains are less stable than an SiO$_2$ precipitate but form through their rapid kinetics. The activation energy for the kick-out of a single Si interstitial appears to be considerable and will not occur during the early-stages at 450°C. The chains give rise to a compressive stress along the [001], leading to a stress induced

Table 5.4: Calculated [001] displacements (Å), $\delta_c(001)$ and $\delta_e(001)$, of central and end Si-atoms, and stress-energy tensor elements B along [001] and [110] (eV), for O_n-2NN chains. Observed tensors for the early TDD members were measured by FTIR spectroscopy and EPR (starred values) (Trombetta *et al.*, 1997; Watkins, 1996).

Calc.	O_5-2NN C_{2v}	O_6-2NN C_{2h}	O_7-2NN C_{2v}	O_∞-2NN
$\delta_c(001)$	0.43	0.42	0.41	0.34
$\delta_e(001)$	0.22	0.22	0.22	–
B_{001}	−13.8	−13.2	−12.1	–
B_{110}	10.5	9.9	8.3	–
Obs.	TDD(2)	TDD(3)	TDD(4)	
B_{001}	−12.2	−11.9	−11.4	
B_{110}		10.3*	8.5*	

empty gap level lying below the conduction-band, whose effective-mass wavefunction is localised on ~ 1000 surrounding Si atoms. The ends of the finite chain are terminated by O-1NN atoms. The donor activity arises from a pair of over-coordinated O-atoms at the interfaces between two species of oxygen in the chain. The energy levels of these regions lie above the stress induced gap level and electrons preferentially occupy the latter.

The two types of oxygen lead to different stress distributions. The core region is highly compressive along [001] while the end region leads to stress along the chain. The magnitudes of the calculated stress-energy tensor are consistent with experimental values. The same model also accounts for the vibrational modes of the donors (Murin *et al.*, 2001).

It is to be noted that the model suggests that single donors can be formed by substitution of O or Si by group-III or group-V impurities. Other possibilities include substitution of O by a tri-valent complex as a C-H unit. The former probably leads to the NL10(Al) family (Gregorkiewicz *et al.*, 1987; Ammerlaan *et al.*, 1996) and the later to the H-related shallow thermal donors (Ewels *et al.*, 1996*a*).

The vibrational spectra have been calculated for a model of the thermal donor consisting of O atoms arranged in a periodic chain. The high and low frequency bands of each donor are assigned to modes of the end-atoms and to IR-active long wavelength bands of the chain respectively. The observations of only a few O-related bands is accounted for even though each donor contains many O atoms. The great disparity in Si-O-Si bond angles between the core and end atoms explains why these atoms are not coupled in Si. This is not the case in Ge. The model also accounts for the shift in the bands with increasing N and gives two additional modes for small O chains which have not yet been observed.

Chapter 6

Shallow thermal donors with hydrogen

6.1 Introduction

Low temperature e-irradiation of Si generates mobile Si interstitials which are readily trapped by substitutional carbon defects forming carbon interstitials (C_i) (Watkins and Brower, 1976). In turn, these are mobile at room temperature and subsequently complex with many impurities including oxygen. The interstitial carbon-oxygen centre (C_iO_i), is a product of the latter interaction and is a stable defect with an annealing temperature around 350-450°C. It has been detected by all four principal methods used to characterise defects. Electron paramagnetic resonance (EPR) experiments relate the G15 signal to $C_iO_i{}^+$. The similarity of its magnetic properties with that of the carbon interstitial implies that the C-atom is only slightly affected by oxygen which is assumed to be bonded to remote Si atoms such as Si_2 and Si_3 shown in Figure 6.1(a) (Trombetta and Watkins, 1987, 1988).

The defect gives a prominent 0.7896 eV photoluminescent (PL) signal (C-band) (Yukhnevich $et\ al.$, 1966), associated with several local mode replicas (Kurner $et\ al.$, 1989; Lightowlers and Safonov, 1997). Previous Fourier transform infra-red (FTIR) spectroscopic experi-
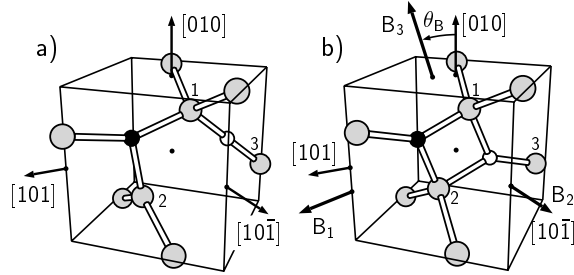
Figure 6.1: Models for C_iO_i.(a) Divalent oxygen model, (b) Trivalent oxygen model. Gray, black, white atoms are Si, C, O. Crystallographic axes and principal directions of the B tensor are also shown.

ments have identified local vibrational modes (LVMs) at 1116, 865, 742, 550 and 529.8 cm^{-1}, the highest of which is carbon and not oxygen related (Davies *et al.*, 1986). Finally, deep level transient spectroscopy (DLTS) has linked a donor level at $E_v + 0.38$ eV with the defect (Mooney *et al.*, 1977).

Earlier theoretical modelling had found that the oxygen atom was strongly affected by carbon and was not divalent as in Fig. 6.1(a), but rather, was bonded to three Si atoms as illustrated in Fig. 6.1(b) (Jones and Öberg, 1992; Snyder *et al.*, 1996). This is because the greater electronegativity of carbon encouraged electron transfer from the Si$_2$ atom with the dangling bond shown in Fig. 6.1(a). This leaves the dangling bond orbital empty and leads to a dative bond with a lone pair orbital on oxygen. Thus the oxygen atom is trivalent. Over-coordinated oxygen atoms are currently of interest because of their possible role in thermal donor defects (Jones, 1996).

The main evidence in support of this model lay in the lack of any mode around 1136 cm^{-1} related to bond-centred interstitial oxygen (O$_i$). Here we present further support to the model and demonstrate that its calculated donor level and stress-energy, or piezospectroscopic, tensor are in agreement with the observations.

Further interest in the defect has recently arisen from the observation of a marked reduction in its concentration in irradiated samples into which hydrogen had been introduced by wet-etching (Feklisova and Yarykin, 1997; Feklisova *et al.*, 1999). These studies suggested

that the C_iO_i defect can trap up to two hydrogen atoms and that the single hydrogenated centre possessed a deep hole trap H4 at $E_v + 0.28$ eV (Feklisova *et al.*, 1999). This hole trap was recently reassigned to the VOH defect (Feklisova *et al.*, 2001)

In view of these developments, we have investigated the interaction of the defect with hydrogen paying attention to its electrical properties. It is clear that the defect with two H atoms is inert but a single H atom results in a bi-stable defect with intriguing properties. In one form it behaves as a deep acceptor but in another configuration, it is a shallow donor. The calculated configuration energy curves for the defect are strikingly similar to a hydrogen related radiation-induced shallow donor labelled D1. Moreover, the calculated oxygen related vibrational mode and its anomalous upward shift with hydrogen are close to the values observed for D1.

This defect appears to be the first of a family of shallow single donors which are successively produced on annealing *e*-irradiated Czochralski-grown Si (Cz-Si) into which hydrogen had been introduced (Markevich *et al.*, 1994). The first two members D1 and D2 are formed around 350°C and 450°C respectively and have $(0/+)$ levels at $E_c - 42.6$ meV and $E_c - 37.0$ meV which are comparable with phosphorus ($E_c - 45.6$ meV). The defects possess a Rydberg series of excited states, and the effective-mass IR transitions for D2 and D3, are identical with those of the shallow thermal donors STD(H)2 and STD(H)3 found by annealing O-rich Si containing hydrogen (Newman *et al.*, 1996, 1998). The STD(H)N family members are known to contain hydrogen as their electronic transitions shift in deuterated material. However, the STD defects are formed in annealed Cz-Si without prior irradiation and they have been suggested to be responsible for the NL10(H) family of shallow single thermal donors (Newman *et al.*, 1996). It has also been proposed that these centres contain, in addition to hydrogen, interstitial carbon and oxygen (Ewels *et al.*, 1996*a*,*b*). However, there is no spectroscopic evidence for these impurities in the DN and STD(H)N families. Nevertheless, weak [17]O-hyperfine satellites have been found in NL10 shallow donors in Al doped samples (Gregorkiewicz *et al.*, 1987, 1988).

A considerable body of information about D1 has been found by electrical, photo-electrical, optical and magnetic experiments (Markevich *et al.*, 1994, 1998*a*, 1995, 1997*b*,*a*, 1998*b*).
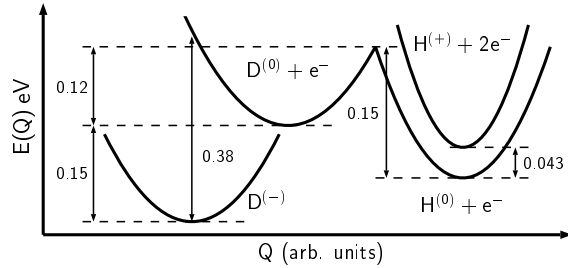
Figure 6.2: Configuration coordinate diagram for D1 according to Markevich *et al* (Markevich *et al.*, 1997*b*). Quoted energies are based on electrical, optical and capacitance measurements.

Thus it is known that the defect is bi-stable, assuming the H-form in the positive and neutral charge states and the D-form in the negative charge state. A metastable neutral D-form (originally labelled X), also exists. Hall effect and conductivity studies show that the defect has a negative-U with an occupation level (the average of the donor and acceptor levels) at $E_c - 0.076$ eV. Electronic IR absorption studies show a donor level lying 43 meV below the conduction band and this then places the acceptor level, or the difference between D$^-$ and H^0, at $E_c - 0.11$ eV. DLTS and optical absorption studies were used to determine the other energies in the configuration coordinate diagram shown in Fig. 6.2.

The D-form of D1 has also been correlated with a local vibrational mode at 1025.5 cm^{-1} that shifts *upwards* to 1027.9 cm^{-1} with deuterium, demonstrating that this defect contains H (Markevich *et al.*, 1998*b*). This unusual shift has not been explained previously but here we link it to an anti-crossing with an unobserved carbon-hydrogen wag mode. No vibrational modes have been found for the H-form.

The neutral H-form of D1 has also been associated with an EPR centre labelled TU1 detected under illumination conditions (Markevich *et al.*, 1997*a*). Its isotropic *g*-tensor probably arises from the delocalised spin-density which does not reflect the true symmetry of the defect. One ^{29}Si hyperfine satellite has been resolved having an isotropic interaction of about 60 MHz. Comparing this with the isotropic hyperfine interaction of 4594 MHz arising from a free ^{29}Si atom (Morton and Preston, 1977), gives 1.3% of the spin-density

162

located on this unique atom. Hyperfine interactions with hydrogen were recently observed for D1 and D2 by using electron-nuclear double resonance (ENDOR) spectroscopy (Langhanki *et al.*, 2001). One principal axis of the hyperfine tensor is nearly parallel to the $\langle 110 \rangle$ direction suggesting a H bond lying along this direction. The isotropic part of the hyperfine tensor corresponds to a minute spin-density on H of $6 \times 10^{-3}\%$. Similar densities and hyperfine tensors were measured for the NL10(H) defects (Ammerlaan *et al.*, 1996), strengthening the link between the STD(H)N, NL10(H), and DN families.

It has been suggested that D1 is a complex of hydrogen with an oxygen-related radiation induced defect like VO or C_iO_i(Markevich *et al.*, 1994). However, VOH is an acceptor with a level at $E_c - 0.31$ eV (Svensson *et al.*, 1989; Artacho and Ynd100uráin, 1989; Nielsen *et al.*, 1999; Peaker *et al.*, 1999), while VOH$_2$ is passive (Markevich *et al.*, 2000). We show that D1 has many properties in common with C_iO_iH. This in turn suggests that the shallow thermal donors STD(H)N also contain interstitial carbon. It is known that interstitial carbon can be produced as a by-product of oxygen aggregation in annealed Cz-Si and does not require irradiation for its formation. This follows as annealing Cz-Si to about 450°C produces a set of prominent photoluminescent lines. One of these is the T-line at 0.935 eV which is known to be a complex involving interstitial carbon bonded to hydrogen and is stable up to $\sim$600°C (Safonov *et al.*, 1996). This thermal stability is comparable with the STD(H)N family which disappear around 550°C (Newman *et al.*, 1998).

6.2 The interstitial carbon-oxygen defect

6.2.1 Infra-red absorption spectrum

Table 6.2 gives the LVM-frequencies and their ^{13}C and ^{18}O isotopic shifts assigned to the C_iO_i defect Davies *et al.* (1986); Coutinho *et al.* (2001a). In descending frequency, they will be labelled as the 1116, 865, 742, 585, 550, 540 and 529 cm^{-1}-bands respectively. The most important result is the observation of a significant 33.4 cm^{-1} oxygen isotopic

shift *only* for the 742 cm^{-1}-band, clearly indicating its oxygen character. This shift is in agreement with observations based on PL vibrational spectroscopy which only detects A_1 modes (Kurner *et al.*, 1989; Lightowlers and Safonov, 1997; Davies and Newman, 1994). Table 6.2 then clearly shows that the highest oxygen related frequency lies at 742 cm^{-1}, compared with 1136 cm^{-1} for O_i, and possesses an ^{18}O shift considerably smaller than that of the asymmetric stretch mode in O_i (51.4 cm^{-1}) (Pajot *et al.*, 1995), where the O atom bridges neighbouring Si atoms.

The 585 and 540 cm^{-1}-bands were recently identified with the C_iO_i complex (Coutinho *et al.*, 2001*a*). All the bands in Table 6.2 anneal out between 300-400°C along with bands related to VO. Simultaneously, there is a strong increase in the intensities of lines related to C_sO_i. Evidently, the annealing behaviour of two dominant defects, C_iO_i and VO, are closely related. Either vacancies, generated upon A-centre dissociation, are trapped by C_iO_i, or C_i atoms liberated from C_iO_i interact with VO. In both cases C_sO_i is formed.

6.2.2 Structure and energetics

In agreement with previous calculations (Jones and Öberg, 1992), we find the ground state structure of C_iO_i, is one where both carbon and oxygen are three-fold coordinated and form two vertices of a ring as shown in Figure 6.1(b). The structure where the O atom lies at the centre of the dilated Si-Si bond, shown in Fig. 6.1(a), relaxes spontaneously to the ring defect for both the neutral and positively charged centre. The binding energy between C_i and O_i is 1.7 eV and this large value is consistent with the high thermal stability of the defect.

6.2.3 Electrical activity

Table 6.1 shows that $E(0) - E(+)$ for C_iO_i lies 0.08 eV above that for C_i. Therefore a deep donor level is estimated at $E_v + 0.36$ eV in agreement with the observed DLTS level at $E_v + 0.38$ eV (Mooney *et al.*, 1977). No acceptor or second donor levels were found. A Mulliken bond population analysis gives 25.4% and 0.1% of spin-density localised around

Table 6.1: Formation energies E_f, $E(-/0)$, $E(0/+)$, and acceptor $(-/0)$ and donor $(0/+)$ levels of O_i, C_i, C_iO_i, C_iO_iH and $C_iO_{2i}H$ defects (eV). C_iO_iH and $C_iO_{2i}H$ defects have forms R and O. Values are calculated using Gaussian s, p-orbitals with 1 set of Gaussian functions at bond-centre sites (4 orbitals), and bracketed values are runs with 2 Gaussians (8 orbitals). E_f was calculated by taking chemical potentials of Si, O, C and H from silicon, α-quartz, diamond, and molecular H_2 environments respectively. The last two columns are estimates of acceptor and donor levels relative to the band edges found as described in the text.

	E_f	$E(-/0)$	$E(0/+)$	$E_c - (-/0)$	$(0/+) - E_v$
O_i	1.809				
	(1.817)				
C_i	4.122	7.073	6.666		
	(4.056)	(6.963)	(6.603)		
C_iO_i	4.212		6.750		0.364
	(4.107)		(6.731)		(0.408)
C_iO_iH-(R)	3.309		7.506		1.120
	(3.281)		(7.416)		(1.093)
C_iO_iH-(O)	3.475	6.908		0.265	
	(3.331)	(6.865)		(0.198)	
$C_iO_{2i}H$-(R)	3.923		7.547		1.161
	(3.858)		(7.419)		(1.096)
$C_iO_{2i}H$-(O)	4.479	6.859		0.314	
	(4.308)	(6.798)		(0.265)	

the carbon and oxygen atoms respectively. The first is in agreement with the 28.6% spin localisation on carbon measured for G15 (Trombetta and Watkins, 1987). In addition, the four Si atoms bonded to Si_1 and Si_2 in Figure 6.1(b) share about 15% of the unpaired spin-density. The presence of oxygen rotates the Si_2-C bond through 22° away from the [010] axis. This is in excellent agreement with the angle of $\theta_A = 20° \pm 5°$ that two of the principal directions of the ^{13}C-hyperfine tensor make with the crystallographic axes (Trombetta and Watkins, 1987).

6.2.4 Stress-energy tensor

The principal directions of the calculated stress-energy tensor are shown in Figure 6.1(b). The C_{1h} symmetry of the defect implies that one principal direction (corresponding to the B_2 component) lies along $[10\bar{1}]$ but the other directions are rotated from the [010] and the [101] axes. For the positively charged defect, the rotation angle is calculated to be $\theta_B = 22°$, and the principal values of the tensor are 8.5, 2.3 and -11.8 eV for B_1, B_2 and B_3 respectively. The angle arises from the perturbation to the structure caused by the oxygen atom as it vanishes for the C_i defect. Stress alignment experiments give the measured values of B_1, B_2 and B_3 for G15 to be 8.6, 0.2 and -8.8 eV and $\theta_B = 15°$, and thus the model accounts well the observations.

6.2.5 Local vibrational modes

The LVMs for the neutral defect are shown in Table 6.2. Of special interest are the oxygen related modes. The highest of these lies at 760 cm^{-1} – well below the asymmetric stretch mode for interstitial oxygen at 1136 cm^{-1}. This is a characteristic of the weakened bonds of over-coordinated oxygen relative to those in Si-O-Si. The oxygen mode is very close to the observed band at 742.8 cm^{-1}. The observed and calculated ^{18}O-shifts are also very close, lying at 33.4 and 35.6 cm^{-1} respectively. Two carbon related modes are calculated to lie at 1138 and 876 cm^{-1}, close to the observed 1116 and 865 cm^{-1}-bands. Their shift with ^{13}C demonstrates that they are carbon related in agreement with the observations.

Table 6.2: Observed and Calculated Local Vibrational Modes (cm^{-1}), for C$_i$O$_i{}^0$. First three columns report absolute frequencies, whereas columns four onwards give their downward isotopic shifts.

| ^{16}O, ^{12}C | | ^{16}O, ^{13}C | | ^{18}O, ^{12}C | | ^{18}O, ^{13}C | |
Obs.	Calc.	Obs.	Calc.	Obs.	Calc.	Obs.	Calc.
1116.3	1137.6	36.4	37.7	1.0	1.0		38.8
865.9	876.1	23.9	24.5	0.15	0.1		24.6
742.8	759.6	0.5	0.3	33.4	35.6		35.8
~588	593.4	—	0.1	~3	3.2		3.3
549.8	555.8	0.2	0.3	0.3	0.2		0.5
~542	544.7	~0.5	0.1	~1.5	0.5		0.5
529.6	544.2	0.1	0.0	5.2	5.4		5.5

The four remaining low frequency modes at 593, 556, 545 and 544 cm^{-1} have not been assigned previously. They arise from vibrations of Si neighbours to the defect core, and are properly described only when energy second derivatives with these atoms are calculated directly from the *ab-initio* program. In this sense they are similar to the lattice-induced band at 517 cm^{-1} due to interstitial oxygen (Coutinho *et al.*, 2000*b*). These modes display very small isotopic shifts upon C or O substitution. Frequencies and isotopic shifts of the 544 and 545 cm^{-1}-modes agree well with those of the measured 529 and 540 cm^{-1}-bands, supporting the assignment of the later to C$_i$O$_i$ (see Subsection 6.2.1). However, the symmetry of the 556 and 544 cm^{-1} modes is B and in conflict with the claim that only A modes are detected as phonon replicas. According to group theory, this is not actually the case for a C_{1h} defect although then the dipole matrix element must involve components parallel and perpendicular to the mirror plane (or vice-versa) for the zero phonon line and replica respectively.

In summary, the agreement between the calculated and observed modes, their isotopic shifts, the energy level and stress-tensor, give convincing evidence for the ring structure

Table 6.3: Relative energies (eV) for five C_iO_iH structures differing in the attachment of hydrogen. R (ring) and O (open) core structures where considered. X-H represent structures where the H atom is bonded to X, where X can be C, Si_1, Si_2, or the O atom in Figure 6.1(b). NS stand for Not Stable.

Core	R			O		
Charge state	+	0	−	+	0	−
C-H	0.00	0.00	NS	NS	0.17	0.00
Si_1-H	NS	NS	NS	NS	NS	NS
Si_2-H	NS	NS	NS	1.67	0.89	0.53
O-H	2.93	2.89	2.32	NS	NS	NS

of C_iO_i.

6.3 Hydrogenation of C_iO_i and the STD defects

It is well established that hydrogen interacts effectively with both deep and shallow centres, displacing or eliminating their energy levels in the gap. Moreover, dangling bonds are particularly attractive sites for H-attack (Pearton *et al.*, 1992; Coomer *et al.*, 2000; Lightowlers *et al.*, 1994).

6.3.1 C_iO_iH as a precursor for STD(H)

The C_iO_i defect, in the neutral or positive charge states, possesses one fully or partially occupied *p*-like dangling orbital centred on the carbon atom. This is a likely place for H attachment as the carbon atom is then saturated leaving the electrical activity confined to the Si_2 dangling bond. If this is empty, as in the positively charge defect, then a ring structure involving oxygen is likely to form in the same way as in C_iO_i. However, in the neutral or negative centre, an anti-bonding orbital will be occupied and we expect that

the ring will break. This would leave an occupied dangling bond orbital on the Si radical near an oxygen atom in its normal interstitial bond centred configuration. We call the ring structure the R-form and the open configuration, the O-form. However, there are several other possible sites for H attachment. It could bond with silicon atoms Si_1 and Si_2 in Figure 6.1(b), or with the oxygen atom. The relative energies when H is in all these structures are given in Table 6.3 for the positive, neutral and negative charge states. Our conclusion is that H prefers to bond with carbon in all cases. However, as expected, the structure depends on the charge state with the R-form lowest in energy for the positive and neutral defects and the O-form in the negative centre.

In Fig. 6.3, a configuration diagram is shown for the defect (Coutinho et $al.$, 2001a). Here, quoted values correspond to the results of the calculations, and the parabolic shapes are only schematic. In the neutral defect, the R-form has the lowest energy while the O-form is metastable by 0.17 eV. By carefully mapping the energy surface linking the two structures, we find $\sim$0.10 and $\sim$0.27 eV barriers for O$\rightarrow$R and R$\rightarrow$O paths respectively. In the positive charge state, the ring form is again stable but the O-form is now unstable and relaxes spontaneously to R.

In the negative charge state, however, the Si_2 dangling bond is occupied with two electrons and a dative bond with oxygen cannot occur. Thus the ring form is unstable and spontaneously relaxes to the O-form. Consequently the defect is bi-stable taking the O-form in the negative state and the R-form in the positive case.

The dissociation energy of the R-form into C_iH and O_i defects was estimated to be 1.4 eV. Once this dissociation has occurred, it is expected that the defects would be lost as previous theory has indicated that C_iH diffuses faster than C_i(Leary et $al.$, 1998). The dissociation path involving the release of H is unlikely to occur. This is because the binding energies of H with the C_iO_i centre are found to be about 2.5 eV. These were calculated by moving H^- or $H^{(0)/(+)}$ from the defect and placing it at an interstitial T or BC sites respectively.

We now consider the energy levels of the defect. These were calculated for the R and O-forms separately, as these are the ground states for the positive and negative charge states respectively (see Table 6.3). The difference in energies of O^- and O^0 when compared with

169
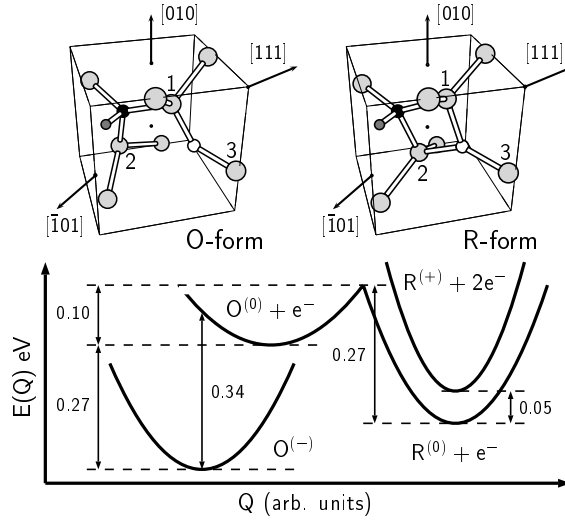
Figure 6.3: Configuration coordinate diagram for C_iO_iH. Atomic structures for O and R-forms are also shown. Gray, black, and white atoms are Si, C, and O respectively. The small gray atom bonded to carbon is H. Quoted values were calculated by the total energy method.

C_i^- and C_i^0 shows that the $(-/0)$ level lies at $E_c - 0.27$ eV. This is not the thermodynamic level as the neutral O-form is metastable with respect to the R-form. Nevertheless, it can be compared with the 0.15 eV emission barrier measured for D1 in the D-form (see Figure 6.2). In the R-form, the $(0/+)$ level lies at $E_c - 0.05$ eV. This demonstrates that the defect is a shallow donor in one form and a deep acceptor in the other. Using the 0.17 eV difference in energies of the two neutral forms, yields the thermodynamic $(-/0)$ level at $E_c - 0.1$ eV in excellent agreement with the $(-/0)$ level at $E_c - 0.11$ eV for the D1 centre described in the introduction.

These results are summarised in Figure 6.3. If the charge state of O^- configuration is changed to become neutral, the energy drops 0.06 eV upon relaxation. The barrier for $R^0 \rightarrow O^0$ is about 0.27 eV while R^0 is 0.17 eV more stable than O^0. The inverted order of energy levels implies that $U = E(-/0) - E(0/+) = -0.05$ eV is negative.

The bi-stability properties and electronic levels for C_iO_iH shown in Fig. 6.3, and those for the D1 defect shown in Fig. 6.2 are strikingly similar. Thus we identify the R and O-forms

170

with the experimentally labelled H and D-forms respectively. The experimental $(-/0)$, $(0/+)$ levels and $H^0 \rightarrow D^0$ barrier energies are 0.11, 0.0426, and 0.15 eV respectively.

The C_iO_iH complex has two paramagnetic states, with the R^0 form more stable, and therefore, we investigated the character of the spin-density by analysing the Mulliken populations of the highest occupied band of the neutral defects.

In the R-form, the Mulliken bond populations show only $\sim$0.5% and $\sim$0.1% of the spin-density lying on C and H, and none on the oxygen atom. The vanishing spin-density on oxygen is striking and unexpected as the over-coordinated oxygen atom is the source of donor activity. We interpret this result in the following way. The anisotropic defect creates a compressive stress along the C-Si$_2$ bond which is rotated by 22° away from [010]. This stress will split the six conduction band valleys along cube directions, lowering the energy of the pair along [010] (the alignment of C-Si$_2$ in Fig. 6.3) relative to the other two pairs (Ramdas and Rodriguez, 1981). Figure 6.4 shows the band structure for the Si crystal folded into the 64 atom cell. The conduction band minima for Si lie near the folded X-points at $\pm\frac{2\pi}{a_0}\langle\frac{1}{4}00\rangle$. However, in the case when the defect occupies the unit cell, Fig 6.4 shows that the band close to the conduction band minima near $\pm\frac{2\pi}{a_0}(0\frac{1}{4}0)$ is now pushed downward into the gap which we suggest is due to the compressive stress of the defect along (010). This strain leads to an effective-mass gap level localised on Si atoms and this explains why the resulting state has so little amplitude on C, H and O. In essence, the potential giving rise to the gap state is due to stress and not the chemical identity of the atoms making up the defect.

The partial occupation of the strain induced gap level is however dependent on the presence of these impurities. The C atom is fully saturated and cannot lead to any donor activity. Consider now the trivalent oxygen atom. One of the electrons in the lone pair on oxygen forms a bond with the Si$_2$ radical, leaving a single electron in an anti-bonding level. If this level lies *above* the gap state arising from the compressive stress of the defect, then the donor electron would drop into the stress induced defect level and lose its oxygen parentage. In this way, the lack of spin-density on oxygen is explained. The explanation is similar to the origin and behaviour of the double donor activity of the NL8 TDD(N)
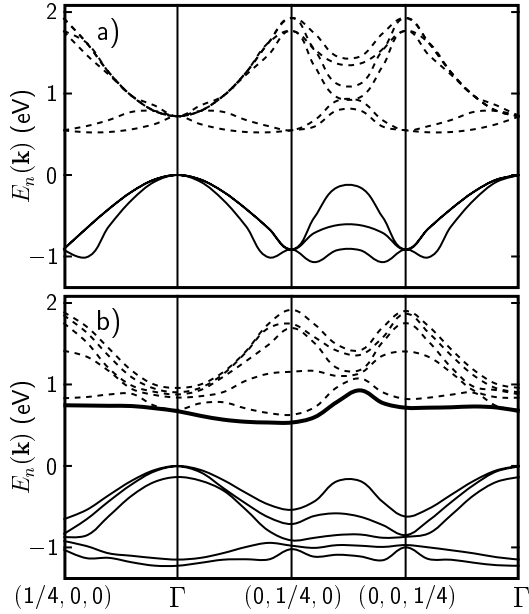
Figure 6.4: One-electron band structure for bulk Si (a), and the R-form of the neutral C_iO_iH defect (b) folded in 64 Si-atom supercells. All **k** vectors are in $2\pi/a_0$ units, where $a_0 = 5.390$ Å is the calculated Si lattice parameter. Alignment of the defect is as shown in Fig. 6.3. Solid and dashed lines represent filled and empty bands, where the highest half-filled band is emphasised as a thick branch in (b).

defect (Jones *et al.*, 2001).

In the neutral O-form, 30% of the spin-density lies on the Si_2 radical. The wavefunction is composed of 15% s and 85% p (approximately parallel to [101]) respectively. Smaller spin-densities of about 3-4% lie on both Si atoms bound to Si_2 on the left hand side of Figure 6.3. Again, little spin-density is found on carbon or oxygen. Finally, we note that in both forms the C-H bond is aligned along $\langle 110 \rangle$ — the same direction as the H-hyperfine interaction in D1.

We now turn to the local vibrational modes of the R and O forms given in Table 6.4. The first three rows give the modes localised mainly on C-H, C and O respectively. One of the most noticeable features is that the oxygen related mode is very sensitive to its bonding. In the ring structure (R-form) its LVM lies around 720 cm^{-1} but this increases to 1010 cm^{-1}

for the O-form where it assumes its normal bond centred location. The C-H stretch mode lies around 2700 cm^{-1} while two wag-modes are found around 1000 cm^{-1} and are split by about 80-100 cm^{-1}. Two carbon related modes lie around 800 and 900 cm^{-1}, although these differ in the two forms, and four other less localised modes lie close to the Raman edge.

Calculations of ^{18}O and ^{12}C related isotopic shifts are shown in the second and third columns of numerical data. The oxygen related mode has shifts of 29 and 43 cm^{-1} in the R and O-forms. In the deuterated case, a complicated reordering occurs, with a change in character in some of the modes. For this reason it has not been possible to give its downward isotopic shifts and Table 6.4 reports the calculated mode with starred values.

Of great significance is the 1009.7 cm^{-1} oxygen related mode in the O-form which shifts 3.1 cm^{-1} *upwards* with deuterium. This is close to a mode observed for the D-form of D1, described in the introduction, at 1025.5 cm^{-1} which also shifts 2.4 cm^{-1} upward with deuterium. We can now understand this anomalous shift as arising from a coupling with the undetected C-H wag mode at 1027.4 cm^{-1}. In the deuterated defect, this wag mode shifts down to around 900 cm^{-1} and below the oxygen related mode and hence the attempted crossing leads to an increase in the frequency of the oxygen related mode. Oxygen related modes usually possess large effective charges while the wag and stretch modes due to C-H have not been detected presumably because of the low values of their effective charges.

In summary, the C$_i$O$_i$H defect is bi-stable with donor and acceptor levels close to the shallow thermal donor D1 defect. The thermal stability, negative-U character, and vibrational modes are consistent with an assignment to this defect which is also known to contain H.

6.3.2 Full passivation

The interaction between the C$_i$O$_i$H defect and a second H atom was also investigated. One would then expect that the two H atoms would passivate the Si and C radicals leading to an inert defect. Indeed, among several alternative structures, the lowest energy one is

Table 6.4: Local vibrational modes and their downward isotopic shifts (cm^{-1}) for the R- and O-forms of C_iO_iH $C_iO_iH_2$ and $C_iO_{2i}H$ defects in the neutral charge state. For C_iO_iH and $C_iO_{2i}H$, the first, second and third rows correspond to modes which are mainly localised on C-H, C and O atoms respectively. For $C_iO_iH_2$, the second row gives modes localised on the Si-H unit, and the third and fourth rows list O and C-related modes. The last four frequencies in all defects correspond to modes mainly localised on Si atoms. Stared values list the actual frequencies of modes of mixed character and not their isotopic shift.

Defect	^{12}C, ^{16}O, H	^{12}C, ^{18}O, H	^{13}C, ^{16}O, H	^{12}C, ^{16}O, D
	2754.4, 1072.3, 943.0	0.0, 0.3, 0.2	7.6, 8.7, 4.2	735.9, 978.5*, 782.3*
	933.3, 752.7	1.3, 5.1	22.1, 11.2	740.9*, 656.0*
C_iO_iH	719.6	28.6	7.6	−1.6
R-form	594.3, 563.3,	1.7, 4.5,	2.9, 0.6,	3.9, 0.9,
	544.6, 530.5	0.2, 1.5	0.2, 1.0	6.4, 3.0
	2767.9, 1027.4, 947.9	0.0, 2.1, 0.1	7.8, 7.1, 3.9	739.9, 924.5*, 815.4*
	881.4, 790.1	0.3, 0.1	21.0, 20.1	704.8*, 665.2*
C_iO_iH	1009.7	42.7	0.9	−3.1
O-form	639.7, 586.9,	6.4, 0.1,	0.2, 4.6,	0.1, 4.7,
	549.1, 531.8	0.0, 0.1	0.2, 0.4	4.7, 3.2
	2723.4, 1032.4, 964.1	0.0, 1.1, 0.0	7.6, 9.0, 5.1	727.7, 927.1*, 839.6*
	1982.3, 772.5, 719.3	0.0, 0.0, 0.0	0.1, 6.0, 0.1	561.3, 701.8*, 672.1*
$C_iO_iH_2$	997.9	43.3	0.2	−2.5
	878.9, 817.4	0.3, 0.1	18.3, 16.0	634.7*, 586.3*
	635.1, 588.0,	6.5, 0.1,	0.2, 3.7,	0.1, 1.5,
	560.2, 534.0	0.0, 0.1	0.8, 0.3	7.5, 3.6
	2730.5, 954.6, 943.6	0.0, 2.5, 0.9	7.6, 10.5, 13.7	729.7, 999.5*, 792.1*
	1079.9, 756.9	0.5, 1.9	10.4, 17.3	737.7*, 673.0*
$C_iO_{2i}H$	1004.1, 811.3	44.6, 33.3	0.1, 2.5	−0.1, −3.4
	670.1, 569.5	12.1, 11.6	0.5, 1.4	2.1, 1.0
	593.0, 549.0	1.6, 5.8	3.4, 0.1	4.0, 0.4

where the second hydrogen atom binds to the Si_2 radical in Figure 6.3 (O-form) on the opposite side of the oxygen atom. The alternative, where H binds to Si_2 nearby the oxygen is 0.6 eV higher in energy. There are then no donor or acceptor levels and the defect is fully passivated. The oxygen atom is bound to C_iH_2 with an energy of 1.4 eV, while the second H atom is bound with an energy of $\sim$2.5 eV.

Table 6.4 gives the LVMs for the defect. These are similar to the O-form of C_iO_iH, but there are three additional Si-H related stretch and bend modes at 1982, 773 and 719 cm^{-1}. The O-mode is now close to 1000 cm^{-1} reflecting its divalent character. The lower carbon mode at 817 cm^{-1} is pushed up by coupling with the Si-H wag modes. As for the singly hydrogenated complex, deuteration results in a cross-over and mixing of several modes. The C-H mode at 1032 cm^{-1} falls below the oxygen mode which is consequently displaced upwards from 998 to 1000 cm^{-1} in a similar manner to the C_iO_iH defect.

6.4 Further oxygen aggregation

We briefly describe the effect of adding a second oxygen atom to C_iO_iH. There are now a greater number of candidate structures but among those investigated, the ones with the additional O-atom lying in the same $(\bar{1}01)$ plane as C_iO_i are energetically favorable. Several ring (R) and open (O) structures have low formation energies and are shown in Fig. 6.5. The O' structure was proposed previously as a candidate for a H-related shallow thermal donor (Ewels *et al.*, 1996*a*,*b*).

The energies of all these forms are listed in Table 6.5. Defects in the positive, neutral and negative charge states were considered. Once again, the R-form is found to be the ground state configuration for the neutral and positively charged states, whereas the O-form is stable in the negative charge state. Forms R' and O' are metastable by $\sim$0.5 eV, with a slight preference for the asymmetric R'-form.

The electronic levels were evaluated for the R and O forms. Again, the former is a shallow donor with a calculated level at $E_c - 0.01$ eV. The O-form has a deep $(-/0)$ level at $E_c - 0.3$ eV, and the barrier for the $O^0 \rightarrow R^0$ transition is only 0.02 eV. However, the
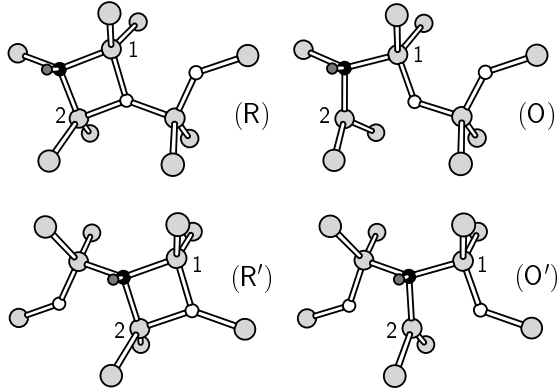
Figure 6.5: Structures for $C_iO_{2i}H$ considered in our study. Gray, black, white atoms are Si, C, O. The small gray atom is H. Relative energies are listed in Table 6.5.

Table 6.5: Relative energies (eV) for four $C_iO_{2i}H$ structures R, O, R' and O' shown in Figure 6.5. NS stand for Not Stable.

Charge state	+	0	−
R	0.00	0.00	NS
O	NS	0.56	0.00
R'	0.37	0.45	NS
O'	0.61	0.56	NS

O^0-form is now metastable by 0.56 eV compared with 0.17 eV for C_iO_iH. This shows that the thermodynamic $(-/0)$ level is now above the conduction band bottom and hence the defect can never be prepared in the negative charge state. These results are summarized in Fig. 6.6. Thus $C_iO_{2i}H$ is *not* bi-stable.

Our conclusions are then that the ring form is stabilized in $C_iO_{2i}H$ which can only be a shallow donor defect. This is consistent with an assignment to D2, and therefore to STD(H)2, as this defect is not known to be bi-stable.

The LVMs of the R^0 are given in Table 6.4. The C-H stretch mode lies around 2700 cm^{-1}, well above a series of strongly coupled C-H modes. Two O-modes appear at 1080 and
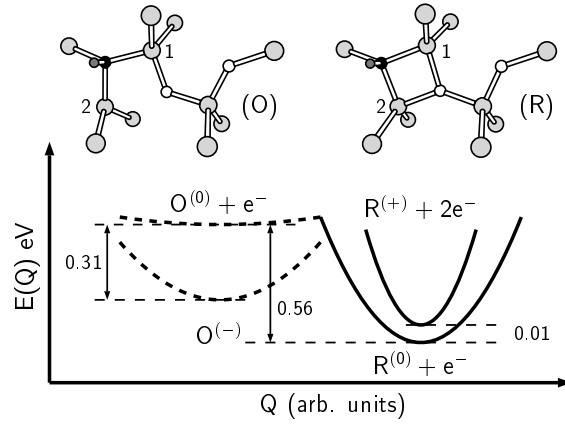
Figure 6.6: Configurational diagram for the $C_iO_{2i}H$ defect. Dashed potential curves indicate that the O-form is unstable under thermodynamic equilibrium – the $C_iO_{2i}H$ complex is a single shallow donor.

757 cm^{-1}, consistent with the presence of a divalent and trivalent oxygen. Modes around 600 cm^{-1} also shift considerably with ^{18}O substitution. These are similar to a low frequency pair also found in the interstitial oxygen dimer (Coutinho *et al.*, 2000*b*; Öberg *et al.*, 1998; Pesola *et al.*, 1999*b*).

6.5 Summary

It is found that the IR-activity from the C_iO_i defect can be divided into three sets of bands classified according to their isotopic shifts. The carbon-related 1116 and 865 cm^{-1}-bands, the oxygen 742 cm^{-1}-band, and the four low frequency 585, 550, 540, 529 cm^{-1}-bands, where the 585 and 540 cm^{-1}-bands have not been reported previously. Of particular interest is the position and ^{18}O isotopic shift observed for the 742 cm^{-1}-band (33.4 cm^{-1}), much less pronounced than that of O_i (51.4 cm^{-1}) (Pajot *et al.*, 1995). There is evidence for absorption bands with similar character related to the thermal double donors in Si. These lie at ~720 cm^{-1} and shift by ~24 cm^{-1} in ^{18}O rich samples (Lindström and Hallberg, 1994, 1996). These observations favor here a different bonding of oxygen, as an alternative to is *normal* bond-centered location.

The calculations have shown that the C_iO_i defect has a ring structure involving an over-coordinated oxygen atom. The weak oxygen bonding then leads to the highest oxygen related vibrational band lying around 720 cm^{-1} and far from the 1136 cm^{-1}-band of interstitial oxygen. This supports previous studies of the defect (Jones and Öberg, 1992; Snyder *et al.*, 1996). This mode is relatively unaffected when H is added to the defect and appears to be a signature for this type of oxygen. All seven observed band frequencies and their isotopic shifts are remarkably well described by the model. The calculated donor level and energy-stress tensor are also in good agreement with the measured values.

The defect can trap one or two H atoms and is electrically inert in the latter. The single hydrogenated center has remarkable properties. It is bi-stable, *i.e.*, the negative charge state has a divalent oxygen atom, whereas in the positively charged defect the oxygen is over-coordinated. The effective ionisation correlation term, U, is negative and a shallow donor level lies 0.05 eV above a deep acceptor.

None of the calculated levels are in agreement with an assignment to the hole trap H4 at $E_v + 0.28$ (Feklisova *et al.*, 1999). On the other hand the C_iO_iH defect has similar properties to the first species of a family of shallow donors, labelled DN, found in irradiated Si (Markevich *et al.*, 1994, 1998a, 1995, 1997b,a, 1998b). D2 and D3 have been associated with the shallow thermal donor defects STD(H)2 and STD(H)3 (Newman *et al.*, 1998; Markevich *et al.*, 1998a). The energy levels, the oxygen related vibrational mode and its shift with hydrogen are all consistent with an assignment of C_iO_iH and $C_iO_{2i}H$ with D1 and D2 respectively. The negligible spin-densities on C, H and O and the alignment of the C-H bond along [$\bar{1}$01] are consistent with ENDOR results. However, to our knowledge, no DN defects have been detected in H-plasma or wet chemical etched and irradiated Cz-Si samples. Moreover, the presence of carbon and oxygen in the defects remains to be verified by a spectroscopic technique. According to the calculations, the ground state for the effective-mass R^0 defect is localized on a strain induced gap level mainly localized on Si atoms. The donor character originates from the over-coordinated oxygen atom which possesses a level higher up in energy. The electron in this level then falls into the strain induced gap level. Thus the character of the spin-density of the donor level does not reflect

its oxygen parentage and this is consistent with the ENDOR studies. Thus, as for the NL8 thermal double donor defects, the chemical composition of the DN and STD(H)N families may be difficult to determine by magnetic resonance.

Finally, we point out that other STD models could be obtained by substituting the C$_i$-H unit in C$_i$O$_{ni}$H defects by a group III atom, or indeed a complex with equivalent coordination. In particular, Al and N are obvious candidates for the STD(Al) and STD(X) families (Gregorkiewicz *et al.*, 1988).

Chapter 7

Concluding remarks

For a long time it was believed that a self-interstitial is inevitably produced when two O-atoms cluster. The argument was based on the volume of a SiO_2 quartz unit which is $\sim2.25\times$ the volume of a host Si atom. Here it is shown that O-atoms can be accommodated in the Si matrix by bending their Si-O-Si units. Only clusters of at least four O-atoms are expected to produce self-interstitials. Moreover, due to the high formation energy of self-interstitial defects, we conclude that these do not form during the early stages of TDD formation (Coutinho *et al.*, 2000*a*).

In collaboration with experimental groups, the VOH_2 defect has been identified by means of IR-spectroscopy (Markevich *et al.*, 2000). This defect is responsible for three LVM-bands, two H-related and one O-related at 2151, 2126 and 943 cm^{-1} respectively. The singly hydrogenated VO has not been detected by IR, but one electron and one hole trap were linked to the defect. The calculations support these assignments

The well known interstitial oxygen defect has been reviewed in detail. In Si, it was found that its potential around the bond centre site varies only by ~10 meV between the bond-centre (D_{3d} symmetry) and puckered configurations (C_2 and C_{1h} symmetry). This is flat enough to allow the defect to tunnel between these configurations at room temperature. In Ge, the situation is somewhat different, with the BC-form considerably higher in energy, so that the defect tunnels only between the puckered forms. Two local

vibrational modes (symmetric and asymmetric stretch) were found, and their combination supports the assignment of the 1750 cm^{-1}-band to a phonon replica (Coutinho *et al.*, 2000*b*).

The effect of hydrostatic pressure on the local modes and structure of O$_i$ and the oxygen dimer has been considered. We found that puckered Si-O-Si units are favoured in the high pressure regime, explaining the trends of the asymmetric-mode frequency in high-pressure measurements. Similar arguments were presented to explain the anomalous temperature-shifts suffered by the O-dimer bands (Coutinho *et al.*, 2000*b*).

We investigated previous suggestions that the oxygen dimer could act as a fast oxygen carrier. Its migration barrier was estimated to be ∼1 eV lower than that of the single interstitial oxygen (2.5 eV). Further investigations revealed that the oxygen trimer and larger aggregates can diffuse through even lower barriers, explaining the fast TDD transformation process. These results are vital to the all oxygen aggregation process. If the dimer was the only fast-diffusing species, soon it would reach extinction after being captured by dominant O$_i$ centres (Jones *et al.*, 2001).

Regarding the structure and composition of TDD defects, we started by investigating the model preferred by experimentalists — the self-interstitial-oxygen model. Here it was shown that a self-interstitial defect is only marginally stable when bound to an oxygen precipitate, and therefore these defects are not expected to survive to temperatures where TDD's form. These conclusions are supported by experiments, where IO_n complexes are observed to break below 200°C. On the other hand, a strong candidate for an IO_2 defect was presented. In this model, an O-dimer and a split-interstitial are bound by only 0.7 eV, and the calculated LVM frequencies are in good agreement with the measurements.

The revelation that the infinite 2NN chain is an insulating sub-oxide presents a definite breakthrough. From ENDOR measurements, we know that the donor electron avoids the TDD core. An electrically inactive core is therefore a *desired* property for the model. In fact, the repulsive core makes the task of experimentalists very difficult. Here we present a novel model for the TDD defects based on electron transfer. The insulating core produces a *stress-induced* empty state overlapping neighbouring Si atoms, lying below

181

those produced by over-coordinated oxygens at the ends. Electrons from the later then drop into the former, lose their oxygen parentage, and therefore explain the ENDOR data (Jones *et al.*, 2001; Coutinho *et al.*, 2001*b*).

The model is also consistent with electronic IR-data, where the effective strain along [001] decreases with the chain length. This suggests a decreasing deformation potential for the stress-induced state, and hence a decrease of the ground state binding energy. This trend is also reproduced by the stress-energy tensor. Of particular importance are the results from a collaboration with an experimental group. At most three distinct vibrational bands were observed for each donor, all well accounted by the model. In Si, the high-frequency band at $\sim$1000 cm^{-1} is localised at the ends, and does not produce new modes in the mixed ^{16}O-^{18}O isotopic samples. This is not the case for the $\sim$720 cm^{-1} and $\sim$580 cm^{-1}-bands, which are localised at the core O and Si atoms respectively. In Ge, the picture is similar, but due to the more pronounced buckled ends, both O-related modes couple several O-atoms (Murin *et al.*, 2001).

The shallow thermal donors were also investigated. Here we focused on the STD defects containing hydrogen. In view of recent experimental progress, we assigned a C_iO_iH interstitial complex to a shallow donor labelled D1, believed to be a precursor for the STD(H) family. This defect is of particular interest as it displays bi-stability with negative-U ordering of ionisation energies. We found that a large local distortion coupled with a strong change in the electronic structure triggers this phenomenon. In the negative charge state the oxygen atom is two-fold coordinated, but in the positive defect the O-atom is over-coordinated (Coutinho *et al.*, 2001*a*). These structures are consistent with the observed 1025 cm^{-1}-band for the D1$^-$, and its disappearance for D1$^+$. In the latter case, the band is expected to fall in the 700 cm^{-1} region. Unfortunately this band escaped detection. These results support a previous suggestion by Ewels *et al.* (1996*a*), where a model for the STD(H) family containing a carbon atom was put forward.

I should now conclude with some remarks regarding some problems still unsolved. The interaction between self-interstitials and oxygen is a technologically important problem. There is much work to be done here, with the most *fundamental* defects such as the single

interstitial or the IO_i complex unresolved. The interest in these problems stems from the fact that in large scale integration technology, implantation of dopants is an important issue. This is especially the case for packed materials such as SiC or diamond, where in-diffusion is not an option. The IO_2 complex has an acceptor level at $E_c - 0.11$ eV. However, only LVMs for the neutral defect were observed. We expect that the defect will change its structure after trapping an electron.

In Chapter 5 we saw how hydrogen can effectively interact with the O-2NN chains. This interaction can itself be used to test the model experimentally. First, the Si-H bonds should produce IR-active LVM bands, and secondly it is expected the doubly hydrogenated complex to act as an acceptor with an electron trap $\sim$150 meV below the conduction band. Such observation would provide convincing evidence for the strain-induced state. The capture cross section for the donor model should display a large anisotropy along directions orthogonal and along the (110) plane. This feature has been observed after measurements of a Poole-Frenkel effect with different orientations of the electric field (Michel and Kimerling, 1994). However, the trends of the capture cross section could also be measured for different stages of TDD(N) formation. This would allow us to compare the approximately linear dependence of the capture cross section with N, for the O-2NN chain.

Effective-mass theory has proven to be effective in modelling shallow states. A description of the TDD model within EMT, which takes into account the microscopic features of the chain, is expected to provide extra information, especially the trends and splittings of the energy levels. Extensive IR-absorption data is available, awaiting for comparison with the theory.

The O-2NN model also predicts IR-active bands which have not yet been observed. This is an obvious track that should be pursued by experiment. It is possible that these modes are affected by strong broadening due to short life-times, and therefore difficult to detect. Another possibility is the fact that the Si samples possess a strong background absorption due to free-carriers between $\sim$600 and $\sim$800 cm^{-1}, hiding the TDD-related LVMs.

The C_iO_iH and $C_iO_{2i}H$ complexes were assigned to D1 and D2 [or STD(H)2] defects. Here

we give detailed insight about the mechanism that triggers bi-stability, i.e., the switching between three-fold and two-fold coordinated oxygen atoms. Several results lead us to suggest the assignment of D1 to the C_iO_iH complex. These include the LVMs, electrical levels and their negative correlation. The presence of carbon is assumed on the basis of such observations.

Although we only dealt with the hydrogen-related shallow thermal donors, much work has also to be done on other families. This is the case of the STD(Al) and STD(X), where X is still unknown. Until now, only oxygen, aluminium and hydrogen have been detected by ENDOR. Unfortunately, as for the TDD defects, we anticipate a negligible amplitude of the donor wavefunction at the core. This feature seems to be the very reason for our poor understating of TD's after so many years of research effort. We need then to find alternative ways to probe these defects.

Finally, I would like to stress the enormous success resulting from the close collaboration between theorists and experimentalists. Fruitful discussions and suggestions were very much responsible for the results reported here.

Bibliography

Abdlullin K A, Mukashev B N, and Gorelkinskii Y V, Semicond. Sci. Technol. **11**, 1696 (1998).

Abe T, *VLSI Electronics Microstructure Science*, volume 12 (Academic Press, New York, 1985).

Åberg D, Svensson B G, Hallberg T, and Lindström J L, Phys. Rev. B **58**, 12944 (1998).

Ammerlaan C A J, Zevenbergen I S, Martynov Y V, and Gregorkiewicz T, in *Early Stages of Oxygen Precipitation in Silicon*, (edited by R Jones), volume 17 of *NATO Advance Science Institutes, Series 3: High Technology*, p. 61 (Kluwer Academic, Dordecht, 1996).

Andersen O, Private communication, the reorientation of VO is allways observed for the neutral defect. In the negative charge state an electron is first emitted. (2001).

Artacho E and Ynduráin F, Solid State Commun. **72**, 393 (1989).

Artacho E, Ynduráin F, Pajot B, Ramírez R, Herrero C P, Khirunenko L I, Itoh K M, and Haller E E, Phys. Rev. B **26**, 4199 (1982).

Bachelet G B, Hamann D R, and Schlüter M, Phys. Rev. B **26**, 4199 (1982).

Baldereschi A, Phys. Rev. B **7**, 5212 (1973).

Baraff G A and Schlüter M, Phys. Rev. Lett. **55**, 1327 (1985).

von Barth U and Hedin L, J. Phys. C **5**, 1629 (1972).

Bean A R and Newman R C, Solid State Commun. **9**, 271 (1971).

Bean A R and Newman R C, J. Phys. Chem. Solids **33**, 255 (1972).

Benton J L, Lee K M, Freeland P E, and Kimerling L C, J. Elect. Mat. **14a**, 647 (1985).

Born M and Huang K, *Dynamical Theory of Crystal Lattices* (Oxford University Press, Oxford, 1954).

Born M and Oppenheimer R, Ann. Physik **87**, 457 (1925).

Bosomworth D R, Hayes W, Spray A R L, and Watkins G D, Proc. Roy. Soc. Lond. A **317**, 133 (1970).

Bourgoin J and Lannoo M, *Point Defects in Semiconductors II: Experimental Aspects* (Springer–Verlag, Berlin, 1983).

Briddon P R, EMIS Data Rev. **20**, 330 (1999).

Brust D, in *Methods in Computational Physics*, volume 8, p. 33 (Academic Press, 1968).

Budde M, Cheney C P, Lüpke G, Tolk N H, and Feldman L C, Phys. Rev. B **63**, 195203 (2001).

Capaz H B, Assali L V C, Kimerling L C, Cho K, and Joannopoulos J D, Phys. Rev. B **59**, 4898 (1999).

Ceperley D M, Phys. Rev. B **18**, 3126 (1978).

Ceperley D M and Alder B J, Phys. Rev. Lett. **45**, 566 (1980).

Chadi D J, Phys. Rev. Lett. **77**, 861 (1996).

Chadi D J and Cohen M L, Phys. Rev. B **7**, 692 (1973).

Cho K, in *Excitons*, (edited by K Cho), number 14 in Topics in current physics, pp. 15–53 (Springer–Verlag, 1979).

Coomer B J, Leary P, Budde M, Nielsen B B, Jones R, Öberg S, and Briddon P R, Mater. Sci. Eng. B **58**, 36 (1999*a*).

Coomer B J, Resende A, Goss J P, Jones R, Öberg S, and Briddon P R, Physica B **273-274**, 520 (1999*b*).

Coomer R J B J, Goss J P, Hourahine B, and Resende A, Solid State Phenomena **71**, 173 (2000).

Corbett J W, McDonald R S, and Watkins G D, J. Phys. Chem. Solids **25**, 873 (1964*a*).

Corbett J W, Watkins G D, Chrenko R M, and McDonald R S, Phys. Rev. **121**, 1015 (1961).

Corbett J W, Watkins G D, and McDonald R S, Phys. Rev. **135**, A1381 (1964*b*).

Coutinho J, Jones R, and Briddon P R, in *Second ENDEASD Workshop*, (edited by C L Claeys), p. 244 (Kista, 2000*a*).

Coutinho J, Jones R, Briddon P R, and Öberg S, Phys. Rev. B **62**, 10824 (2000*b*).

Coutinho J, Jones R, Briddon P R, Öberg S, Murin L I, Markevich V P, and Lindström J L, To appear in Phys. Rev. B, the interstitial carbon-oxygen defect and the shallow thermal donors with hydrogen (2001*a*).

Coutinho J, Jones R, Öberg S, Briddon P R, Murin L I, Markevich V P, and Lindström J L, Submited to Phys. Rev. Lett., thermal Double Donors in Si and Ge (2001*b*).

Cuthbert J D, Phys. Rev. B **1**, 1552 (1970).

Davies G, Rep. Prog. Phys. **44**, 787 (1981).

Davies G, Phys. Reports **176**, 83 (1989).

Davies G, in *Identification of Defects in Semiconductors*, (edited by M Stavola), volume 51B of *Semiconductors and Semimetals*, p. 1 (Academic Press, 1999).

Davies G and Newman R C, in *Handbook on Semiconductors*, (edited by S Mahajan), volume 3b, p. 1557 (Elsevier Science, Amsterdam, 1994).

Davies G, Oates A S, Newman R C, Wooley R, Lightowlers E C, Binns M J, and Wilkes J G, J. Phys. C **19**, 841 (1986).

Dawber P G and Elliot R J, Proc. Phys. Soc. **81**, 453 (1963).

Deák P, Snyder L C, and Corbett J W, Phys. Rev. B **45**, 11612 (1992).

Dean P J, Haynes J R, and Flood W F, Phys. Rev. **161**, 711 (1967).

Dean P J and Herbert D C, in *Excitons*, (edited by K Cho), number 14 in Topics in current physics, pp. 55–176 (Springer–Verlag, 1979).

Deleo G G, Milsted C S, and Kralik J C, Phys. Rev. B **31**, 3588 (1985).

Dirksen R, Gregorkiewicz T, and Ammerlaan C A J, Phys. Stat. Sol. (b) **210**, 539 (1998).

Doren V V, Alsenoy C V, and Geerlings P, editors, *Density functional theory and its application to materials*, volume 577 (IoP Institute of Physics Publishing Ltd, New York, 2001).

Epstein S T, Hurley A C, Wyatt R E, and Parr R G, J. Chem. Phys. **47**, 1275 (1967).

Estreicher S K, Mater. Sci. Eng. Rep. **14**, 317 (1995).

Ewald P, Ann. Physik **64**, 253 (1921).

Ewels C P, Jones R, Miro S O J, and Deák P, Phys. Rev. Lett. **77**, 865 (1996*a*).

Ewels C P, Jones R, and Öberg S, Mater. Sci. Forum **196-201**, 1297 (1995).

Ewels C P, Jones R, and Öberg S, in *Early Stages of Oxygen Precipitation in Silicon*, (edited by R Jones), volume 17 of *NATO Advance Science Institutes, Series 3: High Technology*, p. 141 (Kluwer Academic, Dordecht, 1996*b*).

Faulkner R A, Phys. Rev. **184**, 713 (1969).

Fazzio A, Janotti A, and da Silva A J R, Phys. Rev. B **61**, R2401 (2000).

Feher G, Phys. Rev. **114**, 1219 (1959*a*).

Feher G, Phys. Rev. **8**, 486 (1959*b*).

Feklisova O, Yarykin N, Yakimov E, and Weber J, Physica B **273-274**, 235 (1999).

Feklisova O, Yarykin N, Yakimov E B, and Weber J, in *21st International Conference on Defects in Semiconductors*, (edited by B K Meyer and J M Spaeth) (Giessen, 2001).

Feklisova O V and Yarykin N A, Semicond. Sci. Technol. **12**, 742 (1997).

Fletcher R C, Yager W A, Pearson G L, Holden A N, Read W T, and Merritt F R, Phys. Rev. **94**, 1392 (1954*a*).

Fletcher R C, Yager W A, Pearson G L, and Merritt F R, Phys. Rev. **95**, 844 (1954*b*).

Flynn C P, *Point defects and diffusion* (Oxford University Press, Glasgow, 1972).

Flynn C P, Phys. Rev. Lett. **35**, 1721 (1975).

Fock V, Z. Phys. **61**, 126 (1930).

el Fotouh F A A and Newman R C, Solid State Commun. **15**, 1409 (1974).

Fukuoka N, Saito H, and Kambe Y, Jap. J. Appl. Phys. **22**, L353 (1983).

Fuller C S, Ditzenberger J A, Hannay N B, and Buchler E, Phys. Rev. **96**, 833 (1954).

Fuller C S and Logan R A, J. Appl. Phys. **28**, 1427 (1957).

Gienger M, Glaser M, and Laßmann K, Solid State Commun. **86**, 285 (1993).

Glodeneau A, Phys. Stat. Sol. **19**, K43 (1967).

Gösele U and Tan T, Appl. Phys. A **28**, 79 (1982).

Gregorkiewicz T, Bekman H H P T, and Ammerlaan C A J, Phys. Rev. B **38**, 3998 (1988).

Gregorkiewicz T, van Wezep D A, Bekman H H P T, and Ammerlaan C A J, Phys. Rev. Lett. **59**, 1702 (1987).

Grimmeiss H G and Janzén E, *Deep Centers in Semiconductors*, chapter 2, p. 87 (Gordon and Breach Science Publishers, 1992).

Grimmeiss H G, Jazén E, and Larsson K, Phys. Rev. B **25**, 2627 (1982).

Grimmeiss H G, Jazén E, and Skarstam B, J. Appl. Phys. **51**, 4212 (1980).

Hallberg T, Murin L I, Lindström J L, and Markevich V P, J. Appl. Phys. **84**, 2466 (1998).

Hamann D R, Schlüter M, and Chiang C, Phys. Rev. Lett. **48**, 1425 (1982).

Harrison W A, *Pseudopotentials in the theory of metals* (W. A. Benjamim, New york, 1966).

Heine V, Solid State Physics **24**, 1 (1970).

Henry P M, Farmer J W, and Meese, Appl. Phys. Lett. **45**, 454 (1984).

Hermansson J, Murin L I, Hallberg T, Markevich V P, Lindström J L, Kleverman M, and Svensson B G, Physica B **302-303**, 188 (1999).

Hohenberg P and Kohn W, Phys. Rev. **136**, 864 (1964).

Hourahine B, Jones R, Öberg S, and Briddon P R, Phys. Rev. B **59**, 15729 (1999).

Hrostowski H J and Kaiser R H, Phys. Rev. **107**, 966 (1957).

Hrostowski H J and Kaiser R H, J. Phys. Chem. Solids **9**, 214 (1959).

Imai M, Noda H, Shibata M, and Yatsurugi Y, Appl. Phys. Lett. **50**, 395 (1987).

James A M and Lord M P, *Macmillan's Chemical and Physical Data* (Macmillan, London, 1992).

Jazén E, Grossman G, Stedman R , and Grimmeiss H G, Phys. Rev. B **31**, 8000 (1985).

Jazén E, Stedman R, Grossman G, and Grimmeiss H G, Phys. Rev. B **29**, 1907 (1984).

Johannesen P, Nielsen B B, and Byberg J R, Phys. Rev. B **61**, 4659 (2000).

Johnson N M and Hahn S K, Appl. Phys. Lett. **48**, 709 (1986).

Jones R, Semicond. Sci. Technol. **5**, 255 (1990).

Jones R, editor, *Early Stages of Oxygen Precipitation in Silicon*, volume 17 of *NATO Advance Science Institutes, Series 3: High Technology* (Kluwer Academic, Dordecht, 1996).

Jones R and Briddon P R, in *Identification of Defects in Semiconductors*, (edited by M Stavola), volume 51A of *Semiconductors and Semimetals*, p. 287 (Academic Press, 1999).

Jones R, Coutinho J, Öberg S, and Briddon P R, in *21st International Conference on Defects in Semiconductors*, (edited by B K Meyer and J M Spaeth) (Giessen, 2001).

Jones R and Öberg S, Phys. Rev. Lett. **68**, 86 (1992).

Jones R, Öberg S, Goss J, and Briddon P R, Phys. Rev. Lett. **75**, 2734 (1995).

Jones R, Öberg S, and Umerski A, Mater. Sci. Forum **83-87**, 551 (1991).

Jones R, Umerski A, and Öberg S, Phys. Rev. B **45**, 11321 (1992).

Jones R O and Gunnarsson O, Rev. Mod. Phys. **61**, 689 (1989).

Kaiser W, J. Phys. Chem. Solids **23**, 225 (1962).

Kaiser W, Frisch H L, and Reiss H, Phys. Rev. **112**, 1546 (1958).

Kaiser W, Keck P W, and Lange C F, Phys. Rev. **101**, 1264 (1956).

Kantorovich L N, Shluger A L, and Stoneham A M, Phys. Rev. Lett. **85**, 3856 (2000).

Kaplianskii A A, Opt. Spectrosc. **16**, 329 (1964).

Keating P N, Phys. Rev. **145**, 637 (1966).

Kemble, Rev. Mod. Phys. **1**, 206 (1932).

van Kemp R, Sieverts E G, and Ammerlaan C A J, Phys. Rev. B **40**, 4037 (1989a).

van Kemp R, Sprenger M, Sieverts E G, and Ammerlaan C A J, Phys. Rev. B **40**, 4064 (1989b).

Kimerling L C, in *Radiation Effects in Semiconductors*, (edited by N B Urli and J W Corbett), p. 221 (Institute of Physics, London, 1976).

Kisielowski C, in *21st International Conference on Defects in Semiconductors*, (edited by B K Meyer and J M Spaeth) (Giessen, 2001).

Kittel C, *Introduction to Solid State Physics* (John Wiley & Sons, New York, 1986), 6th edition.

Klechko A A, Litvinov V V, Markevich V P, and Murin L I, Semiconductors **33**, 1163 (1999).

Kleverman M, Fornell J O, Olajos J, Grimmeiss H G, and Lindström J L, Phys. Rev. B **37**, 10199 (1988).

Kohn W, Phys. Rev. **98**, 915 (1955).

Kohn W, Solid State Physics **5**, 257 (1957).

Kohn W and Sham L J, Phys. Rev. **140**, A1133 (1965).

Koopmans T, Physica **1**, 104 (1934).

Kurner W, Sauer R, Dörnen A, and Tonke K, Phys. Rev. B **39**, 13327 (1989).

Lang D V, J. Appl. Phys. **45**, 3014 (1974a).

Lang D V, J. Appl. Phys. **45**, 3023 (1974b).

Langhanki B, Greulich-Weber S, M.Speath J, Markevich V P, Murin L I, Mchedlidze T, and Suezawa M, Physica B **302-303**, 212 (2001).

Larsen A N, Goubet J J, Mejlholm P, Christensen J S, Fanciulli M, Gunnlaugsson H P, Weyer G, Petersen J W, Resende A, Kaukonen M, Jones R, Öberg S, Briddon P R, Svensson B G, Lindström J L, and Dannefaer S, Phys. Rev. B **62**, 4535 (2000).

Laßmann K, Linsenmaier C, Maier F, Zeller F, Haller E E, Itoh K M, Khirunenko L I, Pajot B, and Müssig H, Physica B **263-264**, 384 (1999).

Lawley K P, *Ab-initio methods in quantum chemistry, Parts I and II* (Wiley-Interscience, Chichester, 1987).

Leary P, Jones R, and Öberg S, Phys. Rev. B **57**, 3887 (1998).

Lee Y J, von Boehm J, Pesola M, and Nieminen R M, Phys. Rev. Lett. **86**, 3060 (2001).

Leeuw S W D, Perram J W, and Smith E R, Proc. Roy. Soc. Lond. A **373**, 27 (1980).

Lightowlers E C, *Growth and Characterisation of Semiconductors*, chapter 5, p. 135 (Adam Hilger, Bristol, 1990).

Lightowlers E C, Newman R C, and Tucker J H, Semicond. Sci. Technol. **9**, 1370 (1994).

Lightowlers E C and Safonov A N, Mater. Sci. Forum **258-263**, 617 (1997).

Lindström J L and Hallberg T, Phys. Rev. Lett. **72**, 2729 (1994).

Lindström J L and Hallberg T, in *Early Stages of Oxygen Precipitation in Silicon*, (edited by R Jones), volume 17 of *NATO Advance Science Institutes, Series 3: High Technology*, p. 41 (Kluwer Academic, Dordecht, 1996).

Lindström J L, Hallberg T, Hermansson J, Kleverman M, Murin L I, Markevich K V P, and Svensson B G, in *21st International Conference on Defects in Semiconductors*, (edited by B K Meyer and J M Spaeth) (Giessen, 2001).

Lindström J L, Murin L I, Markevich V P, Hallberg T, and Svensson B G, Mater. Sci. Forum **273-274**, 291 (1999*a*).

Lindström J L, Murin L I, Markevich V P, Hallberg T, and Svensson B G, Physica B **273-274**, 291 (1999*b*).

Lipari N O and Altarelli M, Solid State Commun. **18**, 951 (1976).

Litvinov V V, Murin L I, Lindström J L, Markevich V P, and Klechko A A, Semiconductors **35**, 900 (2001).

Lundqvist S, *Theory of the Inhomogeneous Electron Gas* (Plenum, New York, 1983).

M. A. L. Marques A. Castro A R, J. Chem. Phys. **115**, 3006 (2001).

MacDonald J K L, Phys. Rev. **43**, 830 (1933).

Makarenko L F, Markevich V P, and Murin L I, Sov. Phys. Semic. **19**, 1192 (1985).

Maradudin A A, Solid State Physics **18**, 273 (1966).

Maradudin A A, Montroll E W, and Weiss G H, *Lattice dynamics in the harmonic approximation* (Academic Press, New York, 1963).

Markevich V P, Mchedlidze T, and Suezawa M, Phys. Rev. B **56**, R12695 (1997*a*).

Markevich V P, Mchedlidze T, Suezawa M, and Murin L I, Phys. Stat. Sol. (b) **210**, 545 (1998*a*).

Markevich V P, Medvedeva I F, Murin L I, Sekiguchi T, Suezawa M, and Sumino K, Mater. Sci. Forum **196-201**, 945 (1995).

Markevich V P, Murin L I, Sekiguchi T, and Suezawa M, Mater. Sci. Forum **258-263**, 217 (1997*b*).

Markevich V P, Murin L I, Suezawa M, Lindström J L, Coutinho J, Jones R, Briddon P R, and Öberg S, Phys. Rev. B **61**, 12964 (2000).

Markevich V P, Suesawa M, and Murin L I, J. Appl. Phys. **84**, 1246 (1998*b*).

Markevich V P, Suezawa M, Sumino K, and Murin L I, J. Appl. Phys. **76**, 7347 (1994).

Martin G M and Markram-Ebeid S, *Deep Centers in Semiconductors*, chapter 6, p. 457 (Gordon and Breach Science Publishers, 1992).

Martinez E, Plans J, and Ynduráin F, Phys. Rev. B **36**, 8043 (1987).

Martynov A Y, Gregorkiewicz T, and Ammerlaan C A J, Phys. Rev. Lett. **74**, 2030 (1995).

Mayur A J, Sciacca M D, Udo M K, Ramdas A K, Itoh K, Wolk J, and Haller E E, Phys. Rev. B **49**, 16293 (1994).

McCluskey M D, Private communication, spurious effects due to non-linear fitting procedure (1999).

McCluskey M D, J. Appl. Phys. **87**, 3593 (2000).

McCluskey M D and Haller E E, Phys. Rev. B **56**, 9520 (1997).

McQuaid S A, Johnson B K, andR. Falster D G, Ashwin M J, and Tucker J H, J. Appl. Phys. **86**, 1878 (1999).

McWeeny R, *Methods of Molecular Quantum Mechanics* (Academic Press, New York, 1989).

Meese J M, Farmer J W, and Lamp C D, Phys. Rev. Lett. **51**, 1286 (1983).

Merle J C, Capizzi M, Fiorini P, and Frova A, Phys. Rev. B **17**, 4821 (1978).

Michel J and Kimerling L C, in *Oxygen in Silicon*, (edited by F Shimura), volume 42 of *Semiconductors and Semimetals*, p. 151 (Academic Press, Orlando, 1994).

Michel J, Nicklas J R, and Spaeth J M, Phys. Rev. B **40**, 255 (1989).

Mikkelsen J C, Mater. Res. Soc. Symp. Proc. **59**, 19 (1986).

Miller G L, Lang D V, and Kimerling L C, Ann. Rev. Mater. Sci. **7**, 377 (1977).

Monkhorst H J and Pack J D, Phys. Rev. B **13**, 5188 (1976).

Montroll E W and Potts R B, Phys. Rev. **100**, 525 (1955).

Mooney P M, in *Identification of Defects in Semiconductors*, (edited by M Stavola), volume 51B of *Semiconductors and Semimetals*, p. 93 (Academic Press, 1999).

Mooney P M, Cheng L J, Suli M, Gerson J D, and Corbett J W, Phys. Rev. B **15**, 3836 (1977).

Morton J R and Preston K F, J. Magn. Reson. **30**, 577 (1977).

Murin L I, Private communication, tDD(0) is metastable by about 0.7 eV, and therefore its donor levels where not measured yet (2001).

Murin L I, Hallberg T, Markevich V P, and Lindström J L, Phys. Rev. Lett. **80**, 93 (1998).

Murin L I, Lindström J L, Markevich V P, Hallberg T, Litvinov V V, Coutinho J, Jones R, Briddon P R, and Öberg S, in *21st International Conference on Defects in Semiconductors*, (edited by B K Meyer and J M Spaeth) (Giessen, 2001).

Murin L I and Markevich V P, in *Early Stages of Oxygen Precipitation in Silicon*, (edited by R Jones), volume 17 of *NATO Advance Science Institutes, Series 3: High Technology*, p. 329 (Kluwer Academic, Dordecht, 1996).

Murin L I, Markevich V P, Hallberg T, and Lindström J L, Solid State Phenomena **69**, 309 (1999).

Musgrave M J P and Pople J A, Proc. Roy. Soc. **A268**, 474 (1962).

Needels M, Joannopoulos J D, Bar-Yam Y, and Pantelides S T, Phys. Rev. B **43**, 4208 (1991*a*).

Needels M, Joannopoulos J D, Bar-Yam Y, and Pantelides S T, Mater. Res. Soc. Symp. Proc. **209**, 103 (1991*b*).

Newman R C, *Infra-red studies of crystal defects* (Taylor & Francis Ltd, London, 1973).

Newman R C, J. Phys. C **18**, L967 (1985).

Newman R C, J. Phys.: Cond. Matter **12**, R335 (2000).

Newman R C, Ashwin M J, Pritchard R E, and Tucker J H, Phys. Stat. Sol. (b) **210**, 519 (1998).

Newman R C and Jones R, in *Oxygen in Silicon*, (edited by F Shimura), volume 42 of *Semiconductors and Semimetals*, p. 298 (Academic Press, Orlando, 1994).

Newman R C, Tucker J H, Semaltianos N G, Lightowlers E C, Gregorkiewicz T, Zevenbergen I S, and Ammerlaan C A J, Phys. Rev. B **54**, R6803 (1996).

Newman R C and Willis J B, J. Phys. Chem. Solids **26**, 373 (1965).

Nielsen B B, Unpublished, vO2 is D2d after stress alignment experiments (1996).

Nielsen B B, Hoffmann L, and Budde M, Mater. Sci. Forum **196-201**, 933 (1995).

Nielsen B B, Johannesen P, Stallinga P, Nielsen K B, and Byberg J R, Phys. Rev. Lett. **79**, 1507 (1997).

Nielsen K B, Dobaczewski L, Goscinski K, Bendesen R, Andersen O, and Nielsen B B, Physica B **273-274**, 167 (1999).

Ning T H and Sah C T, Phys. Rev. B **4**, 3468 (1971).

Northrup J E, Phys. Rev. B **62**, 2487 (1989).

Öberg S, Ewels C P, Jones R, Lindström T H J L, and Briddon P R, Phys. Rev. Lett. **81**, 2930 (1998).

Oshiyama A and Saito M, *Defect Control in Semiconductors* (Elsevier Science Publishers, New York, 1990).

Ourmazd A, Schröter W, and Bourret A, J. Appl. Phys. **56**, 1670 (1984).

Pack J D and Monkhorst H J, Phys. Rev. B **16**, 1748 (1977).

Pajot B, Artacho E, Ammerlaan C A J, and Spaeth J M, Phys. Rev. B **7**, 7077 (1995).

Pajot B, McQuaid S, Newman R C, Song C, and Rahbi R, Mater. Sci. Forum **143-147**, 969 (1994).

Palmer D W, *Growth and Characterisation of Semiconductors*, chapter 10, p. 187 (Adam Hilger, Bristol, 1990).

Pantelides S T and Sah C T, Phys. Rev. B **10**, 638 (1974).

Parr R G and Yang W, *Density-Functional Theory of Atoms and Molecules* (Oxford University Press, New York, 1989).

Peaker A R, Evans-Freeman J H, Kan P Y Y, Rubaldo L, Hawkins I D, Vernon-Parry K D, and Dobaczewski L, Physica B **273-274**, 243 (1999).

Pearton S J, Corbett J W, and Stovola M, *Hydrogen in Crystalline Semiconductors* (Springer-Verlag, Berlin, 1992).

Perdew J P, in *Electronic Structure of Solids '91*, (edited by P Ziesche and H Eschrig) (Akademie Verlag, Berlin, 1991).

Perdew J P, Burke K, and Ernzerhof M, Phys. Rev. Lett. **77**, 3865 (1996*a*).

Perdew J P, Burke K, and Ernzerhof M, Phys. Rev. B **54**, 16533 (1996*b*).

Perdew J P and Wang Y, Phys. Rev. B **45**, 13244 (1992).

Perdew J P and Zunger A, Phys. Rev. B **23**, 5048 (1981).

Pesola M, von Boehm J, Mattila T, and Nieminen R M, Phys. Rev. B **60**, 11449 (1999*a*).

Pesola M, von Boehm J, and Nieminen R M, Phys. Rev. Lett. **82**, 4022 (1999*b*).

Pickett W E, Comp. Phys. Rep. **9**, 115 (1989).

Pisany C, Dovea R, and Roetti C, *Hartree-Fock Ab-initio Treatment of Crystaline Systems* (Springer-Verlag, Berlin, 1988).

Pople J A and Beverage D L, *Approximate Molecular Orbital Theory* (McGraw-Hill, New-York, 1970).

Puska M J, Pöykkö S, Pesola M, and Nieminen R M, Phys. Rev. B **58**, 1318 (1998).

Qian G X and Martin R M, Phys. Rev. B **38**, 7649 (1988).

Rajagopal A K and Callaway J, Phys. Rev. B **7**, 1912 (1973).

Ramamoorthy M and Pantelides S T, Phys. Rev. Lett. **76**, 267 (1996).

Ramamoorthy M and Pantelides S T, Appl. Phys. Lett. **75**, 115 (1999).

Ramdas A K and Rodriguez S, Rep. Prog. Phys. **44**, 1297 (1981).

Reif F, *Fundamentals of Statistical and Thermal Physics* (McGraw-Hill, New York, 1965).

Resende A, Jones R, Öberg S, and Briddon P R, Phys. Rev. Lett. **82**, 2111 (1999).

Roothaan C C J, Rev. Mod. Phys. **23**, 69 (1951).

Safonov A N, Lightowlers E C, Davies G, Leary P, Jones R, and Öberg S, Phys. Rev. Lett. **77**, 4812 (1996).

Sangster M J L, Newman R C, Gledhill G A, and Upadhyay S B, Semicond. Sci. Technol. **7**, 1295 (1992).

Schaefer H F, *The electronic structure of atoms and molecules.* (Addison-Wesley, Reading, 1977).

Schiff L I, *Quantum Mechanics* (McGraw-Hill, Singapore, 1955).

Schroder D K, Chen C S, Kang J S, and Song X D, J. Appl. Phys. **63**, 136 (1988).

Shaw D, *Atomic Diffusion in Semiconductors* (Plenum, New York, 1973).

Shimura F, editor, *Oxygen in Silicon*, volume 42 of *Semiconductors and Semimetals* (Academic Press, Orlando, 1994).

Sieverts E, *An EPR and ENDOR study on defects in silicon*, Ph.D. thesis, University of Amsternam (1978).

Singh J, *Physics of Semiconductors and Their Heterostructures* (McGraw-Hill, New York, 1993).

Slater J C, Phys. Rev. **34**, 1293 (1929).

Slater J C, *Quantum Theory of Molecules and Solids*, volume 2 (McGraw-Hill, New York, 1965).

Snyder L C and Corbett J W, in *Oxygen, Carbon, Hydrogen and Nitrogen in Silicon*, (edited by S J Pearton, J W Corbett, and S J Pennycook), volume 59, p. 207 (Matterials Research Society, Pittsburgh, 1985).

Snyder L C, Wu R, and Deák P, Radiat. Eff. Def. Solids **111-112**, 393 (1989).

Snyder L C, Wu R, and Deák P, in *Early Stages of Oxygen Precipitation in Silicon*, (edited by R Jones), volume 17 of *NATO Advance Science Institutes, Series 3: High Technology*, p. 419 (Kluwer Academic, Dordecht, 1996).

Song L W, Zhan X D, Benson B W, and Watkins G D, Phys. Rev. Lett. **60**, 460 (1988).

Song L W, Zhan X D, Benson B W, and Watkins G D, Phys. Rev. B **42**, 5765 (1990).

Spaeth J M, in *Early Stages of Oxygen Precipitation in Silicon*, (edited by R Jones), volume 17 of *NATO Advance Science Institutes, Series 3: High Technology*, p. 83 (Kluwer Academic, Dordecht, 1996).

Srivastava G P, editor, *The physics of phonons* (Adam Hilger, Bristol, 1990).

Stavola M, in *Identification of Defects in Semiconductors*, (edited by M Stavola), volume 51B of *Semiconductors and Semimetals*, p. 153 (Academic Press, 1999).

Stavola M, Lee K M, Nabity J C, Freeland P E, and Kimerling L C, Phys. Rev. Lett. **54**, 2639 (1985).

Stoneham A M, *Theory of Defects in Solids* (Oxford University Press, London, 1975).

Stoneham A M, Physica Scripta **T25**, 17 (1989).

Stoneham A M and Harker A H, J. Phys. C **8**, 1102 (1975).

Svensson B G, Hallen A, and Sundqvist B U R, Mater. Sci. Eng. B **4**, 285 (1989).

Svensson B J and Lindström J L, Phys. Rev. B **34**, 8709 (1986).

Thijssen J M, *Computational Physics* (Cambridge University Press, Cambridge, 1999).

Thonke K, Hangleiter A, Wagner J, and Sauer R, J. Phys. C **18**, L795 (1985).

Tinkham M, *Group theory and quantum mechanics* (McGraw–Hill, Singapore, 1964).

Trombetta J M and Watkins G D, Appl. Phys. Lett. **51**, 1103 (1987).

Trombetta J M and Watkins G D, Mater. Res. Soc. Symp. Proc. **104**, 93 (1988).

Trombetta J M, Watkins G D, Hage J, and Wagner P, J. Appl. Phys. **81**, 1109 (1997).

van Vleck J H, *Electric and Magnetic Susceptibilities* (Oxford University Press, Oxford, 1932).

Vosko S H, Wilk L, and Nusair M, Can. J. Phys. **58**, 1200 (1980).

Wagner P and Hage J, Appl. Phys. A **49**, 123 (1989).

Wagner P, Hage J, Trombetta J M, and Watkins G D, Mater. Sci. Forum **83-87**, 401 (1992).

de Walle C G V and Martin R M, Phys. Rev. B **35**, 8154 (1987).

Watkins G D, Phys. Rev. B **12**, 5824 (1975).

Watkins G D, Rev. Solid State Sci. **4**, 279 (1990).

Watkins G D, *Deep Centers in Semiconductors*, chapter 3, p. 135 (Gordon and Breach Science Publishers, 1992).

Watkins G D, in *Early Stages of Oxygen Precipitation in Silicon*, (edited by R Jones), volume 17 of *NATO Advance Science Institutes, Series 3: High Technology*, p. 1 (Kluwer Academic, Dordecht, 1996).

Watkins G D, in *Identification of Defects in Semiconductors*, (edited by M Stavola), volume 51A of *Semiconductors and Semimetals*, p. 1 (Academic Press, 1999).

Watkins G D and Brower K L, Phys. Rev. Lett. **36**, 1103 (1976).

Watkins G D and Corbett J W, Phys. Rev. **121**, 1001 (1961*a*).

Watkins G D and Corbett J W, Phys. Rev. **121**, 1015 (1961*b*).

Watkins G D and Corbett J W, Phys. Rev. A **138**, A543 (1965).

Watkins G D and Ham F S, Phys. Rev. B **1**, 4071 (1970).

Weber J and Bohne D I, in *Early Stages of Oxygen Precipitation in Silicon*, (edited by R Jones), volume 17 of *NATO Advance Science Institutes, Series 3: High Technology*, p. 123 (Kluwer Academic, Dordecht, 1996).

Whan R E, Phys. Rev. **140**, A690 (1965).

Whan R E, Appl. Phys. Lett. **8**, 131 (1966*a*).

Whan R E, J. Appl. Phys. **37**, 3378 (1966*b*).

Whan R E and Vook F L, Phys. Rev. **156**, 814 (1967).

Yamada-Kaneta H, Phys. Rev. B **58**, 7002 (1998).

Yamada-Kaneta H, Kaneta C, and Ogawa T, Phys. Rev. B **42**, 9650 (1990).

Yamada-Kaneta H, Shirakawa Y, and Kaneta C, in *Early Stages of Oxygen Precipitation in Silicon*, (edited by R Jones), volume 17 of *NATO Advance Science Institutes, Series 3: High Technology*, p. 389 (Kluwer Academic, Dordecht, 1996).

Yukhnevich A V, Tkachev V D, and Bortnik M V, Sov. Phys. Solid State **8**, 1044 (1966).